SAPIENZA
UNIVERSITÀ DI ROMA

Waves in elastic metamaterials

Doctorate school in Mechanical Engineering
Dottorato di Ricerca in Meccanica Teorica e Applicata – XXXI Ciclo

Candidate
Francesco Coppo
ID number 1096805

Thesis Advisor	Co-Advisor
Prof. Antonio Carcaterra	Prof. Emer. Aldo Sestieri

October 2018

Thesis defended on Feb 11th, 2019
in front of a Board of Examiners composed by:

Prof. Sergio De Rosa (chairman)
Prof. Mauro Chinappi
Prof. Nicola Pio Belfiore

:

Prof. Emer. Adnan Akay
Prof. Alberto Doria

Waves in elastic metamaterials
Ph.D. thesis. Sapienza – University of Rome

This thesis has been typeset by LaTeX and the Sapthesis class.

Version: February 12, 2019

Author's email: francesco.coppo@uniorma1.it

Dedicated to the engineers who didn't stop dreaming

Abstract

Wave propagation in long-range elastic metamaterials produces important propagation phenomena, such as wave stopping, negative and supersonic group velocities. Metamaterials are particular materials that gain peculiar properties not because of the material itself, but thanks to the realization of periodic sub-structures, capable of modifying the behavior of the macro-structure.

The advances in technological machining, especially in the field of additive manufacturing techniques, give the possibility to realize complex elastic connections between different cellular elements; the presence of micro- and nano-scale connected structures changes the dynamic response of materials composed by the aggregation of these lattices. Such solids are clustered as elastic metamaterials.

In homogeneous elastic materials, each elementary cell is connected to its first neighbors, constituting short-range interactions; on the other hand, when the range of connections spreads, interesting phenomena in terms of mechanical wave propagation appear. The chance of controlling wave propagation by simply changing the topology of the elastic connections is an important achievement; for instance, such designed materials can manipulate the mechanical energy flow, by isolating a vibration sensitive area at the cost of routing the energy into less sensitive regions, or better the energy can be focused to be harvested and converted.

A physical mathematical model has been constructed starting from some of the long-range interactions that can be found in nature, such as the presence in classical discrete system (Mass-Spring) of magnetostatic or electrostatic elements. The main feature of these interactions is the dependency on the absolute distance and not on the relative displacement; each element, indeed, exchange forces with all the elements of the system, not only with its close neighbors.

Several approaches to the problem have been adopted to model long-range interaction metamaterials. The expertise in the homogenization of discrete problems involving complex structure has been the theoretical basis for building up a continuous model capable of describing long-range interactive metamaterials. Two opposite approaches have been adopted to describe the phenomenon: (i) a differential approach and (ii) an integral approach. The differential approach needs some assumptions and approximations, especially in the interaction range that needs to be limited in space, while the integral approach use some of the same assumptions and approximations but works with a full interaction range. For this reason, most of the mathematical efforts in modelling such materials has been dedicated to the development of the integral approach-based model.

To better describe the system, the interaction model is based on two prototype forces: the Gauss-like and the Laplace-like. Technically speaking, these interactions, as the ones from which they come from, decay with the distance and respect the action-reaction principle holds. In addition, they have a known Fourier transform; it is not the case with magnetostatic and electrostatic forces, generally power-law based.

The principal result of the investigation consists in finding some properties of phase and group velocities for one-dimensional infinite waveguides, where several unusual phenomena emerge. Namely we show and demonstrate in a close analytical form the

following phenomena: wave-stopping, eigenstate migration, negative group velocity, leading to supersonic propagation.
An analogous approach is used to evaluate wave propagation in long-range beams (Euler-Bernoulli), and in two dimensional membranes with circle-step long-range interaction, with the borne of analogous phenomena.
The investigation includes also a huge experimental campaign, set in cooperation with Technion, Israel Institute of technology. An experimental setup for the testing of single and coupled long-range magnetic waveguide has been built, demonstrating interesting phenomena in terms of magnetically coupled waveguides that reproduce some of the results the theoretical investigation predicts.

Acknowledgments

This Ph.D work has been acknowledged by the funds of the "Vibrations, Vehicle Dynamics and Mechatronics Research Group" of the Department of Mechanical and Aerospace Engineering of Sapienza, University of Rome.

The experimental setup has been developed together with the "Dynamics Laboratory" team at Technion, Israel Institute of Technology, directed by Prof. Izhak Bucher.

Some of the calculus hardware has been supported in the year 2017 with the grant "Avvio alla ricerca", a funding program for Ph.D students and candidates of Sapienza, University of Rome.

General support during the stay in Haifa (Israel) has been supported with the grant "Bando per il finanziamento di progetti di ricerca congiunti per la mobilità all'estero di studenti PhD - XXXI e XXXII ciclo", a grant program for Ph.D students and candidates during long journeys for the development of collaborative projects, provided by Sapienza, University of Rome.

Index of contents

List of Figures

List of Tables

Chapter 1

Outlook on elastic metamaterials

Metamaterials are finely designed materials capable of achieving strange behavior. They respond with unusual phenomena thanks to the particular geometry (lattices) in which they are arranged; not thanks to the physics of the material itself. In general, the dimensions of the lattice is much smaller than the dimensions of the observed phenomena. Such kind of smart materials have been deeply studied since fifty years ago. Nevertheless, they found a meaningful applicability only in the last decades, thanks to the advantages of micro- and nano- manufacturing technologies. Under the term metamaterials (*meta*, "beyond" from the ancient greek) several kinds of materials can be found; the classification is generally made according to the physical phenomenon. Therefore, we can find the group of elastic metamaterials: for example, system where the energy distribution in elastic propagation is modified to preserve the integrity of delicate areas [1].

One important cluster is the family of electromagnetic metamaterials [2, 3]. The investigation focuses on the effects on electromagnetic wave propagation, such as scattering [4] and absorption [5]. Cloaking phenomena are also investigated [6, 7], and other strange propagation behaviors.

Two branches of elastic metamaterials have been widely developed: acoustic and seismic. Both clusters study the control and the absorption of mechanical waves, with different models and scales. Beyond sound absorption [8, 9], acoustic metamaterials are capable of controlling the perturbation flow, thanks to the use of modern materials, like aerogels [10], achieving acoustic cloaking (meaningful result in underwater defense applications).

Seismic metamaterials have been developed to control and absorb the flow of seismic waves [11–14]. In addition, in a multidisciplinary approach, hybrid electromagnetic and elastic structures have been developed, using mechanical switches, for instance, to turn on and off electromagnetic control [15, 16], and for the development of nano-mechanical transistors [17].

Among the purely elastic metamaterials, the structural materials play an important role. Some examples are topological [18] metamaterials with negative indexes [19], and soft materials, capable of achieving anisotropic deformation behaviors [20]. Moreover, the use of origami structures to build self assembling robots [21] can be

found, and the study of mechanical cloaking phenomena [22].
The thesis project describes wave propagation in infinite elastic metamaterials, in which peculiar phenomena appear, as achieved in finite elastic materials [23].
The chance of designing elastic metamaterials is supported by the possibility of physically building connection topologies, thanks to the achievements in additive manufacturing [24–27]. In particular, such advances give the opportunity of building long-range metamaterials: peculiar nonlocal materials, developed by the workgroup in the last years. They represent the theoretical basis for the propagation analysis in this thesis [28, 29].
Other authors focus on the analysis of wave propagation in discrete media [30–35], using different approaches in the definition of long-range interactions.
The work here presented is part of a project on the study of nonlocal connections [36], made by the Vibrations Mechanics group in Sapienza, supervised by Prof. Antonio Carcaterra [37, 38].
Nonlocal connections are classified in several categories, defined by the connection topology, as depicted in Figure 1.1. The red connections indicate the short-range interaction, typical of local elastic connections; the blue dashed lines represent the nonlocal connections.

Five connection families are identified: (i) One to all, (ii) All to all with full connections' range, (iii) All to all with random sparse connections, (iv) All to all with limited connection range and (v) Twin-waves family.

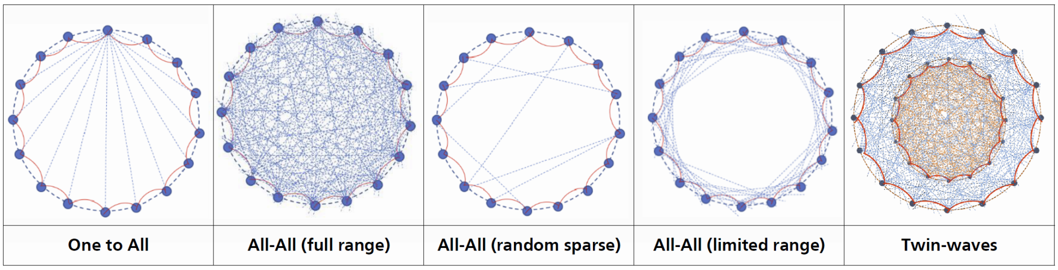

Figure 1.1. Nonlocal connectivity outlook

The one to all group indicates structures where a master-cluster topology is present [1, 39–44]. A mass, called master, is connected to all the other masses of the system, composing the cluster. These masses share an elastic interaction with the master, but they are not necessarily connected among themselves.
The all to all group, (ii), (iii) and (iv), describes an interaction family where each element of the structure has an interaction with several other elements, at maximum with all. In particular, this work spans the all to all full range, and the all to all limited range clusters (also developed in [45]). The the random sparse connections have been studied by other members of the work group [46, 47].
The twin waves family describes the interaction between more than one solid. It has been developed by the group [48, 49] and describes the phenomena borne when two or more local or nonlocal media stand within an interaction range.

The thesis describes some general long-range interactions in elastic media (rods, beam and membranes). The presence of nonlocal interactions leads to peculiar phenomena, unusually present in purely mechanical materials, while they are more common in acoustic or electromagnetic metamaterials. Such phenomena are Wave-Stopping [50–54], Hypersonic/Superluminal phase or group velocities [55–59] and Negative Group Velocity (NGV) [60–63].

The presented phenomena have been highlighted thanks to a closed form approach in the solution of the equations of motion of such waveguides; and the relationship between time frequency and space frequency (dispersion relationship) has been evaluated. The analysis continues through the evaluation of the propagation speeds (Phase velocity and Group velocity); providing the information about wave propagation.

The document is divided in four parts; the first includes this overview on elastic metamaterials, and a section in which the general physical-mathematical model is presented (Section 2).

In Part I the one-dimensional long-range models are developed; in particular long-range interactions in rods (Section 3) and beams (section 4) are presented. Three interaction forces are introduced: (i) Gauss-like, (ii) Laplace-like, and (iii) Rectangular.

In Part II the rectangular model is applied for two-dimensional media (membranes).

In Part III some engineering remarks are presented. In Section 6 an experimental demonstrator is introduced. Some preliminary results are presented in Section 7. Conclusive notes, together with some hints for the forthcoming work, are summarized in Section 8.

Chapter 2

Long-range interaction in continuous media

In the following section a general mathematical approach to the proposed problem is introduced. In the displacement formulation, the equation of motion is ruled by the Navier[1]-Cauchy[2] equation [64], that, for a continuous unbounded three-dimensional elastic medium is:

$$\rho\ \mathbf{u}_{tt}(\mathbf{x},t)-\frac{E}{2(1+\nu)}\left[\nabla^2\mathbf{u}(\mathbf{x},t)+\frac{1}{1-2\nu}\nabla\left(\nabla\cdot\mathbf{u}(\mathbf{x},t)\right)\right]=0 \tag{2.1}$$

The long-range force is introduced as an additional term into the wave equation: $\mathbf{F}(\boldsymbol{P},\boldsymbol{Q})$ is the force that is borne on the particle at $\boldsymbol{P}$, because of the particle at $\boldsymbol{Q}$ as in Figure 2.1. The interaction should guarantee the action-reaction principle holds: $\mathbf{F}(\boldsymbol{P},\boldsymbol{Q})=-\mathbf{F}(\boldsymbol{Q},\boldsymbol{P})$. Considering two punctual elements that are in the

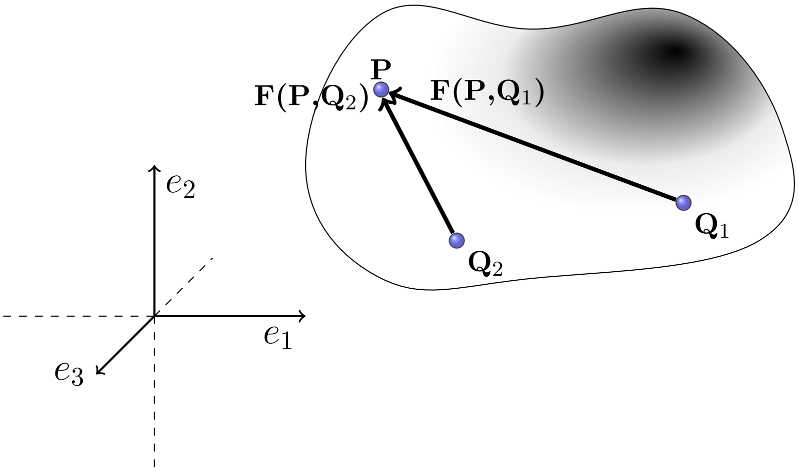

Figure 2.1. Unbounded solid with long-range interactions

---

[1] Claude-Louis Navier (February 10^{th}, 1785 - August 21^{st}, 1836) French engineer and physicist who specialized in mechanics

[2] Baron Augustin-Louis Cauchy (August 21^{st}, 1789 - May 23^{rd}, 1857) French mathematician, engineer and physicist

initial reference configuration at $\boldsymbol{x}$ and $\boldsymbol{\xi}$, respectively, the force between the two is expressed as follows:

$$\mathbf{F}\left(\mathbf{x}+\boldsymbol{u}(\mathbf{x},t),\boldsymbol{\xi}+\boldsymbol{u}(\boldsymbol{\xi},t)\right)=-f(|\mathbf{r}|)\mathbf{r} \tag{2.2}$$

with $\mathbf{u}(\square,t)$ the displacement in the elastic medium of the particle at $\square$ and $\mathbf{r}=\mathbf{x}-\boldsymbol{\xi}+\mathbf{u}(\mathbf{x},t)-\mathbf{u}(\boldsymbol{\xi},t)$. The minus introduces the chosen sign convention: if $f(|\boldsymbol{r}|)$ is positive, the particles attract, if negative, they repulse. The mass density is $\rho(\mathbf{x})$, and the Young and Poisson moduli $E(\mathbf{x})$, $\nu(\mathbf{x})$ are respectively introduced. Moreover, one can consider forces decaying with $|\mathbf{r}|$, such that $\lim_{|\mathbf{r}|\to\infty} f(|\mathbf{r}|)\mathbf{r}=0$. These properties are present in several physical interactions, such as in magnetic dipole-dipole interaction, which formulation is $\mu_M(\boldsymbol{x})\mu_M(\boldsymbol{\xi})\frac{\boldsymbol{r}}{|\boldsymbol{r}|^5}$ ($\mu_M(\boldsymbol{x})$ is the magnetic dipole intensity); analogous considerations hold for the Coulomb electric force. In general, the weakening of the force with the distance is common to many physical problems.

The long-range interaction concerns each punctual element of the medium, and the resultant behavior is affected by the summation of the forces exerted by every punctual element of the volume. The summation on the whole volume leads to an integral term in the equation of motion, leading to a nonlinear integral-differential wave equation. Starting from equation (2.1):

$$\rho\,\mathbf{u}_{tt}(\mathbf{x},t)-\frac{E}{2(1+\nu)}\left[\nabla^2\mathbf{u}(\mathbf{x},t)+\frac{1}{1-2\nu}\nabla\left(\nabla\cdot\mathbf{u}(\mathbf{x},t)\right)\right] \\ +\int_{\boldsymbol{\xi}\in\mathcal{R}^3} f(|\mathbf{r}|)\mathbf{r}\,dV=0 \tag{2.3}$$

In general analytical solutions of equation (2.3) are not possible. However, the linearization of the magnitude term of the force: $f(|\mathbf{r}|)$, with respect to $\boldsymbol{\varepsilon}=\mathbf{u}(\boldsymbol{x},t)-\mathbf{u}(\boldsymbol{\xi},t)$ and assuming $|\boldsymbol{\varepsilon}|\ll|\mathbf{x}-\boldsymbol{\xi}|$, i.e. small deformations, permits to investigate closed form solutions, providing important insights into the wave propagation properties.

Proceeding with the force linearization, the Taylor series of the force up to the first order in terms of $\boldsymbol{\varepsilon}$ brings to the following expansion:

$$f(|\mathbf{r}|)\mathbf{r}=f\left(|\mathbf{x}-\boldsymbol{\xi}|\right)\left(\mathbf{x}-\boldsymbol{\xi}\right)+\frac{\partial}{\partial\boldsymbol{\varepsilon}}\left[f(|\mathbf{r}|)\mathbf{r}\right]\Big|_{\boldsymbol{\varepsilon}=0}+o(\boldsymbol{\varepsilon}^2) \tag{2.4a}$$

$$f(|\mathbf{r}|)\mathbf{r}\approx f\left(|\mathbf{x}-\boldsymbol{\xi}|\right)\left(\mathbf{x}-\boldsymbol{\xi}\right)+\frac{\partial}{\partial\boldsymbol{\varepsilon}}\left[f(|\mathbf{r}|)\mathbf{r}\right]\Big|_{\boldsymbol{\varepsilon}=0} \tag{2.4b}$$

$$\tag{2.4c}$$

and, by single component

$$f(|\mathbf{r}|)r_k\approx f\left(|\mathbf{x}-\boldsymbol{\xi}|\right)(x_k-\xi_k)+\sum_s\left[\frac{\partial f}{\partial\varepsilon_s}\Big|_{\varepsilon=0}(x_k-\xi_k)\varepsilon_s+f|_{\varepsilon=0}\frac{\partial r_k}{\partial\varepsilon_s}\Big|_{\varepsilon=0}\varepsilon_s\right] \tag{2.5a}$$

$$\approx f\left(|\mathbf{x}-\boldsymbol{\xi}|\right)(x_k-\xi_k)+\sum_s\left[\frac{\partial f}{\partial|\boldsymbol{r}|}\Big|_{\varepsilon=0}\frac{\partial|\boldsymbol{r}|}{\partial\varepsilon_s}\Big|_{\varepsilon=0}(x_k-\xi_k)\varepsilon_s+f|_{\varepsilon=0}\frac{\partial r_k}{\partial\varepsilon_s}\Big|_{\varepsilon=0}\varepsilon_s\right] \tag{2.5b}$$

Focusing on the indexed variable:

$$\left.\frac{\partial|\boldsymbol{r}|}{\partial\varepsilon_s}\right|_0 = \frac{\partial}{\partial\varepsilon_s}\left.\left[\sum_i (x_i-\xi_i+\varepsilon_i)^2\right]^{1/2}\right|_0 = \frac{1}{2}\left.\frac{2(x_s-\xi_s+\varepsilon_s)}{|\boldsymbol{x}-\boldsymbol{\xi}+\boldsymbol{\varepsilon}|}\right|_0 = \frac{(x_s-\xi_s)}{|\boldsymbol{x}-\boldsymbol{\xi}|} \tag{2.6a}$$

$$\left.\frac{\partial r_k}{\partial\varepsilon_s}\right|_0 = \left.\frac{\partial}{\partial\varepsilon_s}(x_k-\xi_s+\varepsilon_k)\right|_0 = \delta_{sk} \tag{2.6b}$$

where $\Box|_0 = \Box|_{\varepsilon=0}$. Substituting equation (2.6a) and equation (2.6b) into equation (2.5b), we have:

$$f(|\mathbf{r}|)r_k \approx f\left(|\mathbf{x}-\boldsymbol{\xi}|\right)(x_k-\xi_k) + \sum_s\left[\left.\frac{\partial f}{\partial|\boldsymbol{r}|}\right|_0 \frac{(x_s-\xi_s)}{|\boldsymbol{x}-\boldsymbol{\xi}|}(x_k-\xi_k)\varepsilon_s + f(|\mathbf{r}|)|_0\,\delta_{sk}\varepsilon_s\right] \tag{2.7a}$$

$$\approx f\left(|\mathbf{x}-\boldsymbol{\xi}|\right)(x_k-\xi_k) + \sum_s\left[\left.\frac{\partial f}{\partial|\boldsymbol{r}|}\right|_0 \frac{(x_s-\xi_s)}{|\boldsymbol{x}-\boldsymbol{\xi}|}(x_k-\xi_k)\varepsilon_s + f(|\mathbf{r}|)|_0\,\varepsilon_k\right] \tag{2.7b}$$

that, in vector form becomes:

$$f(|\mathbf{r}|)\mathbf{r} \approx (\mathbf{x}-\boldsymbol{\xi})\,f_0 + \boldsymbol{g}_0\boldsymbol{\varepsilon} + f_0\boldsymbol{\varepsilon} \tag{2.8}$$

where

$$f_0 = f(|\mathbf{r}|)|_0 = f\left(|\mathbf{x}-\boldsymbol{\xi}|\right) \tag{2.9a}$$

$$\boldsymbol{g}_0 = \left.\frac{\partial f}{\partial|\boldsymbol{r}|}\right|_0 \frac{(\mathbf{x}-\boldsymbol{\xi})\otimes(\mathbf{x}-\boldsymbol{\xi})}{|\mathbf{x}-\boldsymbol{\xi}|} \tag{2.9b}$$

The force is composed by three terms: the first is the static component, the other two are the dynamic displacement and dependent forces. Namely, the second order tensor $\boldsymbol{g}_0$ depends on the gradient of the force with respect to the distance, the last due to the static prestress. Therefore, the integral term of equation (2.3) becomes:

$$\int_{\boldsymbol{\xi}\in\mathbb{R}}\left[(\mathbf{x}-\boldsymbol{\xi})\,f_0 + \boldsymbol{g}_0\boldsymbol{\varepsilon} + f_0\boldsymbol{\varepsilon}\right]dV \tag{2.10}$$

Separation of the static and the dynamic components of the displacement, i.e. using the decomposition $\mathbf{u}(\mathbf{x},t) = \mathbf{v}(\mathbf{x}) + \mathbf{w}(\mathbf{x},t)$, leads to:

$$-\frac{E}{2(1+\nu)}\left[\nabla^2\mathbf{v} + \frac{1}{1-2\nu}\nabla\left(\nabla\cdot\mathbf{v}\right)\right] + \int_{\boldsymbol{\xi}\in\mathbb{R}}(\mathbf{x}-\boldsymbol{\xi})\,f_0 dV = 0 \tag{2.11}$$

for the static solution, and to

$$\rho\mathbf{w}_{tt} - \frac{E}{2(1+\nu)}\left[\nabla^2\mathbf{w} + \frac{1}{1-2\nu}\nabla\left(\nabla\cdot\mathbf{w}\right)\right] + \\ + \int_{\boldsymbol{\xi}\in\mathbb{R}}\left(\boldsymbol{g}_0\boldsymbol{\varepsilon} + f_0\boldsymbol{\varepsilon}\right)dV = 0 \tag{2.12}$$

for the dynamic equation. Equation (2.12) can be furtherly split into terms that, singularly analyzed, lead to spatial convolution elements. Moreover, expliciting all the dependencies, the dynamic interaction force becomes:

$$\begin{aligned}&\int_{\boldsymbol{\xi}\in\mathbb{R}} (\boldsymbol{g}_0\boldsymbol{\varepsilon} + f_0\boldsymbol{\varepsilon})\, dV = \\ &\int_{\boldsymbol{\xi}\in\mathbb{R}} [\boldsymbol{g}_0(\boldsymbol{x},\boldsymbol{\xi})\ \boldsymbol{\varepsilon}(\boldsymbol{x},\boldsymbol{\xi},t) + f_0(\boldsymbol{x},\boldsymbol{\xi})\ \boldsymbol{\varepsilon}(\boldsymbol{x},\boldsymbol{\xi},t)]\, dV = \\ &\int_{\boldsymbol{\xi}\in\mathbb{R}} \{\boldsymbol{g}_0(\boldsymbol{x},\boldsymbol{\xi})\,[\boldsymbol{w}(\boldsymbol{x},t) - \boldsymbol{w}(\boldsymbol{\xi},t)] + f_0(\boldsymbol{x},\boldsymbol{\xi})\,[\boldsymbol{w}(\boldsymbol{x},t) - \boldsymbol{w}(\boldsymbol{\xi},t)]\}\, dV\end{aligned} \tag{2.13}$$

Developing each additive term, we have:

$$\int_{\boldsymbol{\xi}\in\mathbb{R}} \boldsymbol{g}_0(\boldsymbol{x},\boldsymbol{\xi})\ \boldsymbol{w}(\boldsymbol{x},t)dV = p\,(\boldsymbol{g}_0 * 1)\cdot\mathbf{w} \tag{2.14a}$$

$$-\int_{\boldsymbol{\xi}\in\mathbb{R}} \boldsymbol{g}_0(\boldsymbol{x},\boldsymbol{\xi})\ \boldsymbol{w}(\boldsymbol{\xi},t)dV = -[\boldsymbol{g}_0 * (\mathbf{w})] \tag{2.14b}$$

$$\int_{\boldsymbol{\xi}\in\mathbb{R}} f_0(\boldsymbol{x},\boldsymbol{\xi})\ \boldsymbol{w}(\boldsymbol{x},t)dV = (f_0 * 1)\mathbf{w} \tag{2.14c}$$

$$-\int_{\boldsymbol{\xi}\in\mathbb{R}} f_0(\boldsymbol{x},\boldsymbol{\xi})\ \boldsymbol{w}(\boldsymbol{\xi},t)dV = -[f_0 * (\mathbf{w})] \tag{2.14d}$$

where $*$ is the convolution operator, and both f_0 and $\boldsymbol{g}_0$ are evaluated at $\boldsymbol{\xi} = \mathbf{0}$. Equation (2.12) becomes:

$$\begin{aligned}\rho\mathbf{w}_{tt} - \frac{E}{2(1+\nu)}\left[\nabla^2\mathbf{w} + \frac{1}{1-2\nu}\nabla\left(\nabla\cdot\mathbf{w}\right)\right] + \\ + (\boldsymbol{g}_0 * 1)\cdot\mathbf{w} - (\boldsymbol{g}_0 * \mathbf{w}) + (f_0 * 1)\mathbf{w} - (f_0 * \mathbf{w}) = 0\end{aligned} \tag{2.15}$$

An interesting result is achieved: in fact, if the hypothesis of small displacements stands, the equation of motion becomes a summation of few convolution integrals, leading to closed form solutions of the wave equation, focusing the attention in resolving the dynamic equation (2.15).

The proposed equation is a general law, basis of some study cases, developed during the PhD and summarized in this document. The following chapters present the results obtained for one and two dimensional metamaterials with some examples of long-range interaction forces.

Part I

One-dimensional waves in metamaterials

The wave dynamics analysis starts with the evaluation of the wave propagation phenomenon in one-dimensional unbounded media subject to long-range interaction, for a better comprehension and evaluation of the wave propagation in elastic metamaterials. Equation (2.15), consequently, reduces in the following expression:

$$\rho\frac{\partial^2 w}{\partial t^2}+\Box+(g_0*1)\,w-(g_0*w)+(f_0*1)w-(f_0*w)=0 \tag{2.16}$$

where $\Box$ represents the local elasticity operator. To this purpose, two models are analyzed in the following sections:

- D'Alembert based media;
- Euler-based media.

The former formulation starts from a local elasticity rod-like unbounded media with long-range interactions, while the latter models a Euler-Bernoulli beam-like infinite structure with long-range connections involving the external surfaces of the media.

Chapter 3

Long-range interactions in a D'Alembert waveguide

The D'Alembert based model is typical of elastic media subject to pressure waves, and in this section, a rod-like long-range structure is presented.

The local elasticity in homogeneous cross-section constant media, subject to pressure waves, for cross-section unit is $-E\dfrac{\partial^2 w}{\partial x^2}$, and equation (2.16) consequently becomes:

$$\rho\frac{\partial^2 w}{\partial t^2} - E\frac{\partial^2 w}{\partial x^2} + (g_0 * 1)\, w - (g_0 * w) + (f_0 * 1)w - (f_0 * w) = 0 \tag{3.1}$$

A general solution for the equation of motion can be assumed as follows:

$$w(x,t) = \iint_{\infty}^{\infty} W(k,\omega) e^{\jmath(kx-\omega t)}\, dk\, d\omega \tag{3.2}$$

where k is the propagation wavenumber $[rad/m]$ and ω is the propagation frequency, $[rad/s]$. In order to evaluate wave propagation in one-dimensional rod-like structures, the general solution is introduced in the equation of motion and a dispersion relationship is found.

The dispersion relationship is a mathematical law, namely a function, that relates the time (frequency) and space (wavenumber) domains. To each fixed frequency, none, one or a set of numerable correspondent wavenumbers solve the equation, and vice versa by variating the wavenumber.

In the following sections, three interaction forces are analyzed:

- Gauss[3]-like;
- Laplace[4]-like;
- Rectangular.

---

[3] Johann Carl Friedrich Gauss (April 30th, 1777 - February 23rd, 1855) German mathematician and physicist

[4] Pierre-Simon, marquis de Laplace (March 23rd, 1749 - March 5th, 1827) French scholar whose work was important to the development of mathematics, statistics, physics and astronomy

The Gauss- and Laplace-like forces are interaction forces rapidly decaying within the distance, and derive from the Gauss (Normal) and Laplace (Double Exponential) distributions, respectively. The distribution term, capable of the interaction magnitude, is multiplied by the $\boldsymbol{r}$ vector, to preserve the action-reaction principle. This is the reason for the presence of the *-like* suffix.
The rectangular force is a constant stiffness interaction defined in a limited window of the distance r.

3.1 Gauss-like

The Gauss-like interaction is a physical-mathematical model capable of describing the force exchanged between two particles at distance $\boldsymbol{r}$. The expression of the magnitude term is the following:

$$f(|\boldsymbol{r}|) = \mu e^{-\frac{|\boldsymbol{r}|^2}{\beta^2}} \tag{3.3}$$

The parameter μ (real, positive or negative) is a magnitude coefficient and β (real and positive) is the interaction length, that takes into account the interaction spread in the distance domain. In Figure 3.1 some Gauss-like examples are presented.
The Gauss-like force, thanks to the presence of the normal distribution, guarantees a distance-dependent decaying, moreover, the skew-symmetric behavior preserves the action-reaction principle decay. Note that the choice of such force model is corroborated by the simplicity of it, in fact, the behavior is controlled by the choice of the two parameters μ and β, with a behavior that mimics several non-local interactions, naturally long-range, such as electrostatic, magneto-static or gravitational interaction, that generally follow a power-like interaction model.

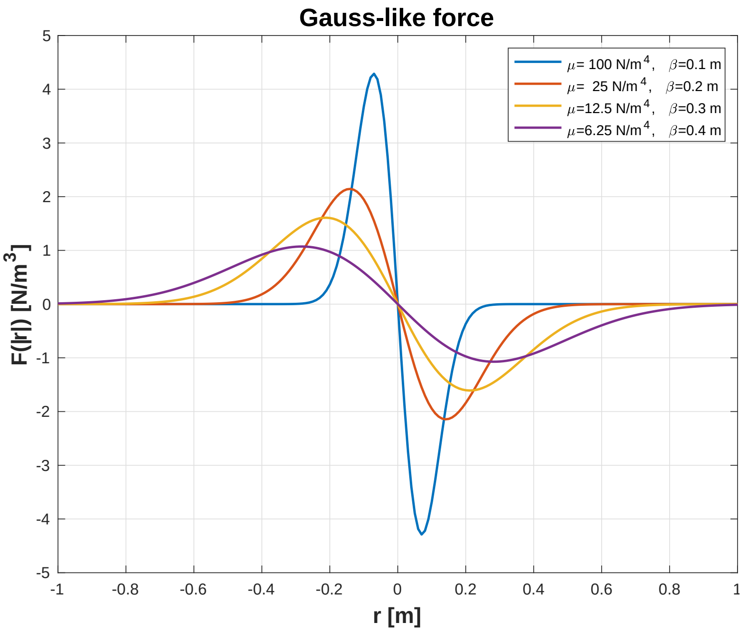

Figure 3.1. Gauss-like force as function of the distance vector $\boldsymbol{r} = \boldsymbol{x} - \boldsymbol{\xi}$

The power-like force, at $\boldsymbol{r}=0$ exhibits a singularity. It would happen in the only case in which one of the particles collapses with another. However, this is a physically unreachable condition, so that, power-law type interactions can be approximated with Gauss-like interactions.

3.1.1 Analytical solution

The Gauss-like force is introduced into equation (3.1): collecting the convolutions, so that it becomes:

$$\rho\frac{\partial^2 w}{\partial t^2}-E\frac{\partial^2 w}{\partial x^2}+\left[(g_0+f_0)*1\right]w-\left[(f_0+g_0)*w\right]=0 \tag{3.4}$$

Introducing the actual expressions of f_0 and g_0, and introducing $h_0=f_0+g_0$ as follows:

$$f_0(x-\xi)=\mu e^{-\frac{(x-\xi)^2}{\beta^2}} \tag{3.5a}$$

$$g_0(x-\xi)=-2\frac{\mu}{\beta^2}(x-\xi)^2 e^{-\frac{(x-\xi)^2}{\beta^2}} \tag{3.5b}$$

$$h_0(x-\xi)=f_0(x-\xi)+g_0(x-\xi)=\mu\left[1-\frac{2}{\beta^2}(x-\xi)^2\right]e^{-\frac{(x-\xi)^2}{\beta^2}} \tag{3.5c}$$

equation (3.4) becomes:

$$\rho\frac{\partial^2 w}{\partial t^2}-E\frac{\partial^2 w}{\partial x^2}+\left[\mu\left(1-\frac{2}{\beta^2}x^2\right)e^{-\frac{x^2}{\beta^2}}*1\right]w-\mu\left(1-\frac{2}{\beta^2}x^2\right)e^{-\frac{x^2}{\beta^2}}*w=0 \tag{3.6}$$

The equation of motion is thus reduced into the sum of four terms, but they reduce to three, because the convolution among the parenthesis of the third term: $\mu\left(1-\frac{2}{\beta^2}x^2\right)e^{-\frac{x^2}{\beta^2}}*1$ is null:

$$\begin{aligned}
&\mu\left(1-\frac{2}{\beta^2}x^2\right)e^{-\frac{x^2}{\beta^2}}*1=\\
&\frac{\partial}{\partial x}\left(\mu\, x\, e^{-\frac{x^2}{\beta^2}}\right)*1=\\
&\mu\, x\, e^{-\frac{x^2}{\beta^2}}*\frac{\partial}{\partial x}(1)=\\
&\mu x\, e^{-\frac{x^2}{\beta^2}}*0=0
\end{aligned} \tag{3.7}$$

Consequently, equation (3.6) reads:

$$\rho\frac{\partial^2 w}{\partial t^2}-E\frac{\partial^2 w}{\partial x^2}-\mu\left(1-\frac{2}{\beta^2}x^2\right)e^{-\frac{x^2}{\beta^2}}*w=0 \tag{3.8}$$

Some considerations about the linearization are needed, in fact, equation (3.8) is useful only if the linearization hypothesis stands; therefore, equation (3.6), and equation (3.8), are valid under the assumption $|\varepsilon|\ll|x-\xi|$. Since $\dfrac{|\varepsilon|}{|x-\xi|}=\dfrac{|w(x)-w(\xi)|}{|x-\xi|}$

the strain should be $\ll 1$, at least of the order of 10^{-1}.
According to the general solution $w(x,t) = w_0 e^{\jmath(kx-\omega t)}$ the strain is $\dfrac{\partial w}{\partial x} = \jmath k w_0 e^{\jmath(kx-\omega t)}$ and the linearization is verified for $\dfrac{\partial w}{\partial x} \ll 1$, i.e. for $w_0 k \ll 1$. Introducing the nondimensional wavenumber $K = \beta k$, it produces $\left|\dfrac{w_0 K}{\beta}\right| \ll 1$ hence $K \ll \dfrac{\beta}{w_0}$.
The obtained relationship indicates that, when the propagation regime is defined, the intrinsic length and the vibration amplitude are mutually defined. In the following sections, the evaluation will focus on low wavenumbers ($K < 6$), where interesting phenomena emerge, in particular when K is in the order of ~ 1; above the interest bandwidth, the long-range model practically collapses into the standard short range elastic waveguide. It means that the linearization is valid when the oscillation amplitude w_0 is much smaller than the intrinsic characteristic β: $w_0 \ll \beta$.
The equation of motion, describing the behavior of the physical system, intrinsically contains the dispersion relationship; to obtain it, the displacement needs to be mathematically collected, and the resulting factor is the dispersion relationship. To collect the displacement, it is necessary to transform the convolution into a product. For this reason domain transforms are needed.
Two Fourier[5] transforms[6] are applied to the equation of motion, in time to frequency and in space to wavenumber domains.
Taking into account the general solution of the equation of motion, equation (3.2), equation (3.8) reads into:

$$-\rho\omega^2 W + E k^2 W - \frac{\mu\beta^3}{2\sqrt{2}} k^2 e^{-\frac{(\beta k)^2}{4}} W = 0 \tag{3.9}$$

where $W = W(k,\omega) = \mathcal{F}_{t\to\omega}\left\{\mathcal{F}_{x\to k}\left[w(x,t)\right]\right\}$.
Collecting W and applying a sign change we have:

$$\left[\rho\omega^2 - E k^2 + \frac{\mu\beta^3}{2\sqrt{2}} k^2 e^{-\frac{(\beta k)^2}{4}}\right] W = 0 \tag{3.10}$$

Equation (3.10) is valid for any possible displacement, implying that the factor needs to be null.
Consequently, the dispersion relationship for the one-dimensional rod based waveguide with Gauss-like long-range interaction is obtained:

$$\rho\omega^2 - E k^2 + \frac{\mu\beta^3}{2\sqrt{2}} k^2 e^{-\frac{(\beta k)^2}{4}} = 0 \tag{3.11}$$

---

[5] Jean-Baptiste Joseph Fourier (March 21st, 1768 - May 16th, 1830) French mathematician and physicist

[6] both time and space interest domains spread from $-\infty$ to $+\infty$

To reduce the number of governing parameters, two additional nondimensional groups are introduced, and, remembering the nondimensional wavenumber K:

$$\Omega = \sqrt{\frac{\rho}{E}}\beta\omega \qquad \text{nondimensional frequency} \tag{3.12a}$$

$$K = \beta k \qquad \text{nondimensional wavenumber} \tag{3.12b}$$

$$\chi = \frac{\mu\beta^3}{2\sqrt{2}E} \qquad \text{stiffness ratio} \tag{3.12c}$$

obtaining the nondimensional dispersion relationship:

$$\Omega^2 + K^2\left(\chi e^{-\frac{K^2}{4}} - 1\right) = 0 \tag{3.13}$$

The nondimensional group in equation (3.12c) is named *ratio* because, introducing the long-range stiffness: $E^* = \frac{\mu\beta^3}{2\sqrt{2}}$, (real, positive or negative, according to the sign of μ) the nondimensional group χ is exactly the ratio between the long-range (nonlocal) stiffness and the short-range (local) stiffness.

The expression obtained in equation (3.13) links the frequency to the wavenumber in a relation that is ruled by one parameter only: the stiffness ratio χ. For one-dimensional second order Gauss-like waveguides, several interesting phenomena emerge, just acting on χ.

Because of the presence of transcendent terms that do not allow a closed form solution in the time frequency domain, the dispersion equation is solved in the wavenumber domain in both dimensional and nondimensional solutions:

$$\omega = \pm k\sqrt{\frac{E}{\rho} - \frac{\mu\beta^3}{2\sqrt{2}\rho}e^{-\frac{(\beta k)^2}{4}}} \tag{3.14}$$

$$\Omega = \pm K\sqrt{1 - \chi e^{-\frac{K^2}{4}}} \tag{3.15}$$

The solution in the frequency domain is numerically obtained, and it is presented in Appendix A. In the following paragraphs, the nondimensional dispersion relationship is analyzed.

The propagation is analyzed in terms of the stiffness ratio χ, especially in terms of magnitude and sign.

Three different regions are identified:

- Strongly negative χ, with $\chi \ll -1$, where a strong long-range repulsion is observed;
- Low magnitude χ, with $-1 \leq \chi \leq 1$, where a quasi-neutral behavior is observed;
- Strongly positive χ, with $\chi \gg 1$, where a strong long-range attraction is observed.

The three regions show unusual behaviors at low wavenumbers ($K <\sim 5.5$), while the long-range waveguide, regardless of the magnitude and the sign of χ, show the same trend, asymptotically converging to the solution of the short-range waveguide, thereafter called with the notation D'Alembert[7] who solved the short-range infinite elastic waveguide system [65].

Strongly negative χ

Under a mathematical point of view, when $\chi \ll -1$, equation (3.15) admits real solutions, positive or negative, according to the sign of the root. In Figure 3.2 some values of the positive solutions of the frequency are plotted, and interesting phenomena emerge.

The dispersion relationships depicted in Figure 3.2 show similar properties. At low wavenumbers they present a high slope that quickly vanishes, up to obtain a local maximum; from then on, the curve decreases up to a valley, a local minimum, until they rapidly converge to the short-range waveguide, in dashed red.

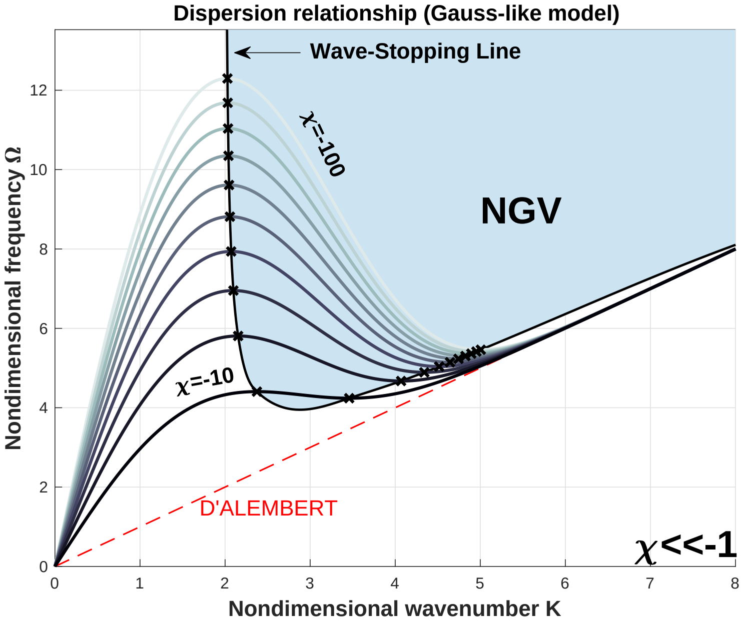

Figure 3.2. Dispersion curves for the 1D 2^{nd} order Gauss-like model with strongly negative χ

The slope of the curve, as widely discussed later, is directly correlated to the wave packet envelope speed; when it is null, as in local points, the envelope does not travel [66], evidencing the presence of wave-stopping phenomenon. To this aim, a wave-stopping line has been depicted in Figure 3.2, indicating the K, Ω couple where the phenomenon verifies. Moreover, when the slope becomes negative, the wave packet travels in opposite direction with respect to the disturbances peaks, so that a NGV (Negative Group Velocity) region is highlighted. The non highlighted region indicates a conventional dynamic behavior.

It is evident that for low magnitude negative χ, the waveguide does not present

---

[7] Jean-Baptiste Le Rond d'Alembert (Paris, November 16th, 1717 - Paris, October 29th, 1783) French mathematician, mechanician, physicist, philosopher, and music theorist

wave-stopping and reverse propagation (as in the NGV region). These values are discussed in the next paragraph.

Low magnitude χ

When the stiffness ratio magnitude is low ($|\chi| < 1$), either positive or negative, the dispersion equation allows real frequencies. In this region, nevertheless, neither wave-stopping, nor reverse propagation phenomena appear. In Figure 3.3 some dispersion curves are presented.

It is evident that the curves are barely different from the D'Alembert line, in that, according to the meaning of the χ parameter, the local elasticity is stronger than the nonlocal interaction. Further discussion will be made in the wave speed analysis sections that follow, because such kind of dispersion curves provokes a modal migration between frequency bandwidths. As for the previous case, also when $|\chi| \leq 1$ for $K >\sim 4$ (not depicted in Figure 3.3 to highlight the lower wavenumbers behavior), the behavior mimics the D'Alembert waveguide.

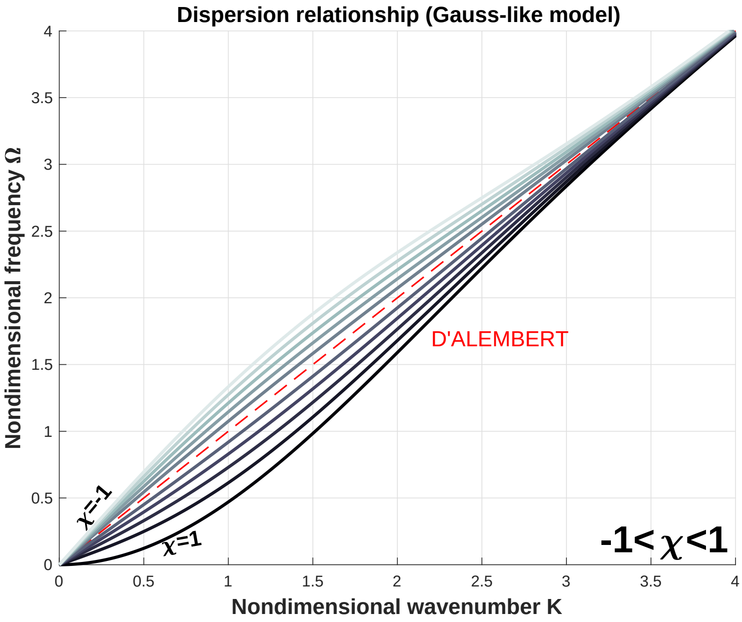

Figure 3.3. Dispersion curves for the 1D 2^{nd} order Gauss-like model with low magnitude χ

Strongly positive χ

When $\chi > 1$ the dispersion curves is not real for any wavenumber values; in fact, for $K \in [0; K_0]$ the dispersion relationship provides purely imaginary frequencies. K_0 is calculated starting from equation (3.15), as follows. By imposing K_0 as the wavenumber value when the square root argument is null, namely the value in which there is the shift from purely imaginary to real solutions of the dispersion relationship:

$$
\begin{aligned}
1-\chi e^{-\frac{K_0^2}{4}} &= 0\\
\chi e^{-\frac{K_0^2}{4}} &= 1\\
e^{-\frac{K_0^2}{4}} &= \frac{1}{\chi}\\
e^{-\frac{K_0^2}{4}} &= \chi^{-1}\\
\ln\left(e^{-\frac{K_0^2}{4}}\right) &= \ln\left(\chi^{-1}\right)\\
-\frac{K_0^2}{4} &= -\ln\left(\chi\right)\\
K_0^2 &= 4\ln\left(\chi\right)\\
K_0 &= 2\sqrt{\ln\left(\chi\right)}
\end{aligned}
\tag{3.16}
$$

the evaluation of negative wavenumbers is not in the interests of this PhD project.

When a purely imaginary solution appears, either the positive and the negative

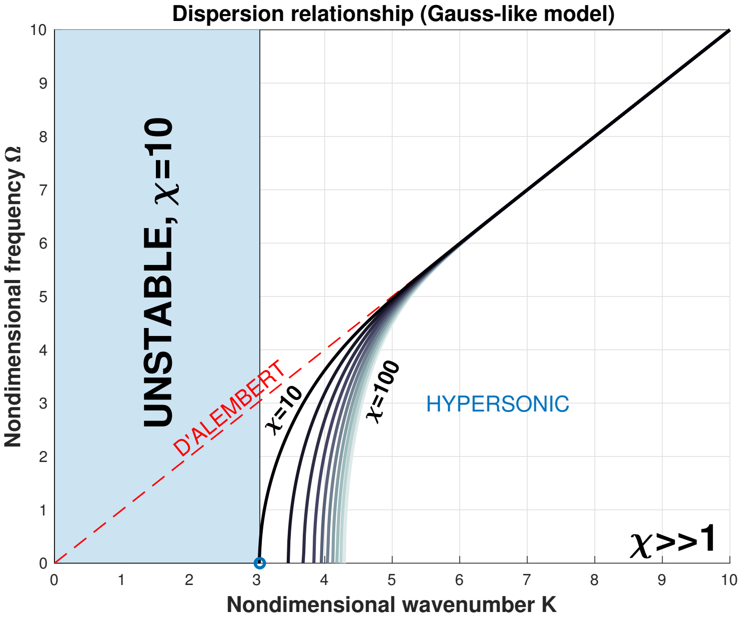

Figure 3.4. Dispersion curves for the 1D 2^{nd} order Gauss-like model with strongly positive χ

solutions of the dispersion relationship leads to instability regions. In fact, defining $\Omega(\bar{K})_{1,2} = \pm\jmath\Omega_{1,2} = \pm\jmath C_\Omega\omega_{1,2}$, with $\bar{K}\in[0,K_0]$ and $C_\Omega = \sqrt{\frac{\rho}{E}}\beta$ the nondimensional to dimensional conversion coefficient, the single element of the displacement solution diverges, as follows:

$$w_1(x,t) = w_{0_1} e^{\jmath(kx - \jmath C_\Omega \omega_1 t)} = w_{0_1} e^{C_\Omega \omega_1 t} e^{\jmath kx} \tag{3.17a}$$

$$w_2(x,t) = w_{0_2} e^{\jmath(kx + \jmath C_\Omega \omega_2 t)} = w_{0_2} e^{-C_\Omega \omega_2 t} e^{\jmath kx} \tag{3.17b}$$

$$\tag{3.17c}$$

The first solution diverge when $t \to +\infty$, the second comes from a divergent condition, i.e. when $t \to -\infty$. In Figure 3.4, an instability region has been depicted when $K \in [0, K_0]$.

The slope of the dispersion curves, right at the beginning of the stable region, is very high. This condition will be accurately discussed later, but similar trends indicate a very high propagation speed, if compared to the pressure waves propagation speed.

3.1.2 Wave speed analysis

To analyse wave propagation, two velocities must be evaluated, namely the phase velocity and the group velocity, two quantities capable of highlighting the presence of peculiar propagation phenomena, such as wave-stopping or superluminal regions.

Phase velocity

The phase velocity describes the motion of a single elementary wavelet in the carrier [67], and it is defined by the ratio between the frequency and the wavenumber. Introducing a reference phase velocity $c = \sqrt{\frac{E}{\rho}}$ corresponding to the solution of the short-range elastic waveguide, the dimensional phase velocity in Gauss-like one-dimensional structures is evaluated from the solution of the dimensional dispersion relationship, equation (3.15), obtaining its nondimensional counterpart:

$$\begin{aligned}
c_\phi = \frac{\omega}{k} &= \pm\sqrt{\frac{E}{\rho} - \frac{\mu\beta^3}{2\sqrt{2}\rho} e^{-\frac{(\beta k)^2}{4}}} \\
&= \pm\sqrt{\frac{E}{\rho}}\sqrt{1 - \frac{\mu\beta^3}{2\sqrt{2}E} e^{-\frac{(\beta k)^2}{4}}} \\
&= \pm c\sqrt{1 - \frac{\mu\beta^3}{2\sqrt{2}E} e^{-\frac{(\beta k)^2}{4}}} \\
&= \pm c\sqrt{1 - \chi e^{-\frac{K^2}{4}}} \\
&= c\left(\pm\sqrt{1 - \chi e^{-\frac{K^2}{4}}}\right) \\
&= c\left(\pm\frac{K\sqrt{1 - \chi e^{-\frac{K^2}{4}}}}{K}\right) \\
&= c\frac{\Omega}{K}
\end{aligned} \tag{3.18}$$

introducing $C_\phi = \frac{\Omega}{K}$ as the nondimensional phase velocity, from equation (3.18):

$$C_\phi = \frac{\Omega}{K} = \frac{c_\phi}{c} = \pm\sqrt{1 - \chi e^{-\frac{(\beta k)^2}{4}}} \tag{3.19}$$

The phase velocity analysis strictly follows the classifications made for the dispersion relationship, namely in terms of magnitude and sign of the stiffness ratio χ.

Strongly negative χ

For strongly negative stiffness ratios, the phase velocity follows a monotonically decreasing behavior[8] with respect to the nondimensional wavenumber, as depicted in Figure 3.5. As a consequence, for each value of χ, the maximum value is obtained at the initial value $K = 0$, and each curve asymptotically converges to the D'Alembert line $C_\varphi = 1$.

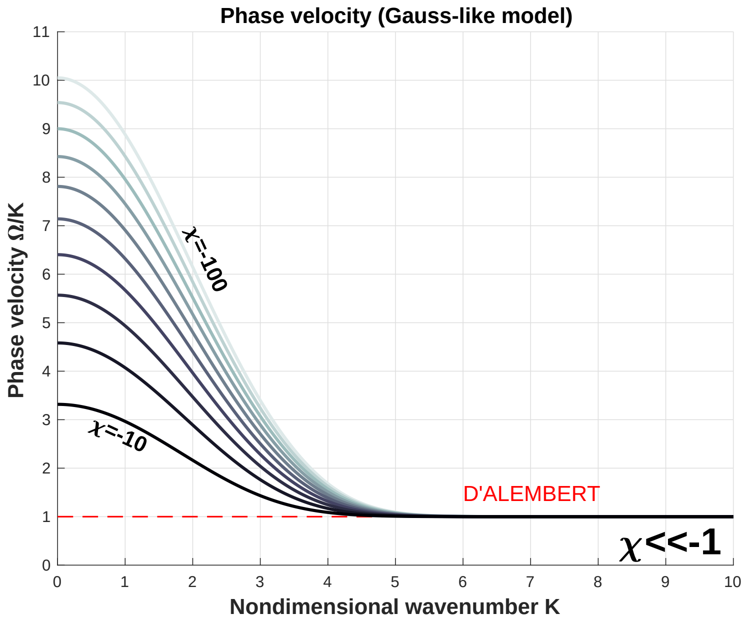

Figure 3.5. Phase velocities for the 1D 2$^{\text{nd}}$ order Gauss-like model with strongly negative χ

From a mechanical point of view, it means that each wavelet travels with a faster speed with respect to the others with higher wavenumbers. Non-constant phase speed means also that the general shape of the perturbation is not preserved and it does not travel in a compact shape along the waveguide, in contrast with what happens for the D'Alembert waveguide, where a constant phase velocity is present and the shape of the perturbation is preserved.

---

[8] if $\chi \ll -1$, $\dfrac{\partial C_\varphi}{\partial K} = \dfrac{\chi e^{-\frac{K^2}{4}}}{4\sqrt{1 - \chi e^{-\frac{K^2}{4}}}} K \neq 0 \; \forall \; K \in [0, +\infty)$

Low magnitude χ

When the magnitude of χ decreases, also the the initial point of the phase velocity decreases its value, getting closer to the limit case, $\chi = 0$ in which the D'Alembert case is obtained[9], while the trend is completely preserved. With low, but positive, stiffness ratios, the trend flips, and the initial value is between 0 and 1, and the value of the phase velocity asymptotically converges to 1: its maximum value. In Figure 3.6 some examples are presented:

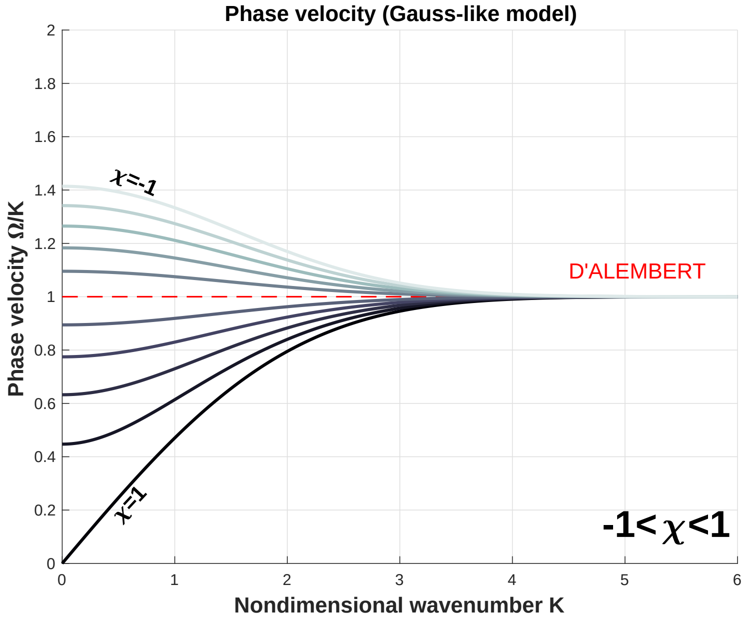

Figure 3.6. Phase velocities for the 1D 2$^{\text{nd}}$ order Gauss-like model with low magnitude χ

The extremum $\chi = 1$ indicates the maximum value of χ for which only real solutions appear, and, for this value, the minimum phase velocity (without instability) can be reached: $C_\varphi = 0$. Mathematically speaking, a constant perturbation along the waveguide ($K = 0$) in such medium has null phase velocity.

Strongly positive χ

For strongly positive values of χ, the value of the phase velocity is similar to the dispersion relationship; it starts close to zero barely right of the instability line, and then it tends to the D'Alembert model, as depicted in Figure 3.7.
Some interesting behavior will emerge in the next paragraph, when the propagation in terms of group velocity is analyzed.

Group velocity

The group velocity describes the speed of modulation [67] and it is defined as the derivative of the frequency with respect to the wavenumber. In an analogous way

---

[9] When $\chi \to 0$, $E \gg \mu\beta^3$: equation (3.13)tends to the D'Alembert wave equation

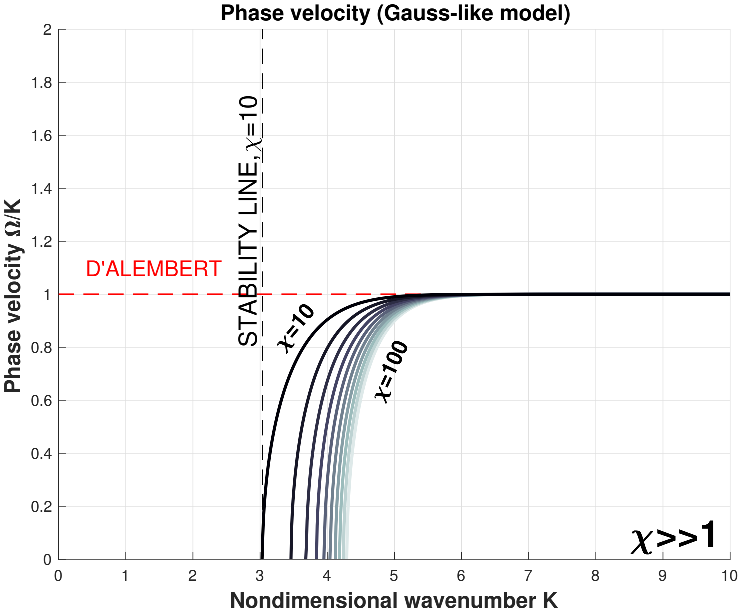

Figure 3.7. Phase velocities for the 1D 2$^{\text{nd}}$ order Gauss-like model with strongly positive χ

with respect to the phase velocity, the group velocity is calculated:

$$\begin{aligned} c_g = \frac{\partial \omega}{\partial k} &= \pm\frac{\partial}{\partial k}\left[k\sqrt{\frac{E}{\rho}-\frac{\mu\beta^3}{2\sqrt{2}\rho}e^{-\frac{(\beta k)^2}{4}}}\right] \\ &= \pm\sqrt{\frac{E}{\rho}}\frac{\partial}{\partial k}\left[k\sqrt{1-\frac{\mu\beta^3}{2\sqrt{2}E}e^{-\frac{(\beta k)^2}{4}}}\right] \\ &= \pm c\frac{\partial}{\partial k}\left[k\sqrt{1-\chi e^{-\frac{(\beta k)^2}{4}}}\right] \\ &= \pm c\frac{\partial}{\partial k}\left[\frac{\beta k\sqrt{1-\chi e^{-\frac{(\beta k)^2}{4}}}}{\beta}\right] \\ &= \pm c\frac{\partial}{\partial(\beta k)}\left[(\beta k)\sqrt{1-\chi e^{-\frac{(\beta k)^2}{4}}}\right] \\ &= \pm c\frac{\partial}{\partial K}\left(K\sqrt{1-\chi e^{-\frac{K^2}{4}}}\right) \\ &= c\frac{\partial \Omega}{\partial K} \end{aligned} \tag{3.20}$$

introducing $C_g = \frac{\partial \Omega}{\partial K}$ as the nondimensional group velocity, from equation (3.20) we have:

$$C_g = \frac{\partial \Omega}{\partial K} = \frac{c_g}{c} = \pm\left(\sqrt{1-\chi e^{-\frac{K^2}{4}}} + \frac{\chi e^{-\frac{K^2}{4}}}{4\sqrt{1-\chi e^{-\frac{K^2}{4}}}}K^2\right) \tag{3.21}$$

Strongly negative χ

When $\chi \ll -1$ interesting phenomena emerge; in fact the group velocity shows a sign change. When the group velocity vanishes, wave-stopping phenomena appear. It means that the envelope of a narrow banded group of wavelets, if the average wavenumber stands in one of the wave-stopping points, does not travel along the waveguide.

Moreover, as shown in Figure 3.8, each curve has two wave-stopping points. These points define a bandwidth in which the group velocity is negative. In this region, while a single banded wavelet travels along the waveguide in one direction, the envelope of a wave packet moves backwards. This region is called Negative Group Velocity (NGV) region, where the *negative* adjective is used to identify the sign of the envelope speed if compared to the wavelet speed. The width of the NGV area is as wide as much higher is the magnitude of χ, as visible in Figure 3.2.

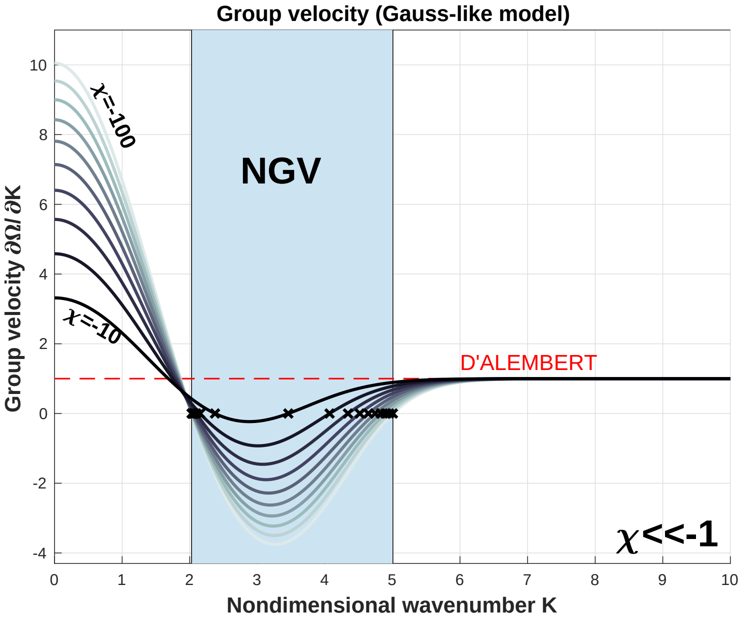

Figure 3.8. Group velocities for the 1D 2^{nd} order Gauss-like model with strongly negative χ

Low magnitude χ

When the magnitude of χ decreases, no wave-stopping or negative group velocity phenomena emerge, but rather a *mode migration* phenomenon appears. To describe the mode migration phenomenon, an additional quantity must be introduced: the *eigenstate density*.

The eigenstate (or modal) density [66] is defined as the number of eigenstates in a certain bandwidth, and it is evaluated as follows for nondimensional quantities:

$$\frac{dN}{d\Omega} \propto \frac{d}{d\Omega}\left(\frac{K}{\pi}L\right)$$

for reference length ($L = \pi$)

$$\propto \frac{dK}{d\Omega} = \frac{1}{C_g} \tag{3.22}$$

$$\frac{dN}{d\Omega} \propto \frac{1}{C_g} = \pm\frac{4\sqrt{1-\chi e^{-\frac{K^2}{4}}}}{4+\chi\left(K^2-4\right)e^{-\frac{K^2}{4}}}$$

As depicted in Figure 3.9 and highlighted in Figure 3.10, all the curves show a trend

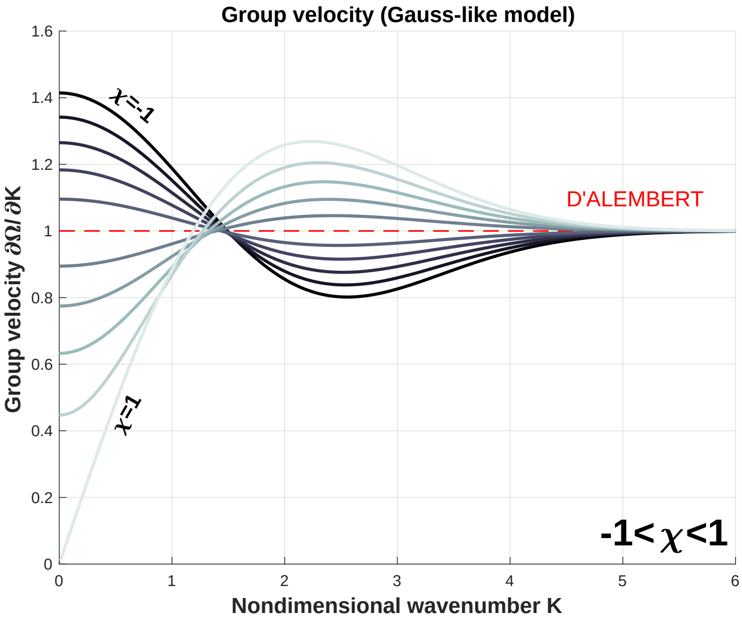

Figure 3.9. Group velocities for the 1D 2^{nd} order Gauss-like model with low magnitude χ

around the D'Alembert reference, in particular two curve branches are identified: the first overcomes the D'Alembert group velocity, while in the second the group velocity is smaller. In terms of eigenstate density, the situation flips. A *folding wavenumber* $k_0 \sim 1,4$ is identified, as the wavenumber that divides the two branches.
In Figure 3.11, for instance, the eigenstate density for $\chi = 0,4$ is depicted. When $0 < \chi < 1$, at lower wavenumbers, the eigenstate density increases, while it is lower than the D'Alembert reference from k_0 on. The *migration* term is used because of the variation of the density has a precise trend; in fact, the eigenstates gained in $[0, k_0]$ is equal to the ones lost in $[k_0, +\infty)$. From a mathematical point of view:

$$\int_0^{k_0}\left(\frac{dN}{d\Omega}-1\right)d\Omega = \int_{k_0}^{+\infty}\left(1-\frac{dN}{d\Omega}\right)d\Omega \tag{3.23}$$

According to the mode migration phenomenon, an eigenstate packet *travels*, migrating from high to low frequencies, folding around k_0. The opposite phenomenon appears when $-1 < \chi < 0$, where the migration goes from low to high frequencies,

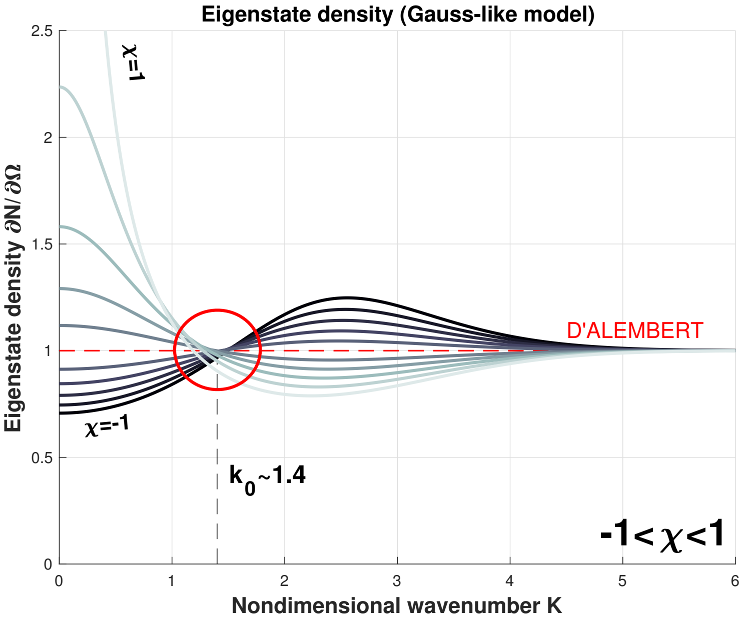

Figure 3.10. Eigenstate density for the 1D 2^{nd} order Gauss-like model with strongly positive χ

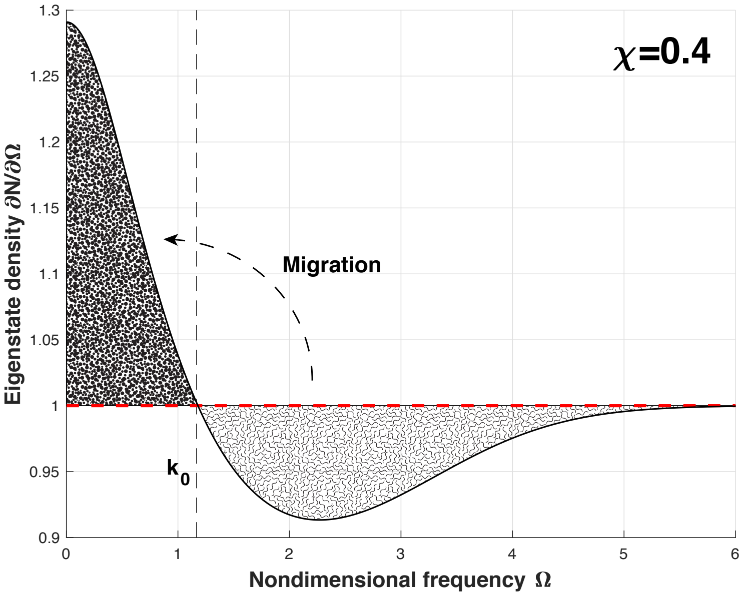

Figure 3.11. Eigenstate density for the 1D 2^{nd} order Gauss-like model with $\chi = 0,4$ as function of Ω

as shown in Figure 3.10.

Strongly positive χ

For $\chi \gg 1$ neither wave-stopping phenomena, nor mode migration appear. Instead, interesting phenomena in the wave propagation studies emerge: superluminal group velocity regions.
Right after the stability line, as depicted in Figure 3.12, the group velocity reaches very high values. Theoretically, in this region infinite group velocity could be reached, no upper limit is mathematically present, so that, speeds higher than the speed of light can be reached[10].
In general, the group velocity is always higher that the D'Alembert reference, as shown in Figure 3.12, and then, with a very high slope, the group velocity decreases to asymptotically reach the short-range waveguide. In the following section, some numerical simulations follow to corroborate the results arisen from the model.

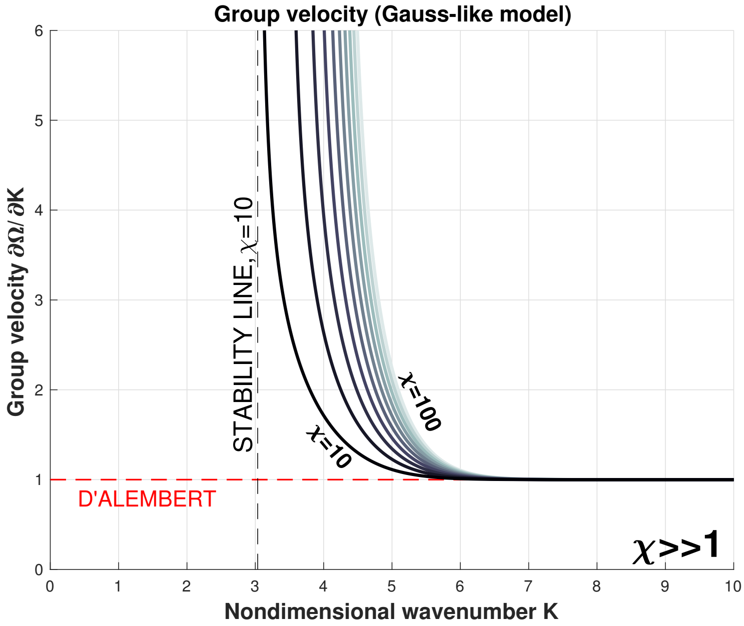

Figure 3.12. Group velocities for the 1D 2^{nd} order Gauss-like model with strongly positive χ

3.1.3 Simulations

Some numerical simulations have been carried out to test the effects of the long-range interaction, and to corroborate the developed models, demonstrating the presence of the hypothesized phenomena.
The numerical simulations have been performed for a continuous finite rod clamped at the ends, and subjected to long-range interaction as in Figure 3.13. The physical quantities are defined as follows:

- mass density: 1320 kg/m^3;

---

[10] this consideration is not in contrast with the impossibility to overcome the speed of light, in fact, neither the group nor the phase velocity indicate the information transmission velocity, whose maximum value is defined by the speed of light [68].

- elastic modulus: 1.6 MPa;
- rod length (l) : 100 m;
- long-range interaction length (β): 0.32 m;

while the long-range force intensity is ruled by the simulation. In fact, three simulations have been run to trace the three scales of the stiffness ratio described in the previous sections.

In all the following simulations, the initial condition has been chosen to excite several wavelengths (200), in a wavenumber domain capable of letting all the propagation phenomena, the ones described by the analysis of the dispersion curve.

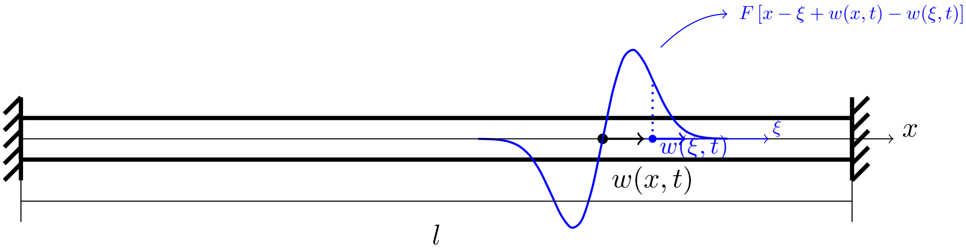

Figure 3.13. Geometry of the rod used to simulate the long-range models

Strongly negative χ

The simulation for the strongly negative stiffness ratio has been evaluated with a Gauss-like force magnitude as follows:

- long-range interaction length (μ): $-8.64\text{x}10^6$ N/m^4

leading to a stiffness ratio $\chi = -42.7$.

The displacement map in Figure 3.14 shows how different wavenumbers spread along the waveguide. It is possible to distinguish low wavenumbers that rapidly

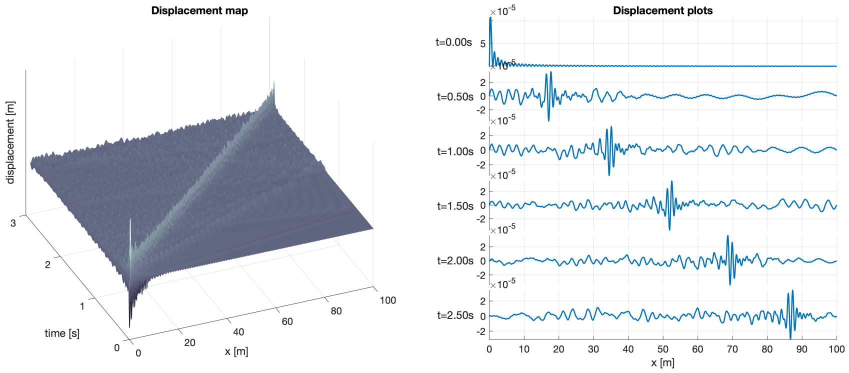

Figure 3.14. Displacement map (left) and plots (right) for 1D waveguide with strongly negative χ subject to Gauss-like interaction

reach the resting extrema of the waveguide. A backbone perturbation propagates with a speed comparable to the D'Alembert propagation speed. This quasi-non dispersive propagation is composed by higher wavenumbers, while this wavefront propagates, a tail evolve with slower speeds in the waveguide.
The propagation map is compared to the analytical dispersion relationship. To obtain a simulated dispersion relationship, a 2-D Discrete Fourier Transform has been applied [69], in space and time domain. In Figure 3.15 the discrete dispersion relationship is compared to the analytical result, where the lightest regions highlight a match between time and space frequencies.

A graphical analysis shows that the expected behavior is found also in the numerical simulations. The analysis shows not just a qualitative match, but the behavior has been completely rebuilt.
Such result was not granted, in that the limitations in the length could lead to unbalancing phenomena in the borders, modifying the static solution.

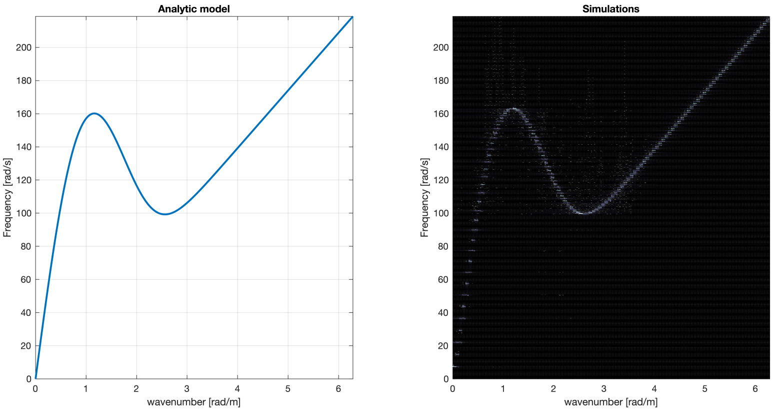

Figure 3.15. Dispersion analysis for Gauss-like interaction and strongly negative χ (Left: analytical dispersion relationship, Right: Simulated dispersion relationship)

Low magnitude χ

The simulation for low magnitude stiffness ratios has been carried on with $\chi = 0.9$, leading to $\mu = 1.82\text{x}10^5\ N/m^4$.

The map and the plots in Figure 3.16 show a barely non-dispersive behavior of the wave packet. In the plots are clearly recognizable the high wavenumbers backbones. According to the model, lower wavenumbers should propagate with slower speeds, and few wavenumbers should propagate with faster speeds. Such behavior is clearly visible in the simulations, where faster and slower frequencies spread from the central packet.

The comparison in Figure 3.17 corroborates the presence of dispersion also in the finite length waveguide. Slow wavenumbers propagate with slower speeds, speed that rapidly decreases and then lightly grows again, up to tend to the D'Alembert propagation speed, showing the migration phenomena hypothesized in the previous sections.

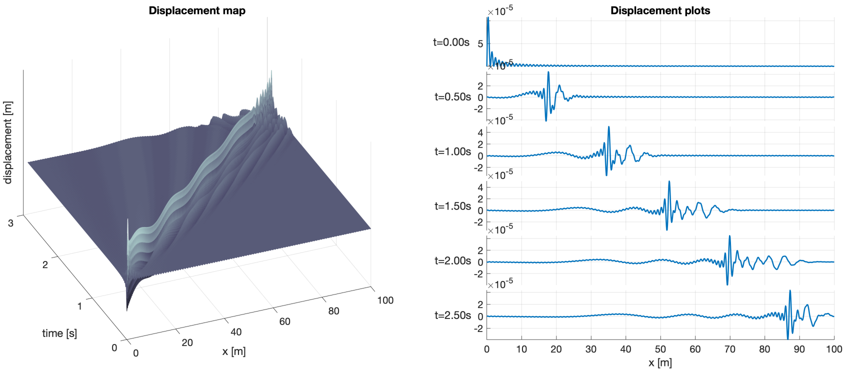

Figure 3.16. Displacement map (left) and plots (right) for 1D waveguide with low magnitude χ subject to Gauss-like interaction

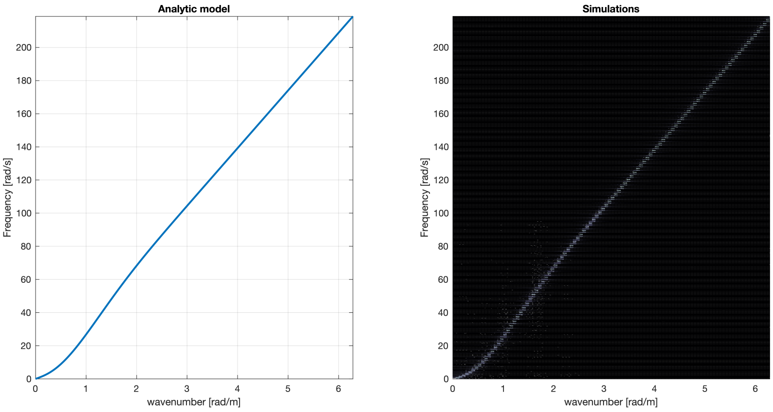

Figure 3.17. Dispersion analysis for Gauss-like interaction and low magnitude χ (Left: analytical dispersion relationship, Right: Simulated dispersion relationship)

Strongly positive χ

The value of the stiffness ratio chosen to simulate a strongly positive system is the same value in magnitude chosen for the negative case. The value has been chosen to compare the opposite effects borne with the same interaction magnitude but with opposite direction. In particular, $\chi = 42.7$ and $\mu = 8.64\text{x}10^6\ N/m^4$.
In the following simulation, the dispersion relationship leading to instability effects have not been excited, due to the focus of the work in the study of propagation phenomena.

The observation of the map and of the plots in Figure 3.18 shows the presence of a very fast wave package which travels along the whole waveguide quasi-instantaneously, as evident in the 3-D map (left). The D'Alembert backbone is evident, together with the presence of faster wave packets (not superluminal).

The comparison between the simulation and the analytical model corroborate the presence of the phenomena presented in the previous sections for strongly positive stiffness ratios.

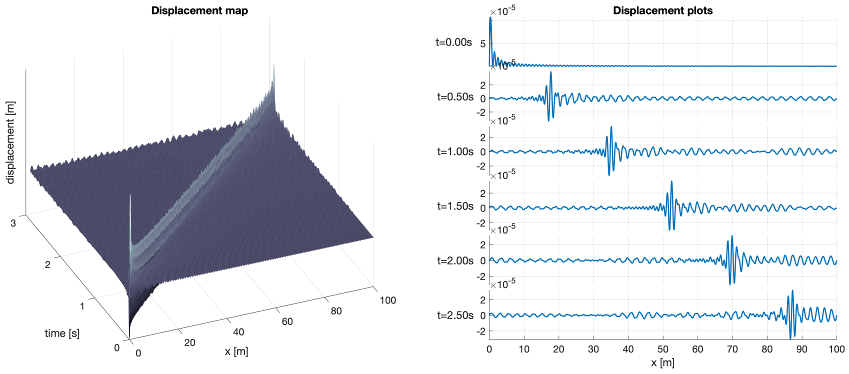

Figure 3.18. Displacement map (left) and plots (right) for 1D waveguide with strongly positive χ subject to Gauss-like interaction

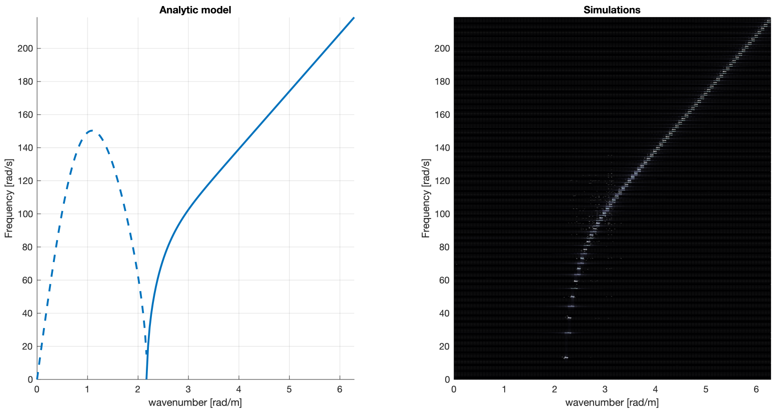

Figure 3.19. Dispersion analysis for Gauss-like interaction and strongly positive χ (Left: analytical dispersion relationship, Right: Simulated dispersion relationship)

In the next section a different interaction model is presented. This force leads to comparable effects, thanks to a comparable distance-decaying behavior.

3.2 Laplace-like

The Laplace-like model describes a distance-decaying long-range interaction between two particles in the media distant $\boldsymbol{r}$ the one from the other.

Similar to the Gauss-like interaction described in section 3.1.1, the Laplace-like interaction model is a combination of two factors: a distribution and a skew-symmetrical component. The mathematical expression of the former is defined as follows:

$$f(|\boldsymbol{r}|) = \mu e^{-\frac{|\boldsymbol{r}|}{\beta}} \tag{3.24}$$

The parameters μ ($\in \mathbb{R}$) and β ($\in \mathbb{R}^+$) inherit their physical meaning from the Gauss-like model. Figure 3.20 shows a picture with some Laplace-like examples.

With respect to the plot in Figure 3.1, the plots in Figure 3.20, obtained for the same μ,β couple, show that the general behavior is preserved. It is evident that the distance spread of the force is wider in the Laplace-like model, as a direct consequence of the Laplace distribution, while the peak position and magnitude are basically comparable, as shown in Figure 3.21:

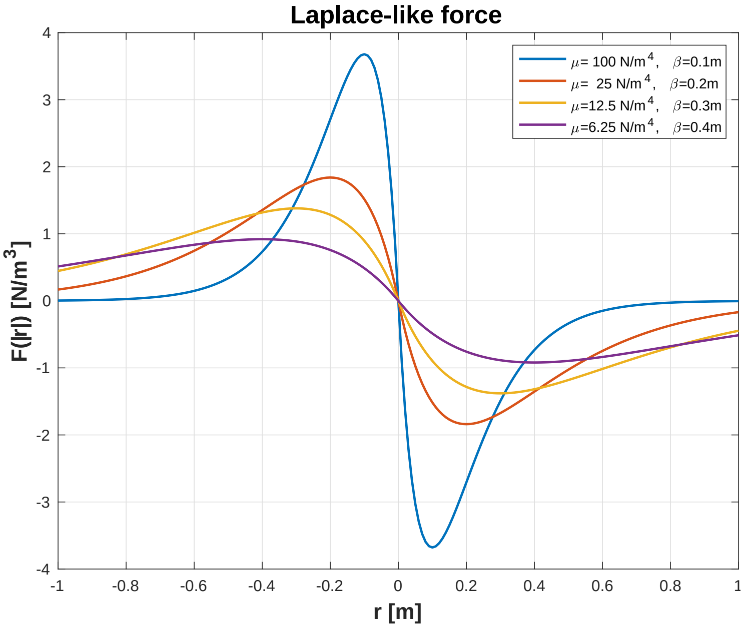

Figure 3.20. Laplace-like force as function of the distance vector $\boldsymbol{r} = \boldsymbol{x} - \boldsymbol{\xi}$

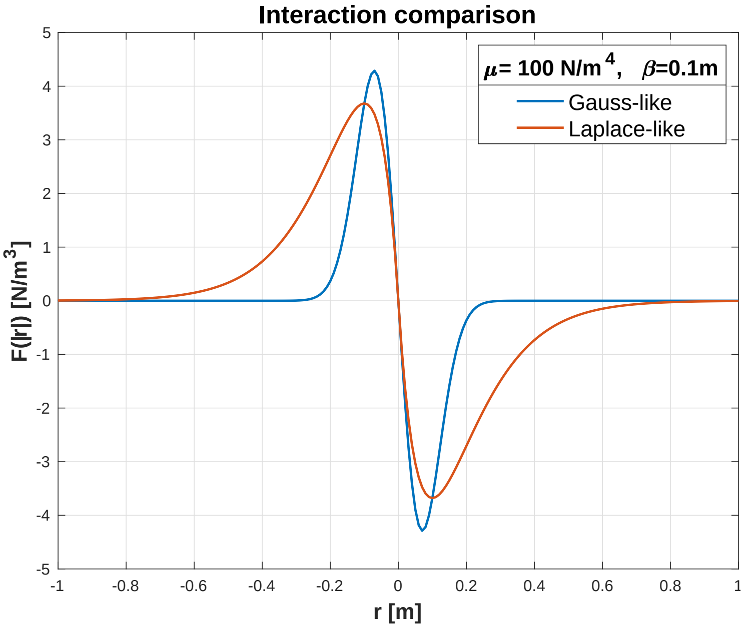

Figure 3.21. Comparison between Gauss-like and Laplace-like force for $\mu = 100\ N/m^4$ and $\beta = 0.1\ m$

As well as for the Gauss-like model, the Laplace like model can be used to mimic the trend of several power-like interactions, especially when the interaction has a lower decay, with respect to the distance.

3.2.1 Analytical Solution

The terms f_0 and g_0 have been calculated, and read as follows:

$$f_0(x-\xi) = \mu e^{-\frac{|x-\xi|}{\beta}} \tag{3.25a}$$

$$g_0(x-\xi) = -\frac{\mu}{\beta}|x-\xi| e^{-\frac{|x-\xi|}{\beta}} \tag{3.25b}$$

$$h_0(x-\xi) = f_0(x-\xi) + g_0(x-\xi) = \mu\left(1-\frac{|x-\xi|}{\beta}\right)e^{-\frac{|x-\xi|}{\beta}} \tag{3.25c}$$

Some terms in the equation of motion are null (as reference, see section 3.1.1). The equation of motion for the one-dimensional waveguide with Laplace-like interaction results as follows:

$$\rho\frac{\partial^2 w}{\partial t^2} - E\frac{\partial^2 w}{\partial x^2} - \left[\mu\left(1-\frac{|x|}{\beta}\right)e^{-\frac{|x|}{\beta}}\right] * w = 0 \tag{3.26}$$

Applying the Fourier transform in both space and time domain, factorizing the Fourier transform of the displacement assumed as in equation 3.2, the dispersion relationship is obtained:

$$\rho\omega^2 - Ek^2 + \mu\frac{2\sqrt{\frac{2}{\pi}}\beta^3}{\left(\beta^2k^2+1\right)^2}k^2 = 0 \tag{3.27}$$

According to the parameters in equation (3.12), the nondimensional dispersion relationship for the Laplace-like one-dimensional model is obtained as follows:

$$\Omega^2 + K^2\left(\frac{8\chi}{\sqrt{\pi}(K^2+1)^2} - 1\right) = 0 \tag{3.28}$$

The dispersion relationship with a Laplace-like interaction differs form the Gauss-like homologous equation in the nature of the long-range contribution. In fact, while in the Gauss-like dispersion relationship we note the presence of a transcendent wavenumber term that does not allow an analytical solution of the equation in the frequency domain, the Laplace-like model gives back a rational dispersion relationship that allows analytical solutions in the frequency domain, as in Appendix B.
The solution in the wavenumber domain has been evaluated for both dimensional and nondimensional quantities:

$$\omega = \pm k\sqrt{\frac{E}{\rho} - \frac{\mu}{\rho}\frac{2\sqrt{\frac{2}{\pi}}\beta^3}{\left(\beta^2k^2+1\right)^2}} = 0 \tag{3.29}$$

$$\Omega = \pm K\sqrt{1 - \frac{8\chi}{\sqrt{\pi}(K^2+1)^2}} = 0 \tag{3.30}$$

In the following paragraphs, the nondimensional dispersion relationship is analyzed.

Strongly negative χ

As well as for the Gauss-like model, the dispersion relationship for the Laplace-like interaction has been evaluated by varying the sign and the intensity of the stiffness ratio.

For strongly negative ratios, as shown in Figure 3.22, also the Laplace-like model shows a dispersion relationship bigger than the D'Alembert reference. Moreover, for $\chi <\sim -29$, the presence of wave-stopping and Negative Group Velocity regions emerge, as highlighted by the line and area, respectively.

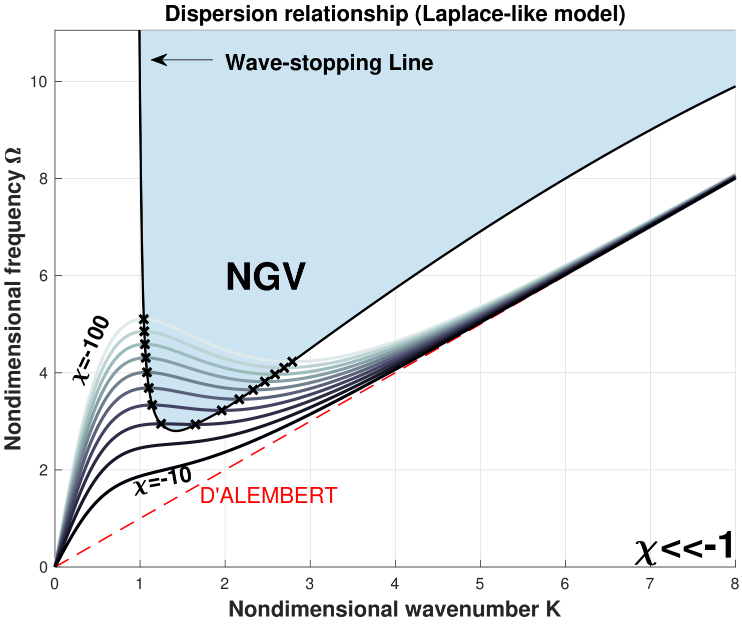

Figure 3.22. Dispersion curves for the 1D 2^{nd} order Laplace-like model with strongly negative χ

Low magnitude χ

The dispersion relationship shows, for long-range stiffnesses comparable with the short-range elasticity, pretty weakly curves, if compared with the local-elasticity reference, as shown in Figure 3.23.

Strongly positive χ

An unstable region is present also in the Laplace like model for $K \in [0, k_0]$, with $k_0 = \sqrt{\frac{2\sqrt{2}\sqrt{\chi}}{\sqrt[4]{\pi}} - 1}$, evaluated by zeroing the square root in equation (3.30) and taking the only solution compatible with the domain.

Out of the stability region, the frequency, always lower than the D'Alembert reference, asymptotically reaches a constant growing trend, corresponding to the D'Alembert one.

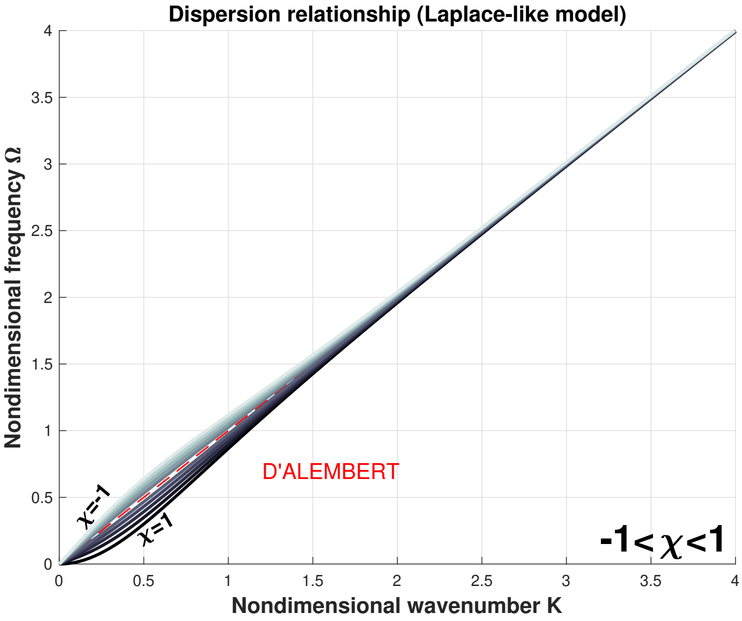

Figure 3.23. Dispersion curves for the 1D 2^{nd} order Laplace-like model with low magnitude χ

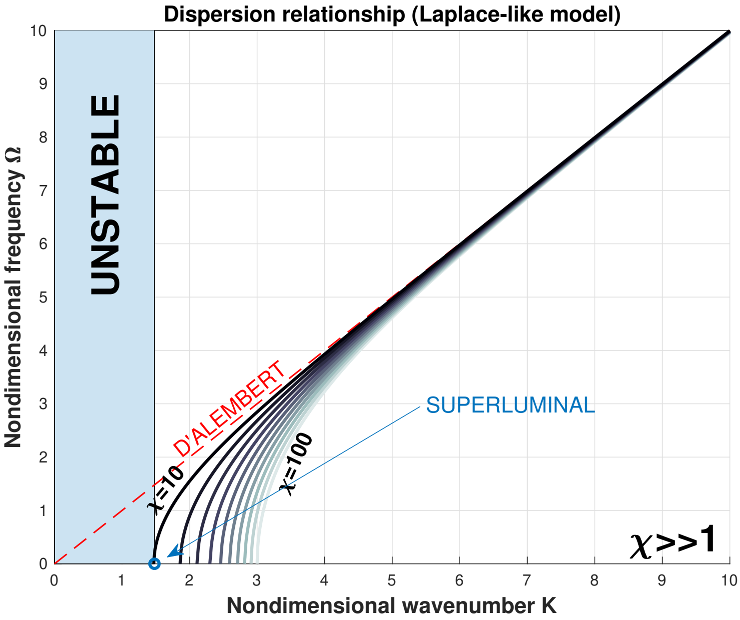

Figure 3.24. Dispersion curves for the 1D 2^{nd} order Laplace-like model with strongly positive χ

3.2.2 Wave speed analysis

Phase and group velocities are now evaluated. With a procedure similar to the Gauss-like model, the two quantities are calculated, in the following paragraphs.

Phase velocity

The nondimensional phase velocity in Laplace-like one-dimensional structures is evaluated, starting from the solution of the dimensional dispersion relationship: equation (3.29), obtaining its nondimensional counterpart:

$$\begin{aligned}
c_\phi = \frac{\omega}{k} &= \pm\sqrt{\frac{E}{\rho} - \frac{\mu}{\rho}\frac{2\sqrt{\frac{2}{\pi}}\beta^3}{\left(\beta^2 k^2 + 1\right)^2}} \\
&= \pm\sqrt{\frac{E}{\rho}}\sqrt{1 - \frac{\mu}{E}\frac{2\sqrt{\frac{2}{\pi}}\beta^3}{\left(\beta^2 k^2 + 1\right)^2}} \\
&= \pm c\sqrt{1 - \frac{\mu}{E}\frac{2\sqrt{\frac{2}{\pi}}\beta^3}{\left(\beta^2 k^2 + 1\right)^2}} \\
&= \pm c\sqrt{1 - \frac{8\chi}{\sqrt{\pi}\left(\beta^2 k^2 + 1\right)^2}} \\
&= \pm c\sqrt{1 - \frac{8\chi}{\sqrt{\pi}\left(K^2 + 1\right)^2}} \\
&= c\frac{\Omega}{K}
\end{aligned} \tag{3.31}$$

introducing $C_\phi = \frac{\Omega}{K}$ as the nondimensional phase velocity, from equation (3.31) we have:

$$C_\phi = \frac{\Omega}{K} = \pm\sqrt{1 - \frac{8\chi}{\sqrt{\pi}\left(K^2 + 1\right)^2}} \tag{3.32}$$

Group velocity

The group velocity is evaluated from the dimensional dispersion equation $\omega(k)$:

$$\begin{aligned}
c_g = \frac{\partial \omega}{\partial k} &= \pm\frac{\partial}{\partial k}\left[k\sqrt{\frac{E}{\rho}-\frac{\mu}{\rho}\frac{2\sqrt{\frac{2}{\pi}}\beta^3}{\left(\beta^2k^2+1\right)^2}}\right] \\
&= \pm\sqrt{\frac{E}{\rho}}\frac{\partial}{\partial k}\left[k\sqrt{1-\frac{\mu}{E}\frac{2\sqrt{\frac{2}{\pi}}\beta^3}{\left(\beta^2k^2+1\right)^2}}\right] \\
&= \pm c\frac{\partial}{\partial k}\left[k\sqrt{1-\frac{8\chi}{\sqrt{\pi}\left(\beta^2k^2+1\right)^2}}\right] \\
&= \pm c\frac{\partial}{\partial k}\left[\frac{\beta k\sqrt{1-\frac{8\chi}{\sqrt{\pi}\left(\beta^2k^2+1\right)^2}}}{\beta}\right] \\
&= \pm c\frac{\partial}{\partial(\beta k)}\left\{(\beta k)\sqrt{1-\frac{8\chi}{\sqrt{\pi}\left[(\beta k)^2+1\right]^2}}\right\} \\
&= \pm c\frac{\partial}{\partial K}\left[K\sqrt{1-\frac{8\chi}{\sqrt{\pi}\left(K^2+1\right)^2}}\right] \\
&= c\frac{\partial \Omega}{\partial K}
\end{aligned} \tag{3.33}$$

As in Section 3.1.1, $C_g = \frac{\partial \Omega}{\partial K}$ is the nondimensional group velocity. From equation (3.33):

$$C_g = \frac{\partial \Omega}{\partial K} = \frac{c_g}{c} = \pm\left[\sqrt{1-\frac{8\chi}{\pi\left(K^2+1\right)^2}}+\frac{16K^2\chi}{\pi\left(K^2+1\right)^3\sqrt{1-\frac{8\chi}{\pi\left(K^2+1\right)^2}}}\right] \tag{3.34}$$

The similarities with the Gauss-like model continue. In fact, the two model see the borne of the same phenomena, namely the presence of wave-stopping, of reverse propagation, of mode migration, and of superluminal, hypersonic group velocity, according to the magnitude and sign of the stiffness ratio χ.
In Figure 3.23 the phase and the group velocity for the three regions are depicted in a summarizing plot comprehensive of all the curves.

3.2.3 Simulations

The following section shows some numerical simulations obtained for the finite waveguide described in Section 3.1.3 with similar interaction magnitude and analogous spread.
The simulation for the strongly negative stiffness ratio is evaluated setting the value of the stiffness ratio (in this case $\chi = \pm 39.7$), obtaining next the value of the force magnitude $\mu = \pm 8.04\text{x}10^6\ N/m^4$ for the high magnitude stiffness ratios, and

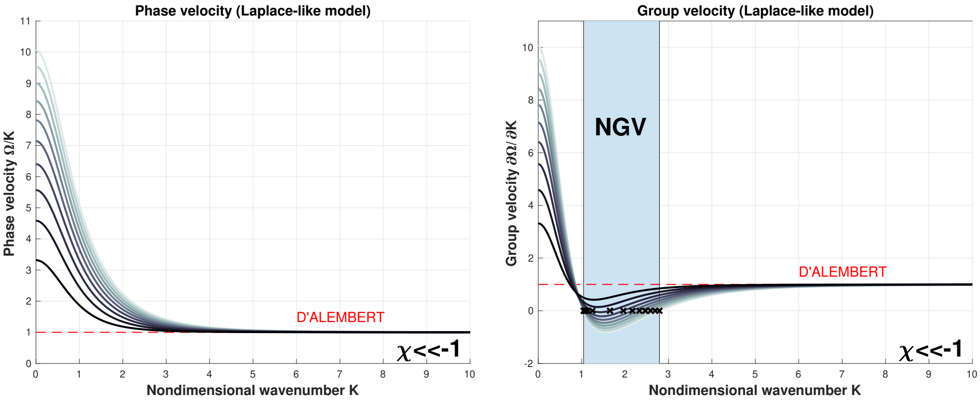

(a) Phase velocity, $\chi \ll -1$. **(b)** Group velocity, $\chi \ll -1$.

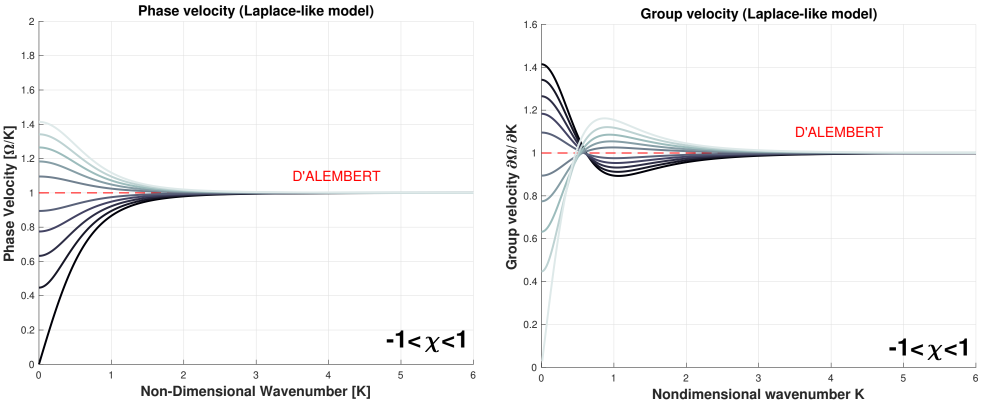

(c) Phase velocity, $-1 \leq \chi \leq 1$. **(d)** Group velocity, $-1 \leq \chi \leq 1$.

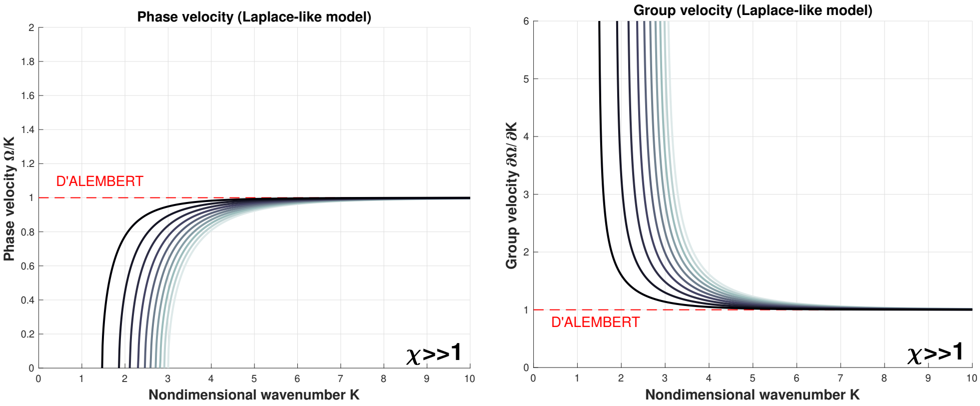

(e) Phase velocity, $\chi \gg 1$. **(f)** Group velocity, $\chi \gg 1$.

Figure 3.23. Propagation speeds for the Laplace-like model.

$\chi = -0.9$ with $\mu = -1.82\text{x}10^5\ N/m^4$. The simulations are presented in Figure 3.22.

A qualitative analysis of the simulations shows the presence of the expected propagation phenomena, coherently with the simulations with Gauss-like interaction

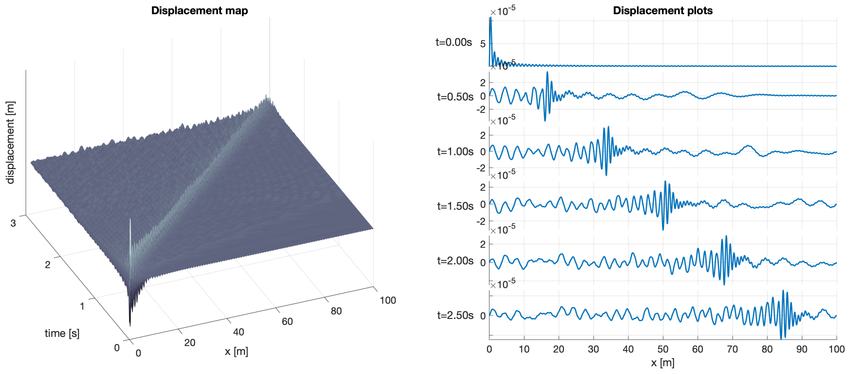

(a) Strongly negative χ

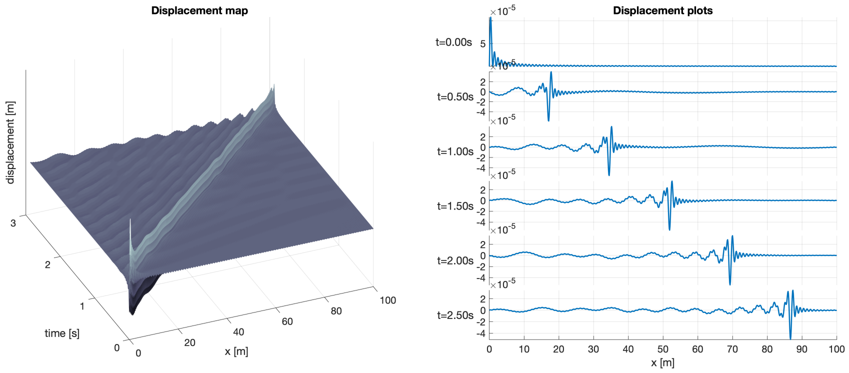

(b) Low magnitude χ

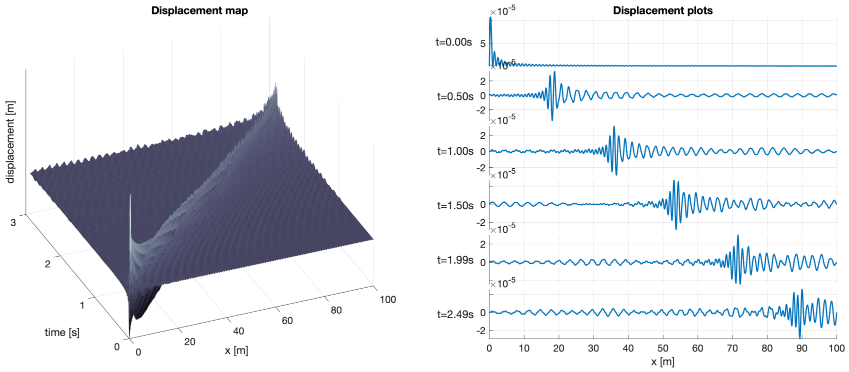

(c) Strongly positive χ

Figure 3.22. Displacement maps (left) and plots (right) for 1D waveguide subject to Laplace-like interaction

described in Section 3.1.3. The analysis of the propagation behavior, presented in Figure 3.21 shows that the trend of the dispersion curves is respected, but, no quantitative match is registered.

A gap is evident in the values where the strange propagation phenomena have

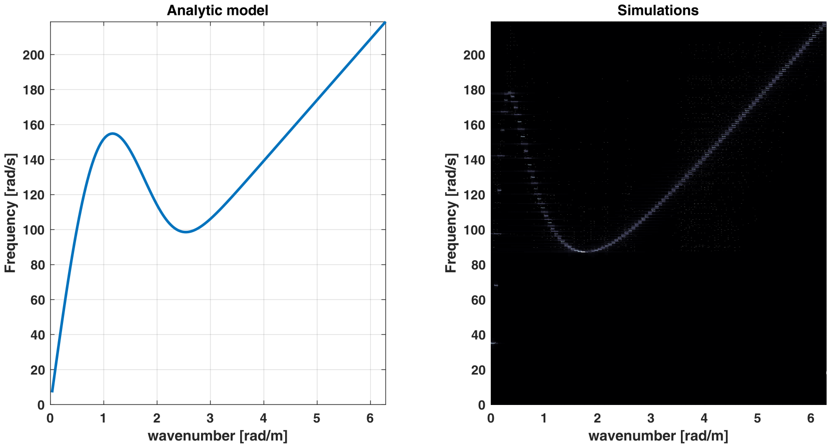

(a) Strongly negative χ

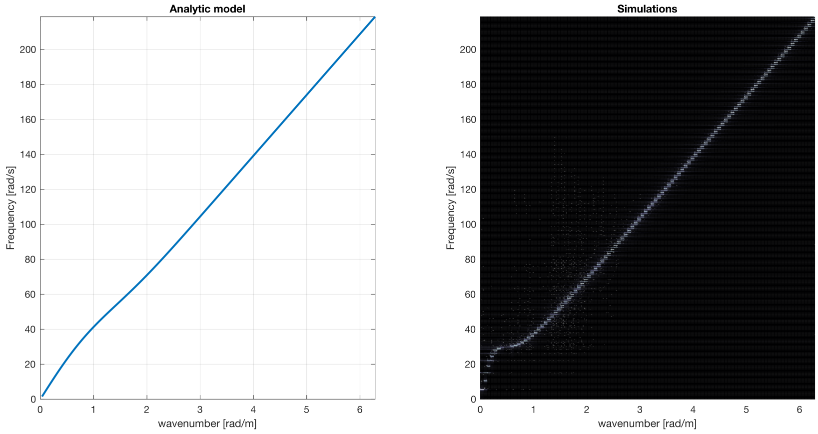

(b) Low magnitude χ

been analytically highlighted. This discrepancy has an explanation in the nature of the force, compared to the interaction length.

The Laplace-like force, as depicted in Figure 3.21, shows that for the same interaction length parameter β, the actual spread is different for the two models. The Laplace distribution, in fact, vanishes more slowly if compared to the normal distribution (Gauss distribution). The truncation effects due to the limited waveguide appear to be no more negligible with respect to the Gauss-like interaction with the same interaction length.

The long-range effect borne from the simulations appears amplified with respect to the analytical results. Under a possible follow up in the analysis, an evaluation of the gap related to the infinite to finite truncation can be carried with both analytical and computational approaches, in a physical feasibility perspective.

The two models show practically the same phenomena, the main difference being in the possibility to solve in closed form (see B) the dispersion relationship of the Laplace-like model in the wavenumber domain.

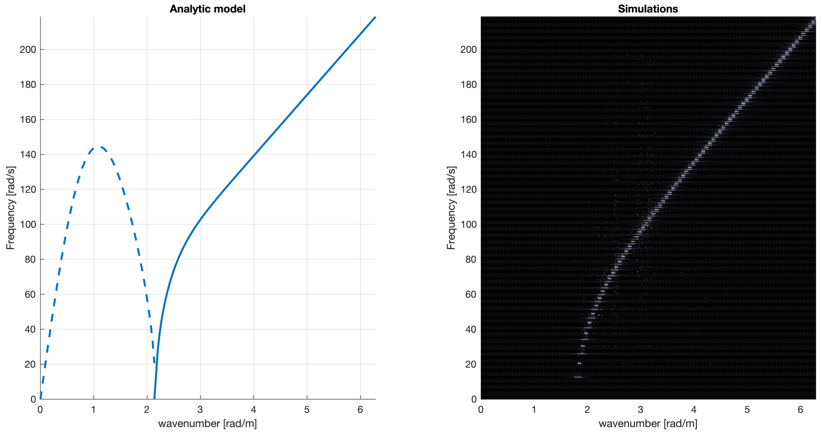

(c) Strongly positive χ

Figure 3.21. Dispersion analysis for Laplace-like interaction (Left: analytical dispersion relationship, Right: Simulated dispersion relationship)

In general, if the interaction force responds to a skew-symmetric behavior $\boldsymbol{F}(\boldsymbol{r}(\boldsymbol{x},\boldsymbol{\xi})) = -\boldsymbol{F}(-\boldsymbol{r}(\boldsymbol{x},\boldsymbol{\xi}))$ responsible of preserving the action-reaction principle, equation (3.1) can be rewritten in the following compact form:

$$\rho\ddot{w} - Ew'' + h * w = 0 \tag{3.35}$$

with $\ddot{w} = \dfrac{\partial^2 w}{\partial t^2}$, $w'' = \dfrac{\partial^2 w}{\partial x^2}$, and $h = f_0 + g_0$.
In the previous sections, the propagation behavior has been analyzed, by selecting some discrete values of the stiffness ratio. To better understand the strange phenomena emerged in these interaction models, a propagation map is built, as in Figure 3.22.

All the unusual regions have been highlighted in Figure 3.22. In both maps, the

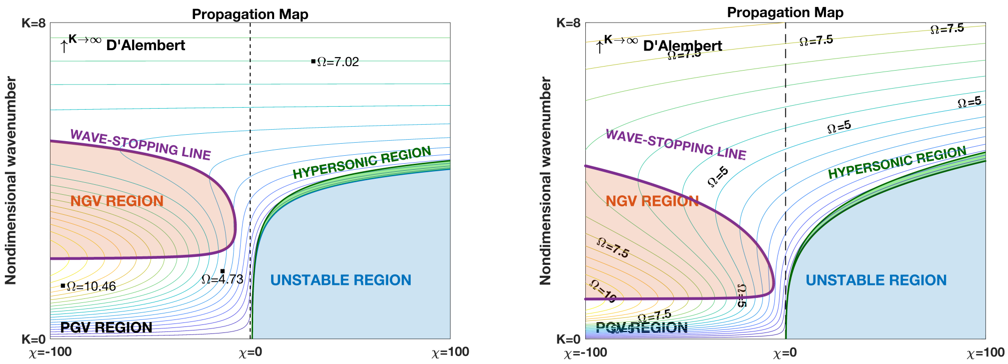

(a) Gauss-like interaction **(b)** Laplace-like interaction

Figure 3.22. Dispersion maps, Gauss-like and Laplace-like interaction.

Wave-Stopping line, the Negative Group Velocity, Unstable and Hypersonic regions

emerge. The map depict the nondimensional frequency (surfaces) as function of the stiffness ratio (in abscissa) and of the nondimensional wavenumber (in ordinate).
The next model has a different basis. in fact, the force is a nonlocal elastic interaction, spreading up to a finite distance for each element of the waveguide.

3.3 Rectangular

The Gauss-like and Laplace-like models have been developed starting from the assumption of an interaction force split in two terms, an intensity term, function of the norm of the distance vector, and the distance vector itself. The rectangular model, instead, describes a classical elastic connection spreading in a finite rectangular window.
To this purpose, the assumptions made to obtain equation (2.15) are not valid, and the equation of motion for the rectangular model is the one-dimensional version of equation (2.3), as follows:

$$\rho\frac{\partial^2 w}{\partial t^2} - E\frac{\partial^2 w}{\partial x^2} + \mu\int_{-\infty}^{+\infty} H(x-\xi,\beta)\varepsilon\, d\xi = 0 \tag{3.36}$$

where the term $\mu\int_{-\infty}^{+\infty} H(x-\xi,\beta)\varepsilon\, d\xi$ describes the rectangular the long-range interaction. Moreover $H(x-\xi,\beta)$ is the function that limits the interaction in a rectangular 2β wide window, as follows:

$$H(x-\xi,\beta) = \Theta(x-\xi+\beta) - \Theta(x-\xi-\beta) \tag{3.37}$$

with Θ the Heaviside theta function.

3.3.1 Analytical Solution

The integral term of equation (3.36) is analyzed:

$$\int_{-\infty}^{+\infty} H(x-\xi,\beta)\varepsilon\, d\xi = \int_{-\infty}^{+\infty} \left[\Theta(x-\xi+\beta) - \Theta(x-\xi-\beta)\right]\left[w(x) - w(\xi)\right] d\xi \tag{3.38}$$

that can be split into the summation of two integrals:

$$\int_{-\infty}^{+\infty} \left[\Theta(x-\xi+\beta) - \Theta(x-\xi-\beta)\right] w(x)\, d\xi \tag{3.39a}$$

and

$$-\int_{-\infty}^{+\infty} \left[\Theta(x-\xi+\beta) - \Theta(x-\xi-\beta)\right] w(\xi)\, d\xi \tag{3.39b}$$

Analyzing equation (3.39a) it becomes:

$$\begin{aligned}\int_{-\infty}^{+\infty} \left[\Theta(x-\xi+\beta) - \Theta(x-\xi-\beta)\right] w(x)\, d\xi &= w(x)\int_{-\infty}^{+\infty} \left[\Theta(x-\xi+\beta) - \Theta(x-\xi-\beta)\right] d\xi \\ &= \left[(x-\xi+\beta)\Theta(x-\xi+\beta) - (x-\xi-\beta)\Theta(x-\xi-\beta)\right]_{-\infty}^{+\infty} w(x) \\ &= 2\beta w(x)\end{aligned} \tag{3.40}$$

while equation (3.39b) becomes:

$$
\begin{aligned}
&-\int_{-\infty}^{+\infty}\left[\Theta(x-\xi+\beta)-\Theta(x-\xi-\beta)\right]w(\xi)\,d\xi \\
&\qquad=-\int_{-\infty}^{+\infty}\left[\Theta(x+\beta-\xi)-\Theta(x-\beta-\xi)\right]w(\xi)\,d\xi \\
&\qquad=-\left[\Theta(x+\beta)-\Theta(x-\beta)\right]*w(x)
\end{aligned}
\tag{3.41}
$$

Substituting equations (3.40) and (3.41) into equation (3.36) the equation of motion for the rectangular interaction is obtained:

$$
\rho\frac{\partial^2 w}{\partial t^2}-E\frac{\partial^2 w}{\partial x^2}+2\beta\mu w(x)-\mu\left[\Theta(x+\beta)-\Theta(x-\beta)\right]*w(x)=0 \tag{3.42}
$$

Applying the Fourier Transform in time and space domains the equation of motion reads as follows:

$$
-\rho\omega^2 W+Ek^2W+2\beta\mu W-\mu\sqrt{\frac{2}{\pi}}\frac{\sin(\beta k)}{k}W=0 \tag{3.43}
$$

Collecting $W(k,\omega)$ the dispersion relationship is obtained:

$$
-\rho\omega^2+Ek^2+2\beta\mu-\mu\sqrt{\frac{2}{\pi}}\frac{\sin(\beta k)}{k}=0 \tag{3.44}
$$

that, in nondimensional parameters, becomes:

$$
-\Omega^2+K^2+4\sqrt{2}\chi-\chi\frac{8}{\sqrt{\pi}}\operatorname{sinc}K=0 \tag{3.45}
$$

and, solved in the wavenumbers domain:

$$
\omega=\pm\sqrt{\frac{E}{\rho}k^2+2\beta\frac{\mu}{\rho}-\frac{\mu}{\rho}\sqrt{\frac{2}{\pi}}\frac{\sin(\beta k)}{k}} \tag{3.46a}
$$

$$
\Omega=\pm\sqrt{K^2+4\sqrt{2}\chi-\chi\frac{8}{\sqrt{\pi}}\operatorname{sinc}K} \tag{3.46b}
$$

The model stands only for positive values of the stiffness ratio χ. In this model, in fact, μ is the spring stiffness distribution per unit length, generally positive.

An interesting difference emerge, with respect to the dispersion relationships obtained with the Gauss-like and Laplace like models. The presence of a constant term strongly modifies the propagation behavior, as depicted in Figure 3.23.

The dispersion relationships depicted in Figure 3.23 shows that, in general, the propagation regime is different from the short-range case, the red dashed line, moreover, increasing the intensity of the stiffness ratio, the presence of wave-stopping and reverse propagation emerge, coherently, in this case, with the two interaction models presented in the previous sections, but, thanks to the presence of an harmonic element, for $\chi > 50$, more NGV bandwidths are present.

In Figure 3.24 the propagation map of the rectangular model where the Wave-stopping, the NGV regions and the superluminal phase velocity regions are highlighted.

The wave propagation analysis continues with the evaluation of the wave speeds.

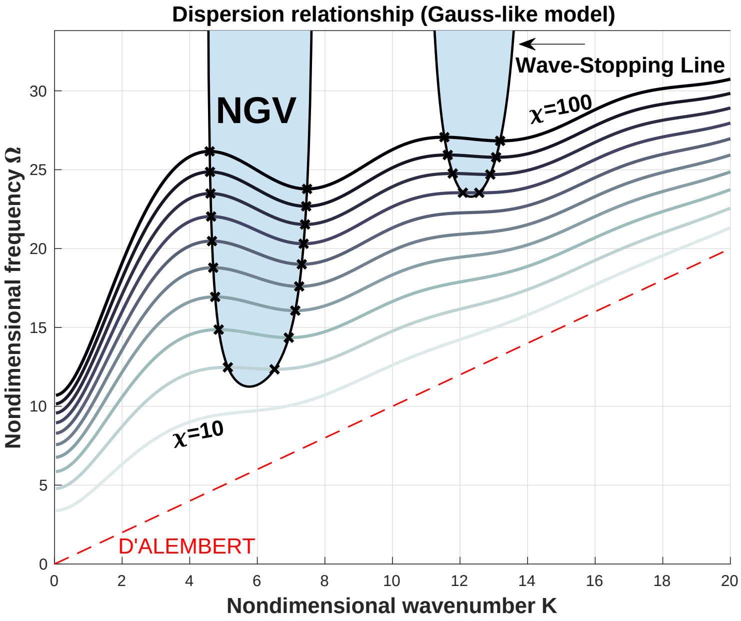

Figure 3.23. Dispersion curves for the 1D 2^{nd} order rectangular model

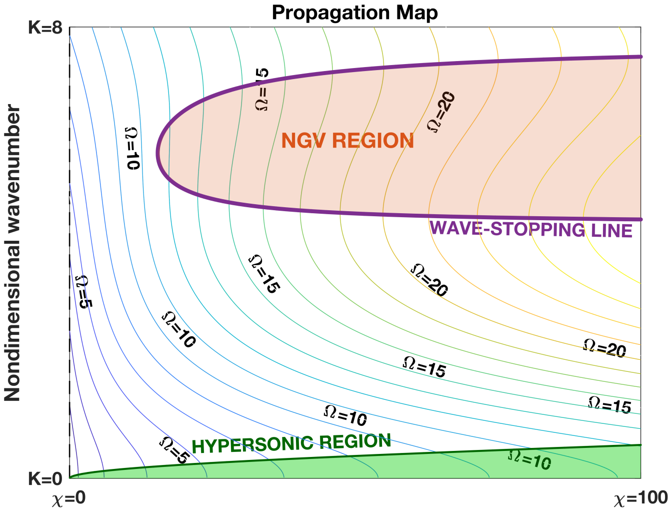

Figure 3.24. Dispersion map rectangular interaction.

3.3.2 Wave speed analysis

The analysis is divided in the evaluation of the phase velocity and the group velocity.

Phase velocity

The nondimensional phase velocity for rectangular interaction is evaluated, starting from the solution of the dimensional dispersion relationship, in equation (3.46a), to obtain, consequently, its nondimensional counterpart:

$$\begin{aligned}
c_\phi &= \frac{\omega}{k} = \pm\frac{\sqrt{\frac{E}{\rho}k^2 + 2\beta\frac{\mu}{\rho} - \frac{\mu}{\rho}\sqrt{\frac{2}{\pi}}\frac{\sin(\beta k)}{k}}}{k} \\
c_\phi &= \frac{\omega}{k} = \pm\sqrt{\frac{E}{\rho} + 2\beta\frac{\mu}{\rho k^2} - \frac{\mu}{\rho}\sqrt{\frac{2}{\pi}}\frac{\sin(\beta k)}{k^3}} \\
&= \pm\sqrt{\frac{E}{\rho}}\sqrt{1 + 2\beta\frac{\mu}{Ek^2} - \frac{\mu}{E}\sqrt{\frac{2}{\pi}}\frac{\sin(\beta k)}{k^3}} \\
&= \pm c\sqrt{1 + 2\beta\frac{\mu}{Ek^2} - \frac{\mu}{E}\sqrt{\frac{2}{\pi}}\frac{\sin(\beta k)}{k^3}} \\
&= \pm c\sqrt{1 + 2\beta^3\frac{\mu}{E(\beta k)^2} - \frac{\mu\beta^3}{E}\sqrt{\frac{2}{\pi}}\frac{\sin(\beta k)}{(\beta k)^3}} \qquad (3.47) \\
&= \pm c\sqrt{1 + 2\beta^3\frac{\mu}{E(\beta k)^2} - \frac{\mu\beta^3}{E}\sqrt{\frac{2}{\pi}}\frac{\operatorname{sinc}(\beta k)}{(\beta k)^2}} \\
&= \pm c\sqrt{1 + \frac{4\sqrt{2}\chi}{K^2} - \chi\frac{8}{\sqrt{\pi}}\frac{\operatorname{sinc} K}{K^2}} \\
&= \pm c\frac{\sqrt{K^2 + 4\sqrt{2}\chi - \chi\frac{8}{\sqrt{\pi}}\operatorname{sinc} K}}{K} \\
&= c\frac{\Omega}{K}
\end{aligned}$$

introducing $C_\phi = \frac{\Omega}{K}$ as the nondimensional phase velocity, from equation (3.47):

$$C_\phi = \frac{\Omega}{K} = \pm\sqrt{1 + \frac{4\sqrt{2}\chi}{K^2} - \chi\frac{8}{\sqrt{\pi}}\frac{\operatorname{sinc} K}{K^2}} \qquad (3.48)$$

In Figure 3.25 some plots of the phase velocity are presented:

The phase velocity in one-dimensional rods with rectangular interaction shows a decreasing behavior, that asymptotically tends to the short range waveguide, but, with respect to the Gauss-like and Laplace-like models with strongly negative stiffness ratios, at very low wavenumbers, the phase velocity tends to infinite values, showing the presence of superluminal phase velocity regions.

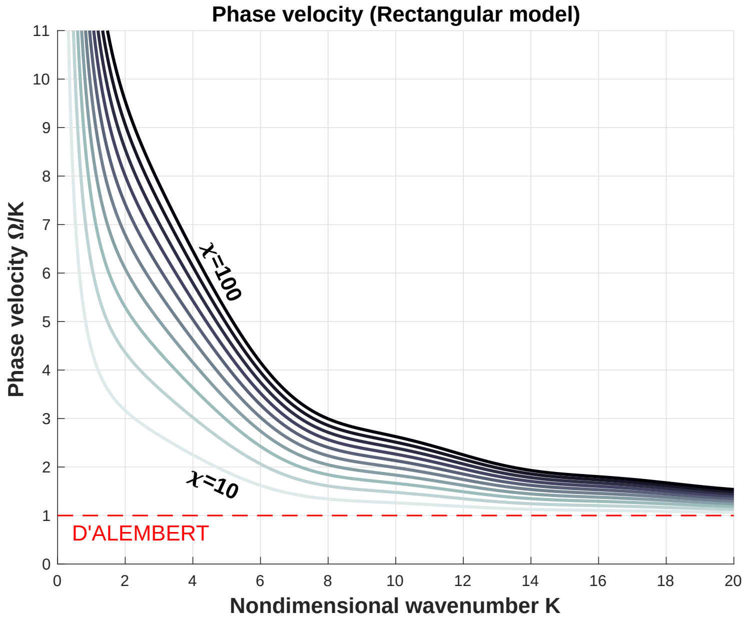

Figure 3.25. Dispersion curves for the 1D 2^{nd} order rectangular model

Group velocity

The group velocity is evaluated from the dimensional dispersion equation $\omega(k)$:

$$\begin{aligned}
c_g = \frac{\partial \omega}{\partial k} &= \pm\frac{\partial}{\partial k}\left[\sqrt{\frac{E}{\rho}k^2 + 2\beta\frac{\mu}{\rho} - \frac{\mu}{\rho}\sqrt{\frac{2}{\pi}}\frac{\sin(\beta k)}{k}}\right] \\
&= \pm\sqrt{\frac{E}{\rho}}\frac{\partial}{\partial k}\left[\sqrt{k^2 + 2\beta\frac{\mu}{E} - \frac{\mu}{E}\sqrt{\frac{2}{\pi}}\frac{\sin(\beta k)}{k}}\right] \\
&= \pm c\frac{\partial}{\partial k}\left[\sqrt{k^2 + 2\beta\frac{\mu}{E} - \frac{\mu}{E}\sqrt{\frac{2}{\pi}}\frac{\sin(\beta k)}{k}}\right] \\
&= \pm c\frac{\partial}{\partial k}\left[\frac{\sqrt{(\beta k)^2 + 2\beta^3\frac{\mu}{E} - \frac{\mu\beta^3}{E}\sqrt{\frac{2}{\pi}}\frac{\sin(\beta k)}{\beta k}}}{\beta}\right] \\
&= \pm c\frac{\partial}{\partial(\beta k)}\left[\sqrt{(\beta k)^2 + 2\beta^3\frac{\mu}{E} - \frac{\mu\beta^3}{E}\sqrt{\frac{2}{\pi}}\operatorname{sinc}(\beta k)}\right] \\
&= \pm c\frac{\partial}{\partial K}\left[\sqrt{K^2 + 4\sqrt{2}\chi - \chi\frac{8}{\sqrt{\pi}}\operatorname{sinc} K}\right] \\
&= c\frac{\partial \Omega}{\partial K}
\end{aligned} \tag{3.49}$$

As in Section 3.1.2, $C_g = \frac{\partial\Omega}{\partial K}$ is the nondimensional group velocity. From equation (3.49):

$$C_g = \frac{\partial\Omega}{\partial K} = \frac{c_g}{c} = \pm\left[\frac{\chi\frac{8}{\sqrt{\pi}}\frac{\operatorname{sinc}K}{K} - \chi\frac{8}{\sqrt{\pi}}\frac{\cos K}{K} + 2K}{2\sqrt{K^2 + 4\sqrt{2}\chi - \chi\frac{8}{\sqrt{\pi}}\operatorname{sinc}K}}\right] \tag{3.50}$$

In Figure 3.26 some plots of the group velocity are presented: The group velocity for the rectangular model is depicted in Figure 3.26, for some values of the stiffness ratio. The behavior can be defined as pseudo-harmonic and several zero crossing appear, the number of which is related to the intensity of χ, leading to the presence of one or more NGV regions, delimited by couples of wave-stopping wavenumbers. One other interesting phenomenon is evidenced in terms of wave-stopping: for very low wavenumbers, the group velocity vanishes, and, this effect appears for every not null stiffness ratio, leading to the presence of wave stopping also where the long-range interaction is not so strong, requirement necessary in the Gauss-like and Laplace-like cases.

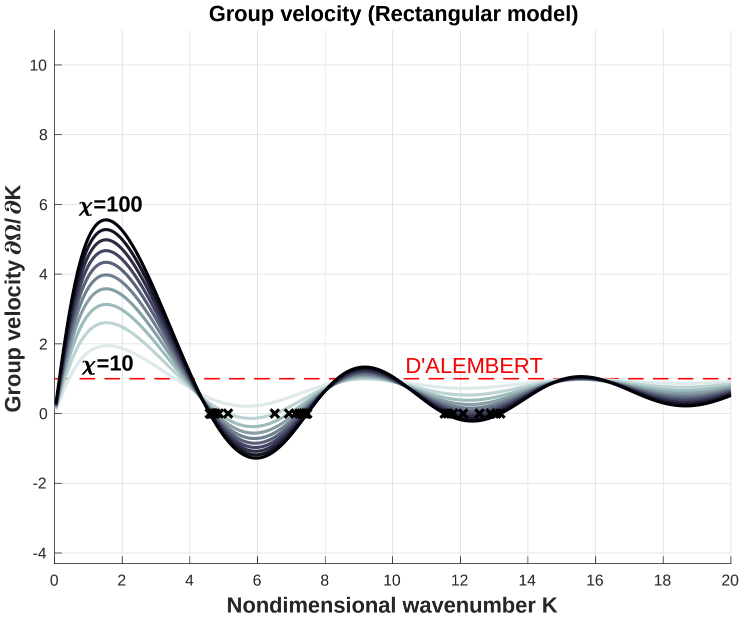

Figure 3.26. Dispersion curves for the 1D 2^{nd} order rectangular model

For high wavenumbers, the harmonic amplitude vanishes and the group velocity, as shown in the previous interaction models. The waveguide, thus, tends to the short-range D'Alembert waveguide.

Chapter 4

Long-range interactions in a Bernoulli beam

The beam model is typical of elastic media subject to bending waves. In the following section, a beam-like long-range structure, thereafter called waveguide, subject to bending waves, is presented.

The local elasticity operator responds to the Euler[11]-Bernoulli[12][28, 70] beam model, represented as follows:

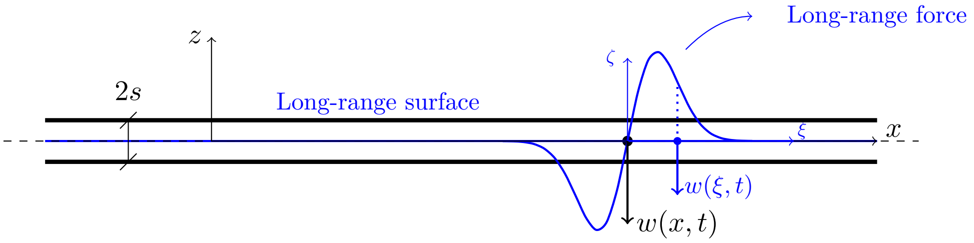

Figure 4.1. Unbounded Euler-Bernoulli beam with long-range interaction.

with ρ, $2s$, A, E and I the mass density, the thickness, the cross-section (supposed rectangular), the Young modulus and the moment of inertia, respectively, constant along the beam, and $w(\dots)$ the z-axis displacement.

The two dimensional model, according to the Euler-Bernoulli formulation, is reduced to a one-dimensional problem, function of the only $z-$direction displacement, and the local elasticity operator is $EI\dfrac{\partial^4 w}{\partial x^4}$. The equation of motion for the Euler-Bernoulli formulation reads as follows:

$$\rho A\frac{\partial^2 w(x,t)}{\partial t^2}+EI\frac{\partial^4 w(x,t)}{\partial x^4}+p(x,t)=0 \tag{4.1}$$

where $p(x,t)$ indicates the applied loads.

For a purely flexural beam, the long-range interaction leads to two terms: $q(x,t)$

---

[11] Leonhard Euler (April 5th, 1707 - September 18th 1783) Swiss mathematician, physicist, astronomer, logician and engineer

[12] Daniel Bernoulli (February 8th, 1700 - March 17th, 1782) Swiss mathematician and physicist

and $m(x,t)$, a shear force and a bending moment, respectively.
The resulting equation of motion of the Euler-Bernoulli beam is:

$$\rho A \frac{\partial^2 w(x,t)}{\partial t^2} + EI \frac{\partial^4 w(x,t)}{\partial x^4} + q(x) + \frac{\partial m(x)}{\partial x} = 0 \tag{4.2}$$

where

$$m(x) = zF_x(x) = z \int_{-\infty}^{\infty} \left[\boldsymbol{r} f(|\boldsymbol{r}|) \right]_x d\xi \tag{4.3a}$$

$$q(x) = F_z(x) = \int_{-\infty}^{\infty} \left[(\boldsymbol{r} f(|\boldsymbol{r}|) \right]_z d\xi \tag{4.3b}$$

Two interactions are considered, the first where the long-range interaction is present on the upper surface only (TOP), the second where both the upper and the lower surfaces interact (TOP-BOTTOM).

4.1 Gauss-like

The case of a Gauss-like interaction in long-range beams is considered. In the following parts, the interaction on the only top surface is considered, as graphically depicted in Figure 4.2 that follows:

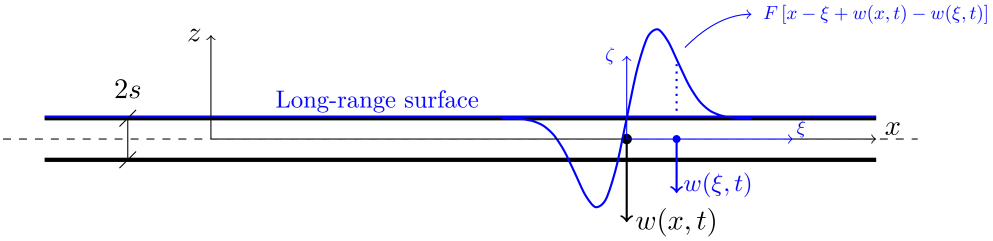

Figure 4.2. Unbounded Euler-Bernoulli beam with TOP long-range interaction (Gauss-like).

Subsequently, the long-range interaction is introduced also in the bottom surface. As a consequence, a mutual interaction between particles from top to bottom and vice-versa appears, besides the self-evident interaction between all the elements of the bottom surfaces. The graphical appearance of such beam is shown in Figure 4.3.

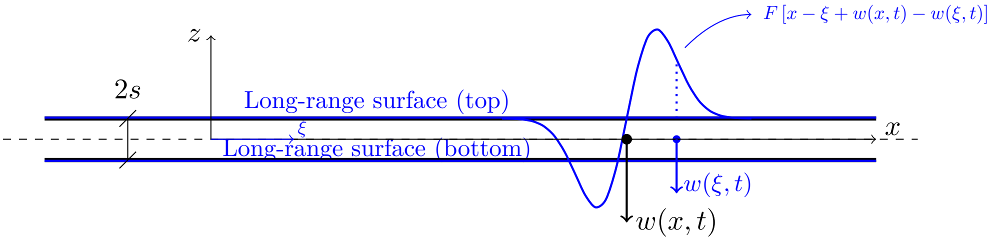

Figure 4.3. Unbounded Euler-Bernoulli beam with TOP-BOTTOM long-range interaction (Gauss-like).

4.1.1 Top surface interaction

Analytical solution

According to the Euler-Bernoulli beam model, $w(\dots)$ is sufficient to describe the displacement of the beam: $\boldsymbol{u}$. Being:

$$u_x = -s(w'(x,t) - w'(\xi,t)) \tag{4.4a}$$

$$u_z = w(x,t) - w(\xi,t) \tag{4.4b}$$

with $w'(\dots) = \frac{\partial w(\dots)}{\partial x}$ and, remembering that $\boldsymbol{x} = \left(\begin{smallmatrix} x \\ s \end{smallmatrix}\right)$ and $\boldsymbol{\xi} = \left(\begin{smallmatrix} \xi \\ s \end{smallmatrix}\right)$, with $\boldsymbol{g}_0 = \begin{bmatrix} \left.\frac{\partial f(|\boldsymbol{r}|)}{\partial |\boldsymbol{r}|}\right|_0 \frac{(x-\xi)^2}{|x-\xi|} & 0 \\ 0 & 0 \end{bmatrix} = \begin{bmatrix} g_{0_{11}} & 0 \\ 0 & 0 \end{bmatrix}$, the long-range force becomes:

$$\boldsymbol{r} f(|\boldsymbol{r}|) = f_0 \left(\begin{smallmatrix} x-\xi \\ 0 \end{smallmatrix}\right) + \begin{bmatrix} g_{0_{11}} & 0 \\ 0 & 0 \end{bmatrix} \left(\begin{smallmatrix} -s[w'(x,t)-w'(\xi,t)] \\ w(x,t)-w(\xi,t) \end{smallmatrix}\right) + f_0 \left(\begin{smallmatrix} -s[w'(x,t)-w'(\xi,t)] \\ w(x,t)-w(\xi,t) \end{smallmatrix}\right) \tag{4.5}$$

Bending moment From equation (4.3a)

$$\begin{aligned} m(\boldsymbol{x},t) &= s \int_{-\infty}^{\infty} f_0(x-\xi) + (g_{0_{11}} + f_0)\left\{-s[w'(x,t) - w'(\xi,t)]\right\} d\xi && (4.6a) \\ &= s \int_{-\infty}^{\infty} f_0(x-\xi) d\xi - \\ &- s^2 w'(x,t) \int_{-\infty}^{\infty} (g_{0_{11}} + f_0) d\xi + \\ &+ s^2 \int_{-\infty}^{\infty} (g_{0_{11}} + f_0) w'(\xi,t) = && (4.6b) \\ &= s^2 \int_{-\infty}^{\infty} (g_{0_{11}} + f_0) w'(\xi,t) = && (4.6c) \\ &= s^2 \left[(g_{0_{11}} + f_0) * w'(x,t)\right] && (4.6d) \end{aligned}$$

Shear force From equation (4.3b)

$$\begin{aligned} p(\boldsymbol{x},t) &= \int_{-\infty}^{\infty} f_0[w(x,t) - w(\xi,t)] d\xi && (4.7a) \\ &= w(x) \int_{-\infty}^{\infty} f_0 d\xi - \int_{-\infty}^{\infty} f_0 w(\xi) = && (4.7b) \\ &= \bar{f}_0 w(x) - f_0 * w(x) && (4.7c) \end{aligned}$$

where $\bar{\square} = \square * 1$.

Substituting (4.6) and (4.7) into (4.2):

$$\rho A \frac{\partial^2 w(x,t)}{\partial t^2} + EI \frac{\partial^4 w(x,t)}{\partial x^4} + \bar{f}_0 w(x,t) - (f_0 * w(x,t)) + \frac{\partial}{\partial x}\left\{s^2 \left[(f_0 + g_{0_{11}}) * \frac{\partial w(x,t)}{\partial x}\right]\right\} = 0 \tag{4.8}$$

The Fourier Transform in time and space leads to the dispersion relationship:

$$-\rho A\omega^2 + EIk^4 + \bar{f}_0 - \hat{\hat{f}}_0 - k^2 s^2 \left(\hat{\hat{f}}_0 + \hat{\hat{g}}_{0_{11}}\right) = 0 \tag{4.9}$$

where $\hat{\hat{\square}}$ denotes the double Fourier transform.
For a Gauss-like interaction, remembering that $f(|\boldsymbol{r}|) = \mu A e^{-\frac{|\boldsymbol{r}|^2}{\beta^2}}$, and remembering f_0 and $g_{0_{11}} = g_0$ from equation (3.5), equation (4.9) becomes

$$-\rho A\omega^2 + EIk^4 + \mu A\beta\sqrt{\pi} - \mu A\beta\frac{e^{-\frac{(\beta k)^2}{4}}}{\sqrt{2}} - k^4 s^2 \mu A\beta^3 \frac{e^{-\frac{(k\beta)^2}{4}}}{2\sqrt{2}} = 0 \tag{4.10}$$

that, in nondimensional parameters becomes:

$$\Omega^2 - \frac{1}{3}S^2K^4 - \chi\left[2\sqrt{2\pi} - \left(2 + S^2K^4\right)e^{-\frac{K^2}{4}}\right] = 0 \tag{4.11}$$

with $S = \frac{s}{\beta}$, and the moment of inertia is $I = \dfrac{1}{12}A(2s)^2 = \dfrac{1}{3}As^2$.
Equation 4.12 leads to the nondimensional dispersion curve:

$$\Omega = \pm\sqrt{\frac{1}{3}S^2K^4 + \chi\left[2\sqrt{2\pi} - (2 + S^2K^4)\,e^{-\frac{K^2}{4}}\right]} \tag{4.12}$$

In Figure 4.4 two values of the stiffness ratio are presented and compared with the canonical Euler-Bernoulli formulation (in red dashed line). The thickness of the beam is assumed constant: $s = 0.01\beta$.
Both values lead to hypersonic/superluminal propagation, the model on the left (a) shows superluminal group velocity right out of an unstable region, while the case depicted on the right (b) presents a superluminal phase velocity, as highlighted in section 4.1.1.

Two propagation maps are depicted for many values of the beam thickness, as

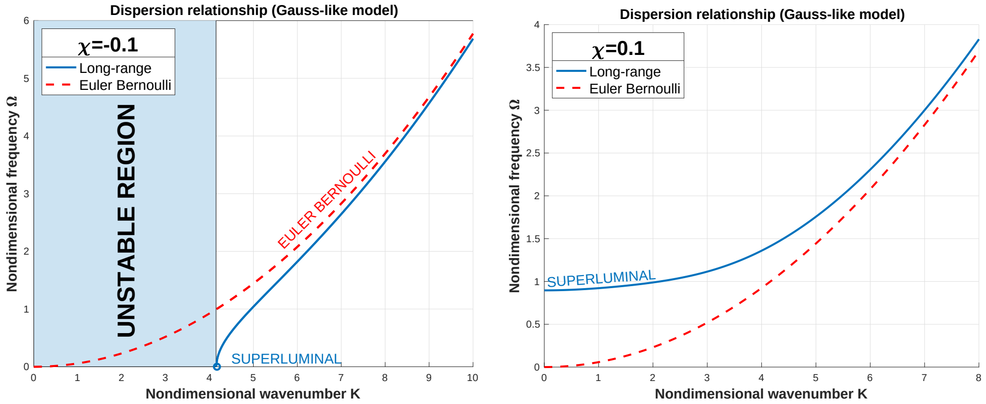

(a) $S = 0.01$, $\chi = -0.1$ **(b)** $S = 0.01$, $\chi = 0.1$

Figure 4.4. Dispersion relationships, Gauss-like top surface interaction beam.

in Figure 4.11 to summarize the behavior of the long-range beam with Gauss-like interaction on top surface. Both plots show the presence of unstable regions when the stiffness ratio is negative[13]. In addition, the thickness of the beam plays a valuable role in the definition of the unstable region. In fact, the smallest the thickness, the biggest the value of K_0, the transition wavenumber between the unstable and the stable regions.

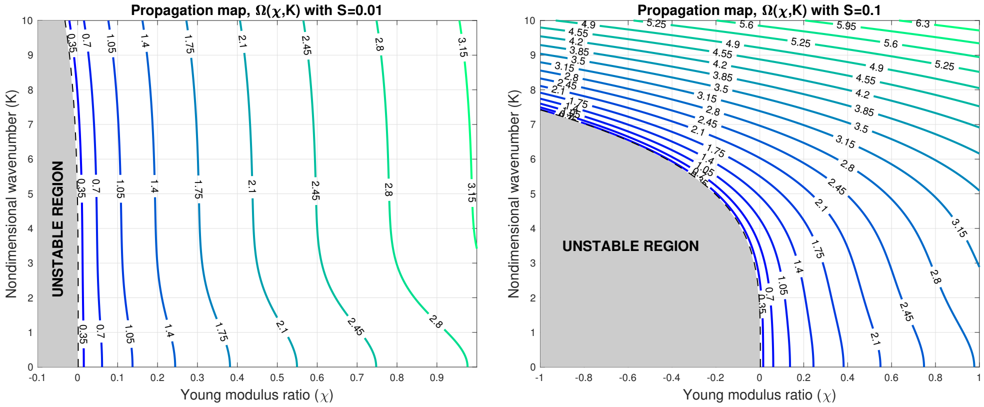

(a) $S = 0.01$ **(b)** $S = 0.1$

Figure 4.5. Dispersion map, Gauss-like top surface interaction beam.

Wave speed analysis

The nondimensional phase and group velocities are obtained:

$$C_\phi = \frac{\Omega}{K} = \pm \frac{\sqrt{\frac{1}{3}S^2K^4 + \chi\left[2\sqrt{2\pi} - \left(2 + S^2K^4\right)e^{-\frac{K^2}{4}}\right]}}{K} \tag{4.13a}$$

$$C_g = \frac{\partial \Omega}{\partial K} = \pm \frac{\frac{4K^3S^2}{3} + e^{-\frac{K^2}{4}}K\chi + \frac{1}{2}e^{-\frac{K^2}{4}}K^5S^2\chi - 4e^{-\frac{K^2}{4}}K^3S^2\chi}{2\sqrt{\frac{K^4S^2}{3} - 2e^{-\frac{K^2}{4}}\chi - e^{-\frac{K^2}{4}}K^4S^2\chi + 2\pi\sqrt{2}\chi}} \tag{4.13b}$$

From the analysis of the propagation velocities, some interesting phenomena emerge, as depicted in Figure 4.6:

As anticipated in the previous sections, some interesting phenomena appear in the long-range beams with Gauss-like interaction on the top surface, where, according to the sign of the stiffness ratio, superluminal region appears alternatively: phase velocity or group velocity for positive or negative stiffness ratios, respectively. Moreover, all the velocities asymptotically tend to the classical Euler-Bernoulli beam, and, for positive χ, for very low wavenumbers, the group velocity rapidly decreases, theoretically vanishing when $K \to 0$.

---

[13] remember that in the case of the rod the unstable region was found in positive χs

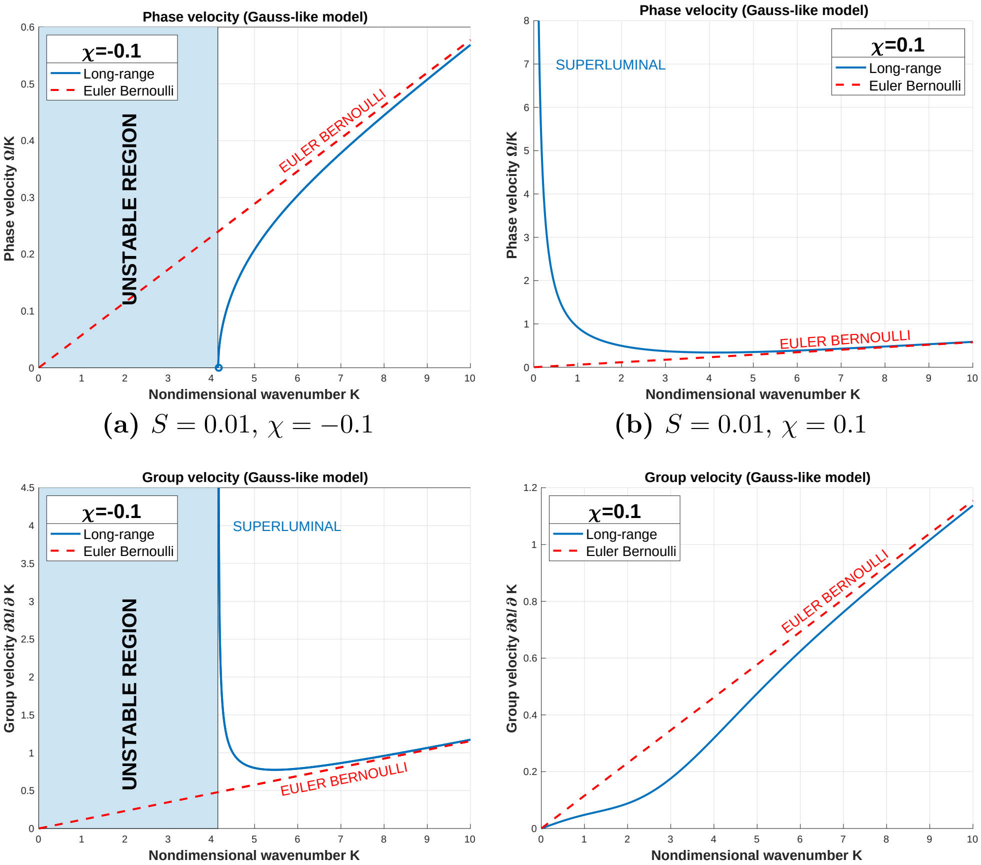

(a) $S = 0.01,\ \chi = -0.1$ **(b)** $S = 0.01,\ \chi = 0.1$

(c) $S = 0.01,\ \chi = -0.1$ **(d)** $S = 0.01,\ \chi = 0.1$

Figure 4.6. Dispersion velocities, Gauss-like top surface interaction beam.

4.1.2 Top and Bottom surface interaction

Analytical solution

The top-top interaction is the one evaluated in section 4.1.1, thus it is not discussed here. According to the Euler-Bernoulli beam model, $w(\dots)$ is sufficient to describe the displacement of the beam and $\boldsymbol{u}$ leads to:

$$u_x = -sw'(x,t) - sw'(\xi,t)) \tag{4.14a}$$

$$u_z = w(x,t) - w(\xi,t) \tag{4.14b}$$

with $w'(\dots) = \frac{\partial w(\dots)}{\partial x}$ and, remembering that $\boldsymbol{x} = \left(\begin{smallmatrix} x \\ s \end{smallmatrix}\right)$ and $\boldsymbol{\xi} = \left(\begin{smallmatrix} \xi \\ -s \end{smallmatrix}\right)$, with $\boldsymbol{g}_0 = \begin{bmatrix} \frac{\partial f(|\boldsymbol{r}|)}{\partial |\boldsymbol{r}|}\Big|_0 \frac{(x-\xi)^2}{|x-\xi|} & \frac{\partial f(|\boldsymbol{r}|)}{\partial |\boldsymbol{r}|}\Big|_0 \frac{2s(x-\xi)}{|x-\xi|} \\ \frac{\partial f(|\boldsymbol{r}|)}{\partial |\boldsymbol{r}|}\Big|_0 \frac{2s(x-\xi)}{|x-\xi|} & \frac{\partial f(|\boldsymbol{r}|)}{\partial |\boldsymbol{r}|}\Big|_0 \frac{4h^2}{|x-\xi|} \end{bmatrix} = \begin{bmatrix} g_{0_{11}} & g_{0_{12}} \\ g_{0_{21}} & g_{0_{22}} \end{bmatrix}$, the two-dimensional long-range force becomes:

$$\boldsymbol{r} f(|\boldsymbol{r}|) = f_0 \begin{pmatrix} x-\xi \\ 2s \end{pmatrix} + \begin{bmatrix} g_{0_{11}} & g_{0_{12}} \\ g_{0_{21}} & g_{0_{22}} \end{bmatrix} \begin{pmatrix} -sw'(x,t)-sw'(\xi,t)) \\ w(x,t)-w(\xi,t) \end{pmatrix} + f_0 \begin{pmatrix} -sw'(x,t)-sw'(\xi,t)) \\ w(x,t)-w(\xi,t) \end{pmatrix} \tag{4.15}$$

Bending moment From equation (4.3a)

$$m(\boldsymbol{x},t) = s\int_{-\infty}^{\infty} \left\{ f_0(x-\xi) + (g_{0_{11}} + f_0)\left[-sw'(x,t) - sw'(\xi,t)\right] + g_{0_{12}}\left[w(x) - w(\xi)\right]\right\} d\xi \tag{4.16a}$$

$$= s\int_{-\infty}^{\infty} f_0(x-\xi)d\xi -$$

$$- s^2 w'(x,t)\int_{-\infty}^{\infty} (g_{0_{11}} + f_0)d\xi -$$

$$- s^2 \int_{-\infty}^{\infty} (g_{0_{11}} + f_0)w'(\xi,t)d\xi + \tag{4.16b}$$

$$+ s\,w(x)\int_{-\infty}^{\infty} g_{0_{12}}d\xi - \tag{4.16c}$$

$$- s\int_{-\infty}^{\infty} g_{0_{12}}w(\xi)d\xi = \tag{4.16d}$$

$$= -s^2\left[(g_{0_{11}} + f_0) * w'(x,t)\right] - s\,g_{0_{12}} * w(x,t) \tag{4.16e}$$

Shear force From equation (4.3b)

$$p(\boldsymbol{x},t) = \int_{-\infty}^{\infty} \left\{2sf_0 + g_{0_{21}}\left[-sw'(x) + sw'(\xi)\right] + (g_{0_{22}} + f_0)\left[w(x,t) - w(\xi,t)\right]\right\} d\xi \tag{4.17a}$$

$$= 2s\int_{-\infty}^{\infty} f_0 d\xi -$$

$$- sw(x,t)\int_{-\infty}^{\infty} g_{0_{21}}d\xi -$$

$$- s\int_{-\infty}^{\infty} g_{0_{21}}w'(\xi,t)d\xi + \tag{4.17b}$$

$$w(x)\int_{-\infty}^{\infty} (g_{0_{22}} + f_0)d\xi - \tag{4.17c}$$

$$- \int_{-\infty}^{\infty} (g_{0_{22}} + f_0)w(\xi)d\xi = \tag{4.17d}$$

$$= 2s\bar{f}_0 - sg_{0_{21}} * w(x,t) + (\bar{g}_{22} + \bar{f}_0)w(x,t) - (g_{0_{22}} + f_0) * w(x,t) \tag{4.17e}$$

where $\bar{\Box} = \Box * 1$.

Bottom-Top interaction

For the Bottom-Top interaction, $\boldsymbol{x}$ and $\boldsymbol{\xi}$ are as follows: $\boldsymbol{x} = \left(\begin{smallmatrix} x \\ -s \end{smallmatrix}\right)$ and $\boldsymbol{\xi} = \left(\begin{smallmatrix} \xi \\ s \end{smallmatrix}\right)$, with $\boldsymbol{g}_0 = \begin{bmatrix} \left.\frac{\partial f(|\boldsymbol{r}|)}{\partial |\boldsymbol{r}|}\right|_0 \frac{(x-\xi)^2}{|x-\xi|} & \left.\frac{\partial f(|\boldsymbol{r}|)}{\partial |\boldsymbol{r}|}\right|_0 \frac{-2s(x-\xi)}{|x-\xi|} \\ \left.\frac{\partial f(|\boldsymbol{r}|)}{\partial |\boldsymbol{r}|}\right|_0 \frac{-2s(x-\xi)}{|x-\xi|} & \left.\frac{\partial f(|\boldsymbol{r}|)}{\partial |\boldsymbol{r}|}\right|_0 \frac{4h^2}{|x-\xi|} \end{bmatrix} = \begin{bmatrix} g_{0_{11}} & g_{0_{12}} \\ g_{0_{21}} & g_{0_{22}} \end{bmatrix}$, the two-dimensional long-range force becomes:

$$\boldsymbol{r}f(|\boldsymbol{r}|) = f_0 \left(\begin{smallmatrix} x-\xi \\ -2s \end{smallmatrix}\right) + \begin{bmatrix} g_{0_{11}} & g_{0_{12}} \\ g_{0_{21}} & g_{0_{22}} \end{bmatrix} \left(\begin{smallmatrix} sw'(x,t)+sw'(\xi,t)) \\ w(x,t)-w(\xi,t) \end{smallmatrix}\right) + f_0 \left(\begin{smallmatrix} +sw'(x,t)+sw'(\xi,t)) \\ w(x,t)-w(\xi,t) \end{smallmatrix}\right) \tag{4.18}$$

Bending moment From equation (4.3a)

$$m(\boldsymbol{x},t) = -s\int_{-\infty}^{\infty} \left\{ f_0(x-\xi) + (g_{0_{11}} + f_0)\left[sw'(x,t) + sw'(\xi,t)\right] + g_{0_{12}}\left[w(x) - w(\xi)\right]\right\} d\xi \tag{4.19a}$$

$$= -s\int_{-\infty}^{\infty} f_0(x-\xi)d\xi -$$

$$- s^2 w'(x,t)\int_{-\infty}^{\infty}(g_{0_{11}} + f_0)d\xi -$$

$$- s^2\int_{-\infty}^{\infty}(g_{0_{11}} + f_0)w'(\xi,t)d\xi - \tag{4.19b}$$

$$- s\, w(x)\int_{-\infty}^{\infty} g_{0_{12}} d\xi + \tag{4.19c}$$

$$+ s\int_{-\infty}^{\infty} g_{0_{12}} w(\xi)d\xi = \tag{4.19d}$$

$$= -s^2\left[(g_{0_{11}} + f_0) * w'(x,t)\right] + s\, g_{0_{12}} * w(x,t) \tag{4.19e}$$

Shear force From equation (4.3b)

$$p(\boldsymbol{x},t) = \int_{-\infty}^{\infty}\left\{-2sf_0 + g_{0_{21}}\left[sw'(x) + sw'(\xi)\right] + (g_{0_{22}} + f_0)\left[w(x,t) - w(\xi,t)\right]\right\} d\xi \tag{4.20a}$$

$$= -2s\int_{-\infty}^{\infty} f_0 d\xi +$$

$$+ sw(x,t)\int_{-\infty}^{\infty} g_{0_{21}} d\xi +$$

$$+ s\int_{-\infty}^{\infty} g_{0_{21}} w'(\xi,t)d\xi + \tag{4.20b}$$

$$w(x)\int_{-\infty}^{\infty}(g_{0_{22}} + f_0)d\xi - \tag{4.20c}$$

$$- \int_{-\infty}^{\infty}(g_{0_{22}} + f_0)w(\xi)d\xi = \tag{4.20d}$$

$$= -2s\bar{f}_0 + sg_{0_{21}} * w(x,t) + (g_{0_{22}}{}^{-}\!+ f_0)w(x,t) - (g_{0_{22}} + f_0) * w(x,t) \tag{4.20e}$$

where $\bar{\square} = \square * 1$.

Bottom-Bottom interaction

For the Bottom-Bottom interaction, $\boldsymbol{x}$ and $\boldsymbol{\xi}$ become as follows: $\boldsymbol{x} = \left(\begin{smallmatrix} x \\ -s \end{smallmatrix}\right)$ and $\boldsymbol{\xi} = \left(\begin{smallmatrix} \xi \\ -s \end{smallmatrix}\right)$, with $\boldsymbol{g}_0 = \begin{bmatrix} \left.\frac{\partial f(|\boldsymbol{r}|)}{\partial|\boldsymbol{r}|}\right|_0 \frac{(x-\xi)^2}{|x-\xi|} & 0 \\ 0 & 0 \end{bmatrix} = \begin{bmatrix} g_{0_{11}} & 0 \\ 0 & 0 \end{bmatrix}$, the two-dimensional long-range force becomes:

$$\boldsymbol{r} f(|\boldsymbol{r}|) = f_0 \left(\begin{smallmatrix} x-\xi \\ 0 \end{smallmatrix}\right) + \begin{bmatrix} g_{0_{11}} & 0 \\ 0 & 0 \end{bmatrix} \left(\begin{smallmatrix} -sw'(x,t)+sw'(\xi,t)) \\ w(x,t)-w(\xi,t) \end{smallmatrix}\right) + f_0 \left(\begin{smallmatrix} -sw'(x,t)+sw'(\xi,t)) \\ w(x,t)-w(\xi,t) \end{smallmatrix}\right) \tag{4.21}$$

Bending moment From equation (4.3a)

$$\begin{aligned} m(\boldsymbol{x},t) &= -s \int_{-\infty}^{\infty} \left\{ f_0(x-\xi) + (g_{0_{11}} + f_0) \left[-sw'(x,t) + sw'(\xi,t) \right] \right\} d\xi && (4.22\text{a}) \\ &= -s \int_{-\infty}^{\infty} f_0(x-\xi) d\xi + \\ &+ s^2 w'(x,t) \int_{-\infty}^{\infty} (g_{0_{11}} + f_0) d\xi - \\ &- s^2 \int_{-\infty}^{\infty} (g_{0_{11}} + f_0) w'(\xi,t) d\xi = && (4.22\text{b}) \\ &= -s^2 \left[(g_{0_{11}} + f_0) * w'(x,t) \right] + s^2 \left[(g_{0_{11}} \bar{+} f_0) w'(x,t) \right] && (4.22\text{c}) \end{aligned}$$

Shear force From equation (4.3b)

$$\begin{aligned} p(\boldsymbol{x},t) &= \int_{-\infty}^{\infty} + f_0 \left[w(x,t) - w(\xi,t) \right] d\xi && (4.23\text{a}) \\ &= w(x) \int_{-\infty}^{\infty} + f_0 d\xi - && (4.23\text{b}) \\ &- \int_{-\infty}^{\infty} f_0 w(\xi) d\xi = && (4.23\text{c}) \\ &= \bar{f_0} w(x,t) - f_0 * w(x,t) && (4.23\text{d}) \end{aligned}$$

where $\bar{\square} = \square * 1$.

Total contribution

The contributions coming from the cases depicted in Section 4.1.1 are combined, for the Gauss-like model, as follows:

$$p_{tot} = 2\bar{f}_{0_{TT}} w - 2f_{0_{TT}} * w - 2sg_{0_{21_{TB}}} * w' + 2(\bar{g}_{0_{22_{TB}}} + \bar{f}_{0_{TB}}) w - 2(g_{0_{22_{TB}}} + f_{0_{TB}}) * w \tag{4.24}$$

$$m_{tot} = 2s^2 (g_{0_{11_{TT}}} + f_{0_{TT}}) * w' - 2s^2 (g_{0_{11_{TB}}} + f_{0_{TB}}) * w' - 2sg_{0_{12_{TB}}} * w \tag{4.25}$$

there the pedices $\square_{TT}$ and $\square_{TB}$ indicate the TOP-TOP and TOP-BOTTOM contribution, respectively; moreover, for a more clear graphic appearance, the dependencies have been omitted.

Some terms have been simplified during the calculation because they vanish in the Gauss-like formulation. The remaining terms are as follows:

$$\bar{f}_{0_{TT}} = \mu A\beta\sqrt{\pi} \tag{4.26a}$$

$$f_{0_{TT}}\big|_x = \mu A e^{-\frac{x^2}{\beta^2}} \tag{4.26b}$$

$$g_{021_{TB}}\big|_x = g_{12_{TB}}\big|_x = -\frac{2\mu A}{\beta^2} s e^{-4\frac{s^2}{\beta^2}} x e^{-\frac{x^2}{\beta^2}} \tag{4.26c}$$

$$\bar{g}_{022_{TB}} + \bar{f}_{0_{TB}} = \mu A\beta\sqrt{\pi} e^{-4\frac{s^2}{\beta^2}} \left(1 - \frac{8s^2}{\beta^2}\right) \tag{4.26d}$$

$$(g_{022_{TB}} + f_{0_{TB}})\big|_x = \mu A e^{-4\frac{s^2}{\beta^2}} \left(1 - \frac{8s^2}{\beta^2}\right) e^{-\frac{x^2}{\beta^2}} \tag{4.26e}$$

$$(g_{011_{TT}} + f_{0_{TT}})\big|_x = \mu A(1 - \frac{2x^2}{\beta^2})e^{-\frac{x^2}{\beta^2}} \tag{4.26f}$$

$$(g_{011_{TB}} + f_{0_{TB}})\big|_x = \mu A e^{-4\frac{s^2}{\beta^2}}(1 - \frac{2x^2}{\beta^2})e^{-\frac{x^2}{\beta^2}} \tag{4.26g}$$

Substituting into (4.8), the Fourier transform in time and space leads to the following dispersion relationship:

$$\begin{aligned} & -\rho A\omega^2 + EIk^4 + 2\mu A\beta\sqrt{\pi} + 2\mu A\beta\sqrt{\pi}\left(1 - \frac{8s^2}{\beta^2}\right) e^{-4\frac{s^2}{\beta^2}} - 2\mu A\beta\frac{1}{\sqrt{2}} e^{-\frac{(\beta k)^2}{4}} - \\ & -4\mu A s^2 \frac{\sqrt{2}e^{-4\frac{s^2}{\beta^2}}}{\sqrt{\beta}} k^2 e^{-\frac{(\beta k)^2}{4}} - 2\mu A\beta \frac{\left(1 - \frac{8s^2}{\beta^2}\right) e^{-4\frac{s^2}{\beta^2}}}{\sqrt{2}} e^{-\frac{(\beta k)^2}{4}} + 2\mu A\beta^3 \frac{e^{-4\frac{s^2}{\beta^2}} - 1}{2\sqrt{2}} s^2 k^4 e^{-\frac{(\beta k)^2}{4}} = 0 \end{aligned} \tag{4.27}$$

In non dimensional parameters, equation (4.27) for a rectangular section beam, becomes:

$$\begin{aligned} \Omega^2 = & \frac{1}{3}S^2K^4 + 4\chi\sqrt{2}\sqrt{\pi} + 4\chi\sqrt{2}\sqrt{\pi}(1 - 8S^2)e^{-4S^2} - 4\chi e^{-\frac{K^2}{4}} - \\ & - 16\chi S^2K^2 e^{-4S^2} e^{-\frac{K^2}{4}} - 4\chi(1 - 8S^2)e^{-4S^2} e^{-\frac{K^2}{4}} - 2\chi\left(1 - e^{-4S^2}\right) S^2K^4 e^{-\frac{K^2}{4}} \end{aligned} \tag{4.28}$$

As in the case of the top surface interaction only, the case in which the two surfaces interact presents an unstable region for negative stiffness ratios and superluminal velocities, as depicted in Figure 4.7 for $s = 0.01\beta$.

In Figure 4.8 the propagation map for the top and bottom interaction surfaces for two values of the beam thickness is presented. Once again, the ratio between the thickness of the beam and the interaction length controls the spread of the instability region.

Wave speed analysis

From the analysis of the propagation velocities, some interesting phenomena emerge, as depicted in Figure 4.7:

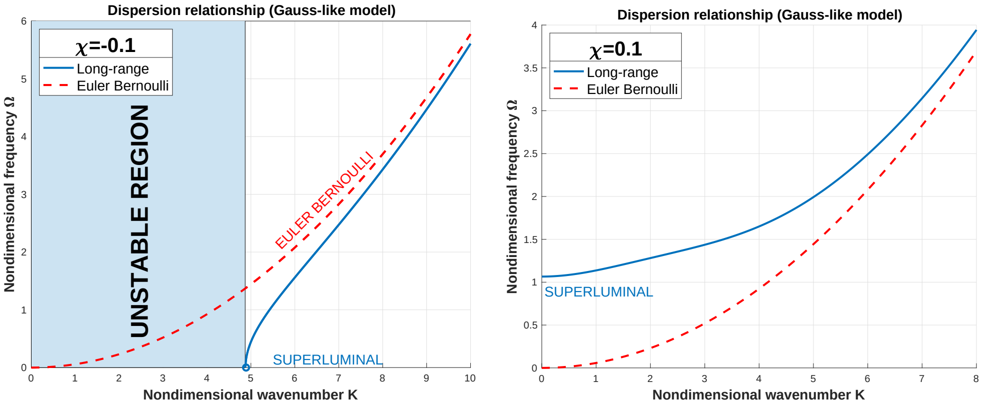

(a) $S = 0.01$, $\chi = -0.1$ **(b)** $S = 0.01$, $\chi = 0.1$

Figure 4.7. Dispersion relationships, Gauss-like top and bottom surfaces interaction beam.

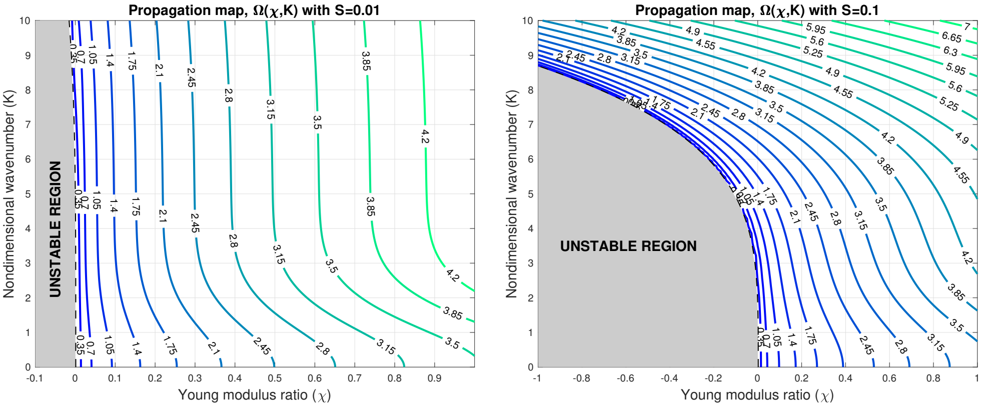

(a) $S = 0.01$ **(b)** $S = 0.1$

Figure 4.8. Dispersion map, Gauss-like top-bottom surface interaction beam.

4.2 Laplace-like

The case of the Laplace-like beam is considered. Starting from equation (4.8), the additional forces for the top surface interaction and for the top and bottom surfaces are considered.

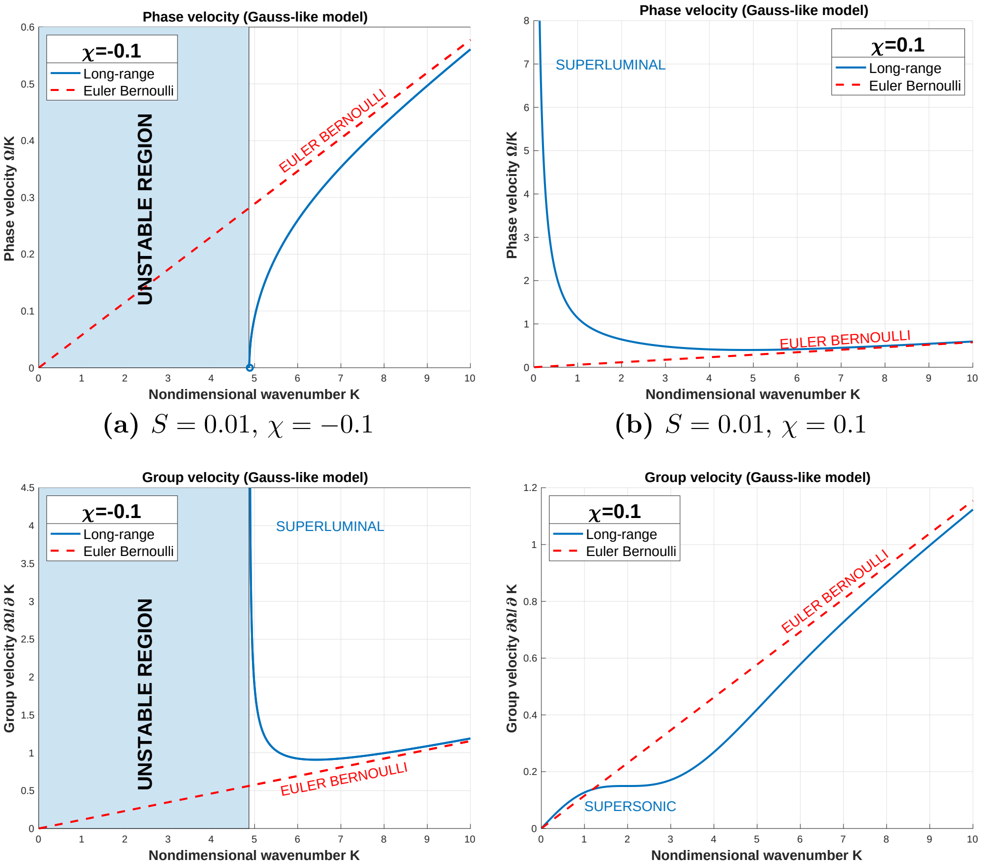

(a) $S = 0.01$, $\chi = -0.1$ **(b)** $S = 0.01$, $\chi = 0.1$

(c) $S = 0.01$, $\chi = -0.1$ **(d)** $S = 0.01$, $\chi = 0.1$

Figure 4.9. Dispersion velocities, Gauss-like top and bottom surfaces interaction beam.

4.2.1 Top surface interaction

Analytical Solution

The solution of the top surface interaction is evaluated in the previous section for the Gauss-like model. Starting from equation (4.9) the following values are considered:

$$\bar{f}_0 = 2A\mu\beta \tag{4.29a}$$

$$f_0|_x = \mu A e^{-\frac{|x|}{\beta}} \tag{4.29b}$$

$$(g_{0_{11}} + f_{0_{11}})|_x = \mu A(1 - \frac{x^2}{\beta})e^{-\frac{|x|}{\beta}} \tag{4.29c}$$

and the dispersion relationship for the Laplace-like beams reads into:

$$-\rho A\omega^2 + EIk^4 + 2\mu A\beta - \frac{\sqrt{\frac{2}{\pi}}\beta\mu A}{\beta^2 k^2 + 1} - k^4 s^2 \frac{2\sqrt{\frac{2}{\pi}}A\beta^3 k^2\mu}{(\beta^2 k^2 + 1)^2} = 0 \tag{4.30}$$

that, in nondimensional parameters becomes:

$$\Omega^2 - \frac{1}{3}S^2K^4 - \chi\left\{4\sqrt{2} - \left[\frac{4}{\sqrt{\pi}(K^2+1)} + S^2K^4\frac{8}{\sqrt{\pi}(K^2+1)^2}\right]\right\} = 0 \tag{4.31}$$

leading to the solution for the nondimensional frequency as follows:

$$\Omega = \pm\sqrt{\frac{1}{3}S^2K^4 + \chi\left\{4\sqrt{2} - \left[\frac{4}{\sqrt{\pi}(K^2+1)} + S^2K^4\frac{8}{\sqrt{\pi}(K^2+1)^2}\right]\right\}} \tag{4.32}$$

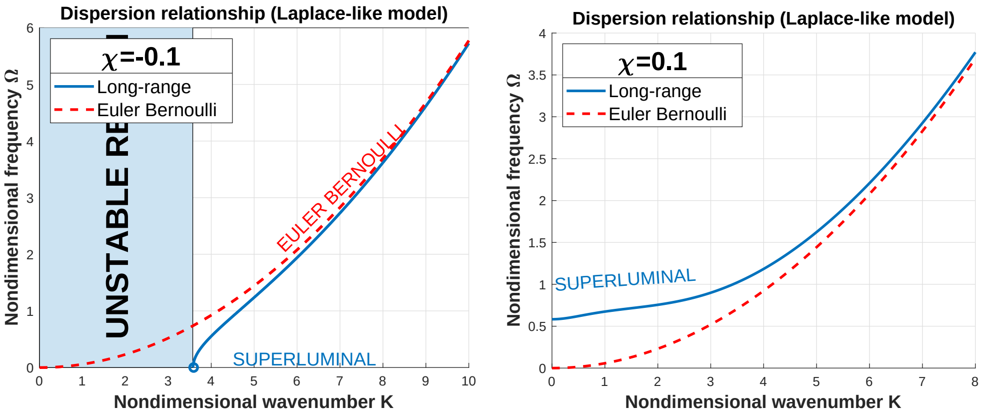

(a) $S = 0.01$, $\chi = -0.1$ **(b)** $S = 0.01$, $\chi = 0.1$

Figure 4.10. Dispersion relationships, Laplace-like top surface interaction beam.

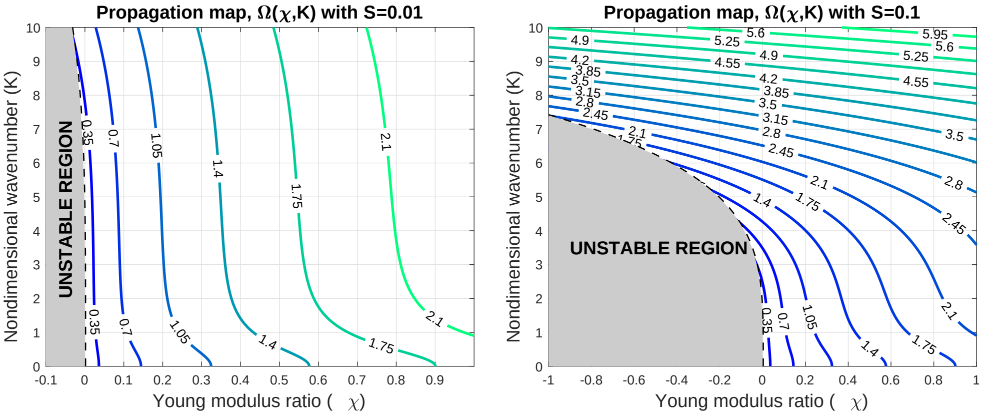

(a) $S = 0.01$ **(b)** $S = 0.1$

Figure 4.11. Dispersion map, Gauss-like top surface interaction beam.

Wave speed analysis

The nondimensional phase and group velocities are obtained:

$$C_\phi = \frac{\Omega}{K} = \pm \frac{\sqrt{\frac{1}{3}S^2K^4 + \chi\left\{4\sqrt{2} - \left[\frac{4}{\sqrt{\pi}(K^2+1)} + S^2K^4\frac{8}{\sqrt{\pi}(K^2+1)^2}\right]\right\}}}{K} \tag{4.33a}$$

$$C_g = \frac{\partial\Omega}{\partial K} = \pm \frac{\frac{4K^3S^2}{3} + \frac{8K\chi\left(K^2\left(1-4S^2\right)+1\right)}{\sqrt{\pi}(K^2+1)^3}}{2\sqrt{\frac{K^4S^2}{3} - \frac{4\chi(2K^4S^2+K^2+1)}{\sqrt{\pi}(K^2+1)^2} + 4\sqrt{2}\chi}} \tag{4.33b}$$

Some interesting phenomena emerge according to the propagation velocities, as depicted in Figure 4.12:

The Laplace-like beam with top interactive surface is solved in a closed form and subsequently the wave propagation analysis is completed. This is not the case of the Laplace-like beam with top and bottom interaction, where numerical approaches are needed to extract the dispersion relationship, not in the target of this thesis project. In forthcoming activities, the analysis will be extended also in evaluating the propagation regimes in beams with rectangular long-range interaction.

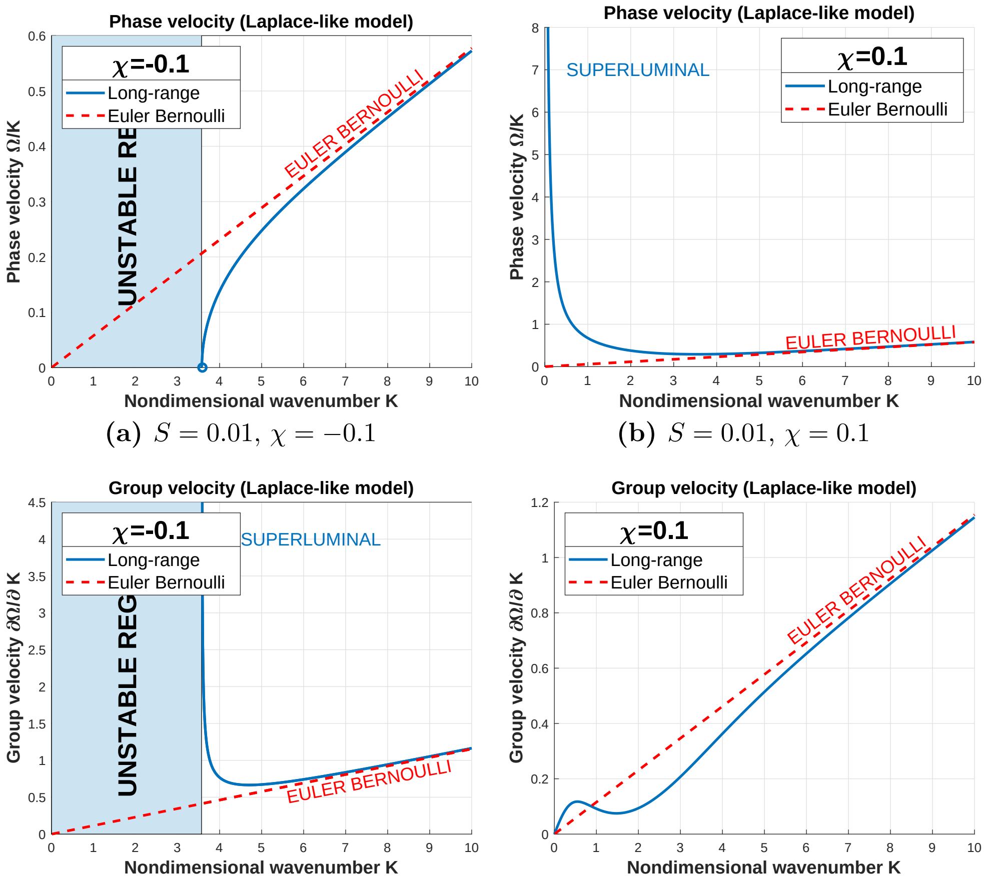

(a) $S = 0.01$, $\chi = -0.1$ **(b)** $S = 0.01$, $\chi = 0.1$

(c) $S = 0.01$, $\chi = -0.1$ **(d)** $S = 0.01$, $\chi = 0.1$

Figure 4.12. Dispersion velocities, Gauss-like top surface interaction beam.

Part II

Two-dimensional waves in metamaterials

Chapter 5

Long-range interactions in an elastic membrane

Interesting phenomena have been highlighted in the previous sections. The interaction will be susbequently expanded in two dimensional membranes subject to long-range interaction.
In a logical and consequential expansion of the work made for the one-dimensional metamaterials, the Gauss-like, Laplace-like and the rectangular models must be analysed. The first two cases do not present a closed form solution, thus, the analysis of such kind of interaction has not been developed in this thesis, whose aim is to find analytical solution for long-range interaction models. The rectangular model will be presented in the following section, together with the supporting mathematics. The two dismissed models open the chance to study a follow up of this thesis, focused on the deep analysis of such behaviors.
In the following formulation, the elements will be identified by the $\boldsymbol{x} = \left(\begin{smallmatrix} x \\ y \end{smallmatrix}\right)$ and $\boldsymbol{\xi} = \begin{pmatrix} \xi \\ \eta \end{pmatrix}$ coordinates systems.

5.1 Rectangular interaction

The dynamic equation of motion in two dimensions cannot be obtained from equation (2.15), because the interaction force does not respond to the formulation $\boldsymbol{F}(\boldsymbol{r}) = -f(|\boldsymbol{r}|)\boldsymbol{r}$. Introducing the long range interaction

$$\boldsymbol{F}(\boldsymbol{r}) = \mu\, H(|\boldsymbol{r}|)\, \boldsymbol{\varepsilon} \tag{5.1}$$

the equation of motion for the long-range membrane is introduced:

$$\rho \boldsymbol{w}_{tt} - P\, \nabla^2 \boldsymbol{w} + \iint_{\mathbb{R}^2} \mu\, H(|\boldsymbol{r}|)\, \boldsymbol{\varepsilon}\, d\xi\, d\eta = 0 \tag{5.2}$$

where P indicates the intensity per unit area of the stiffness operator.
As in the one-dimensonal case, the operator H describes the interaction window. An axial-symmetric rectangular window is introduced, as in equation (5.3) and plotted in Figure 5.1:

$$H(|\boldsymbol{r}|) = \begin{cases} 1, & |\boldsymbol{r}| \leq \beta \\ 0, & |\boldsymbol{r}| > \beta \end{cases} \tag{5.3}$$

where β, as in previous models, is a real positive quantity, indicating the interaction spread.

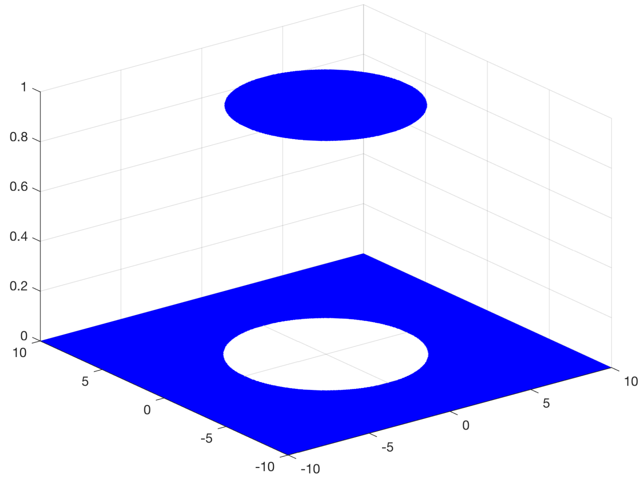

Figure 5.1. Rectangular long-range interaction in membranes for $\mu = 1$ and $\beta = 5$

5.1.1 Analytical Solution

Introducing equation (5.3) into equation (5.1), expliciting $\boldsymbol{\varepsilon} = \boldsymbol{w}(x, y) - \boldsymbol{w}(\xi, \eta)$ the following expression is obtained:

$$\rho \boldsymbol{w}_{tt} - P\,\nabla^2 \boldsymbol{w} + \mu \iint_{\mathbb{R}^2} H(|\boldsymbol{r}|)\,[\boldsymbol{w}(x, y) - \boldsymbol{w}(\xi, \eta)]\,d\xi\,d\eta = 0 \tag{5.4}$$

Splitting the double integral in two terms, remembering that $|\boldsymbol{r}| = \sqrt{(x-\xi)^2 - (y-\eta)^2}$, two expressions are obtained and analysed:

$$\begin{aligned} \mu \iint_{\mathbb{R}^2} H(|\boldsymbol{r}|)\boldsymbol{w}(x, y)\,d\xi\,d\eta =& \mu \boldsymbol{w}(x, y) \iint_{\mathbb{R}^2} H(|\boldsymbol{r}|)\,d\xi\,d\eta \\ =& \mu \boldsymbol{w}(x, y) \iint_{\mathbb{R}^2} H\left(x-\xi, y-\eta\right)d\xi\,d\eta \\ =& \mu\pi\beta^2 \boldsymbol{w}(x, y) \end{aligned} \tag{5.5}$$

and

$$\begin{aligned} -\mu \iint_{\mathbb{R}^2} H(|\boldsymbol{r}|)\boldsymbol{w}(\xi, \eta)\,d\xi\,d\eta =& -\mu \iint_{\mathbb{R}^2} H\left(x-\xi, y-\eta\right)\boldsymbol{w}(\xi, \eta)\,d\xi\,d\eta \\ =& -\mu\,\left[H(x, y) * \boldsymbol{w}(x, y)\right] \end{aligned} \tag{5.6}$$

that, substituted in equation (5.4) leads to the equation of motion:

$$\rho \boldsymbol{w}_{tt} - P\,\nabla^2 \boldsymbol{w} + \mu\pi\beta^2 \boldsymbol{w} - \mu\,[H * \boldsymbol{w}] = 0 \tag{5.7}$$

Applying two times the Fourier transform and collecting the transform of the displacement, a dispersion relationship for the long-range membrane is obtained:

$$-\rho\omega^2 + P\left(k_x^2 + k_y^2\right) + \mu\pi\beta^2 - \frac{\mu\beta}{\sqrt{k_x^2+k_y^2}} J_1\left(\beta\sqrt{k_x^2+k_y^2}\right) = 0 \tag{5.8}$$

where k_x and k_y are the wavenumbers along the two coordinates, and $J_1(\square)$ is the Bessel[14] function of the 1st kind[15] with $\alpha = 1$ [71]. Introducing new nondimensional groups:

$$\Omega = \sqrt{\frac{\rho}{P}}\beta\omega \qquad \text{nondimensional frequency} \tag{5.9a}$$

$$K_{x,y} = \beta k_{x,y} \qquad \text{nondimensional wavenumber} \tag{5.9b}$$

$$\chi = \frac{\mu\beta^4}{P} \qquad \text{stiffness ratio} \tag{5.9c}$$

equation 5.8 becomes, in nondimensional form:

$$-\Omega^2 + \left(K_x^2 + K_y^2\right) + \chi\left[\pi - \frac{J_1(\sqrt{K_x^2+K_y^2})}{\sqrt{K_x^2+K_y^2}}\right] = 0 \tag{5.10}$$

The two dispersion relations lead to the dispersion surfaces

$$\omega^2 = \frac{P}{\rho}\left(k_x^2 + k_y^2\right) + \frac{\mu}{\rho}\pi\beta^2 - \frac{\mu\beta}{\rho\sqrt{k_x^2+k_y^2}} J_1\left(\beta\sqrt{k_x^2+k_y^2}\right) \tag{5.11a}$$

$$\Omega^2 = \left(K_x^2 + K_y^2\right) + \chi\left[\pi - \frac{J_1(\sqrt{K_x^2+K_y^2})}{\sqrt{K_x^2+K_y^2}}\right] \tag{5.11b}$$

With analogous meanings with respect to the one-dimensional models, the parameter χ can be defined as the ratio between the long-range interaction stiffness $E^* = \mu\beta^4$, and the short range stiffness, ruled by P.

Introducing the radial wavenumber $K = \sqrt{K_x^2 + K_y^2}$, the dispersion surface is plotted in Figure 5.2, now reduced into a series of parametric curves, according to the magnitude of the stiffness ratio, compared to the case of the short-range membrane, in which the dispersion relationship is defined as $\omega^2 = c^2(k_x^2 + k_y^2)$ with $c = \sqrt{\frac{P}{\rho}}$ that, in radial direction, becomes a line crossing the zero at the origin.

The curves in Figure 5.2 indicate, similarly to what happened in the case of the one-dimensional, that the presence of the long-range term strongly modifies the oscillation frequency of the membrane. Nevertheless, a mathematical analysis shows that all the curves start from a non-zero value and asymptotically lead to the short-range membrane. In addition, when the stiffness ratio increases, some perturbation in the propagation appears, analysed in terms of phase and group velocities.

---

[14] Friedrich Wilhelm Bessel (July 22nd, 1784 - March 17th 1846) German astronomer, mathematician, physicist and geodesist

[15] defined by Bernoulli after Bessel's death: $J_\alpha(x) = \int_0^\pi \cos(\alpha\tau - x\sin\tau)\, d\tau$

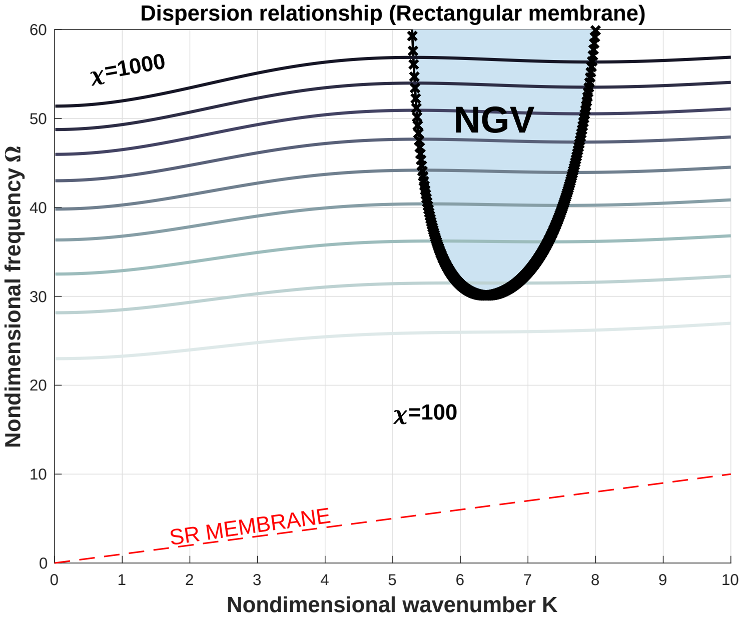

Figure 5.2. Dispersion curves for the rectangular membrane model as function fo the radial wavenumber

5.1.2 Wave speed analysis

The analysis of the phase and the group velocity is performed along two different directions, the former following the radial wavenumber approach, the latter by analyzing the propagation direction in both x and y axis.

phase velocity

The phase velocity is calculated in the following paragraphs.

radial wavenumber For the evaluation of the phase velocity in the radial direction, the radial dimensional wavenumber is introduced: $k = \sqrt{k_x^2 + k_y^2}$,

$$\begin{aligned}
c_\phi = \frac{\omega}{k} &= \pm\frac{\sqrt{\frac{T}{\rho}k^2 + \frac{\mu\pi}{\rho}\beta^2 - \frac{\mu\beta}{\rho k}J_1\left(\beta k\right)}}{k} \\
&= \pm\sqrt{\frac{P}{\rho} + \frac{\mu\pi}{\rho}\frac{\beta^2}{k^2} - \frac{\mu\beta}{\rho k^3}J_1\left(\beta k\right)} \\
&= \pm\sqrt{\frac{P}{\rho}}\sqrt{1 + \frac{\mu\pi}{P}\frac{\beta^2}{k^2} - \frac{\mu\beta}{P k^3}J_1\left(\beta k\right)} \\
&= \pm c\sqrt{1 + \frac{\mu\pi}{P}\frac{\beta^2}{k^2} - \frac{\mu\beta}{P k^3}J_1\left(\beta k\right)} \\
&= \pm c\sqrt{1 + \frac{\mu\beta^4}{P}\frac{\pi}{(\beta k)^2} - \frac{\mu\beta^4}{P}\frac{J_1\left(\beta k\right)}{(\beta k)^3}} \qquad (5.12)\\
&= \pm c\sqrt{1 + \chi\frac{\pi}{(\beta k)^2} - \chi\frac{J_1\left(\beta k\right)}{(\beta k)^3}} \\
&= \pm c\sqrt{1 + \chi\frac{\pi}{K^2} - \chi\frac{J_1\left(K\right)}{K^3}} \\
&= \pm c\frac{\sqrt{K^2 + \chi\left[\pi - \frac{J_1(K)}{K}\right]}}{K} \\
&= c\frac{\Omega}{K}
\end{aligned}$$

As well as for the previous models the nondimensional phase velocity $C_\phi = \dfrac{c_\phi}{c} = \dfrac{\Omega}{K}$ is introduced and plotted in Figure 5.3 for the radial wavenumber.

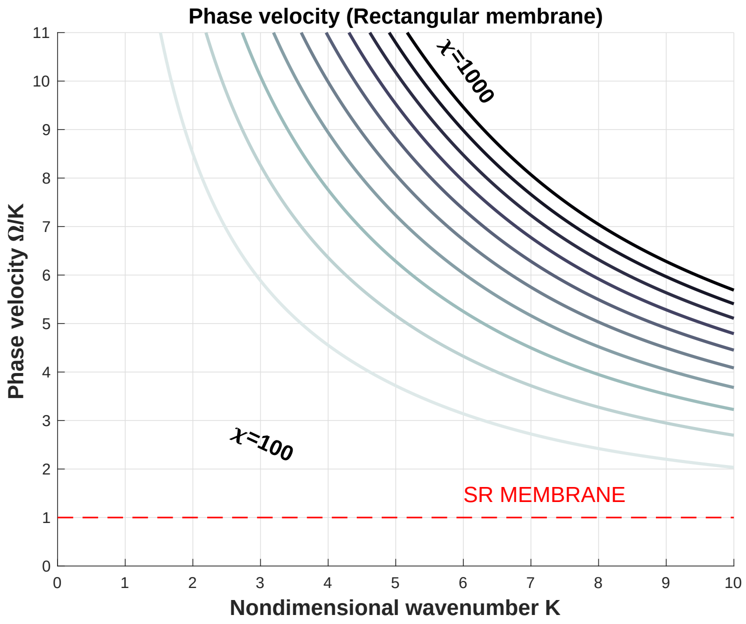

Figure 5.3. Phase velocity for the rectangular membrane model (radial wavenumber)

Coordinates propagation direction The phase velocity along the single axis is introduced as follows:

$$
\begin{aligned}
c_{\phi_x} = \frac{\omega}{k_x} &= \pm\frac{\sqrt{\frac{P}{\rho}(k_x^2+k_y^2)+\frac{\mu\pi}{\rho}\beta^2-\frac{\mu\beta}{\rho\sqrt{k_x^2+k_y^2}}J_1\left(\beta\sqrt{k_x^2+k_y^2}\right)}}{k_x} \\
&= \pm\sqrt{\frac{P}{\rho}}\frac{\sqrt{(k_x^2+k_y^2)+\frac{\mu\pi}{P}\beta^2-\frac{\mu\beta}{P\sqrt{k_x^2+k_y^2}}J_1\left(\beta\sqrt{k_x^2+k_y^2}\right)}}{k_x} \\
&= \pm c\frac{\sqrt{(k_x^2+k_y^2)+\frac{\mu\pi}{P}\beta^2-\frac{\mu\beta}{P\sqrt{k_x^2+k_y^2}}J_1\left(\beta\sqrt{k_x^2+k_y^2}\right)}}{k_x} \\
&= \pm c\frac{\sqrt{\beta^2(k_x^2+k_y^2)+\frac{\mu\pi}{P}\beta^4-\frac{\mu\beta^4}{P\beta\sqrt{k_x^2+k_y^2}}J_1\left(\beta\sqrt{k_x^2+k_y^2}\right)}}{\beta k_x} \\
&= \pm c\frac{\sqrt{[(\beta k_x)^2+(\beta k_y)^2]+\chi\pi-\frac{\chi}{\sqrt{(\beta k_x)^2+(\beta k_y)^2}}J_1\left(\sqrt{(\beta k_x)^2+(\beta k_y)^2}\right)}}{\beta k_x} \\
&= \pm c\frac{\sqrt{(K_x^2+K_y^2)+\chi\pi-\frac{\chi}{\sqrt{K_x^2+K_y^2}}J_1\left(\sqrt{K_x^2+K_y^2}\right)}}{K_x} \\
&= \pm c\frac{\sqrt{(K_x^2+K_y^2)+\chi\left[\pi-\frac{J_1\left(\sqrt{K_x^2+K_y^2}\right)}{\sqrt{K_x^2+K_y^2}}\right]}}{K_x} \\
&= c\frac{\Omega}{K_x}
\end{aligned}
\tag{5.13}
$$

and the nondimensional $x-$direction phase velocity is $C_{\phi_x} = \frac{c_{\phi_x}}{c} = \frac{\Omega}{K_x}$, depicted in Figure 5.4. The nondimensional $y-$direction phase velocity, for analogous calculus is $C_{\phi_y} = \frac{\Omega}{K_y}$.

The radial phase velocity shows similar trends independently of the intensity of the stiffness ratio, as depicted in Figure 5.3, where all the curves present a very high phase velocity at low wavenumbers, and superluminal phenomena emerge.

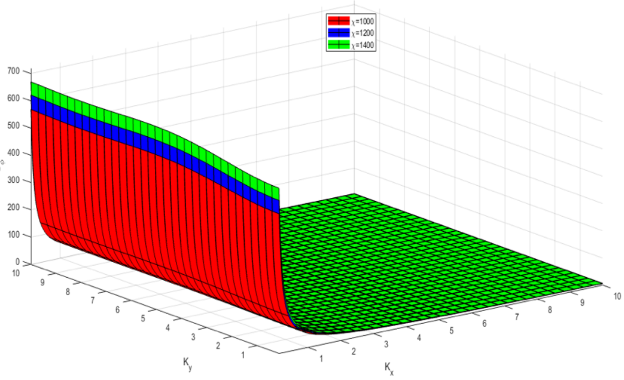

Figure 5.4. Phase velocity for the rectangular membrane model (x-direction propagation)

The same phenomenon comes out analyzing the propagation along the x and y directions. In fact, low wavenumbers superluminal phase velocity emerges, as shown in Figure 5.4.

group velocity

The group velocity is calculated as follows for the two directions in the next paragraphs.

radial wavenumber The dimensional group velocity is calculated:

$$
\begin{aligned}
c_g = \frac{\partial \omega}{\partial k} &= \pm \frac{\partial}{\partial k}\sqrt{\frac{P}{\rho}k^2 + \frac{\mu\pi}{\rho}\beta^2 - \frac{\mu\beta}{\rho k}J_1\left(\beta k\right)} \\
&= \pm \frac{\partial}{\partial k}\sqrt{\frac{P}{\rho}}\sqrt{k^2 + \frac{\mu\pi}{P}\beta^2 - \frac{\mu\beta}{Pk}J_1\left(\beta k\right)} \\
&= \pm c \frac{\partial}{\partial k}\sqrt{k^2 + \frac{\mu\pi}{P}\beta^2 - \frac{\mu\beta}{Pk}J_1\left(\beta k\right)} \\
&= \pm c \frac{\partial}{\partial k}\frac{1}{\beta}\sqrt{k^2 + \frac{\mu\pi}{P}\beta^4 - \frac{\mu\beta^4}{P\beta k}J_1\left(\beta k\right)} \\
&= \pm c \frac{\partial}{\partial (\beta k)}\sqrt{(\beta k)^2 + \frac{\mu\beta^4}{P}\pi - \frac{\mu\beta^4}{P}\frac{J_1\left(\beta k\right)}{(\beta k)}} \\
&= \pm c \frac{\partial}{\partial K}\sqrt{K^2 + \chi\left[\pi - \frac{J_1\left(K\right)}{K}\right]} \\
&= c\frac{\partial \Omega}{\partial K}
\end{aligned}
\tag{5.14}
$$

The nondimensional radial group velocity $C_g = \frac{c_g}{c} = \frac{\partial \Omega}{\partial K}$ is introduced and depicted in Figure 5.5.

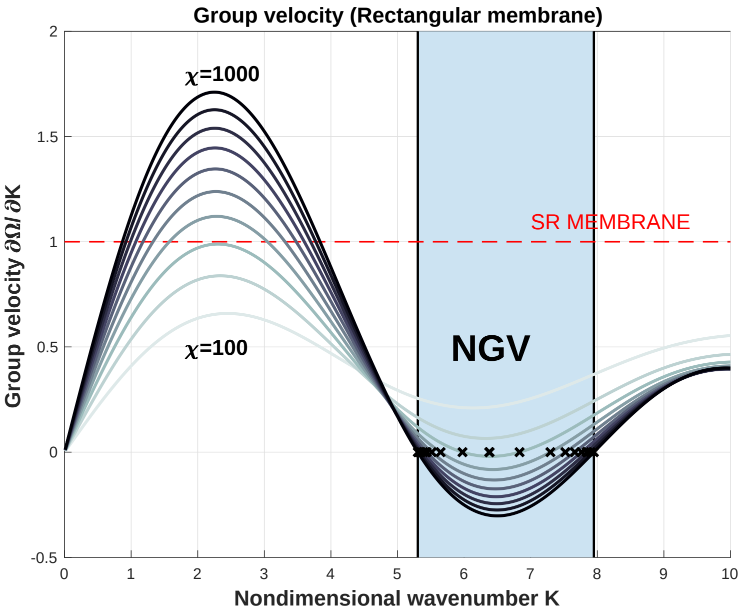

Figure 5.5. Group velocity for the rectangular membrane model (radial wavenumber)

Coordinates propagation direction The group velocity along the x-axis is introduced:

$$\begin{aligned}
c_{g_x} = \frac{\partial \omega}{\partial k_x} &= \pm \frac{\partial}{\partial k_x}\sqrt{\frac{P}{\rho}(k_x^2+k_y^2)+\frac{\mu\pi}{\rho}\beta^2-\frac{\mu\beta}{\rho\sqrt{k_x^2+k_y^2}}J_1\left(\beta\sqrt{k_x^2+k_y^2}\right)} \\
&= \pm\sqrt{\frac{P}{\rho}}\frac{\partial}{\partial k_x}\sqrt{(k_x^2+k_y^2)+\frac{\mu\pi}{P}\beta^2-\frac{\mu\beta}{P\sqrt{k_x^2+k_y^2}}J_1\left(\beta\sqrt{k_x^2+k_y^2}\right)} \\
&= \pm c\frac{\partial}{\partial k_x}\sqrt{(k_x^2+k_y^2)+\frac{\mu\pi}{P}\beta^2-\frac{\mu\beta}{P\sqrt{k_x^2+k_y^2}}J_1\left(\beta\sqrt{k_x^2+k_y^2}\right)} \\
&= \pm c\frac{\partial}{\partial k_x}\frac{1}{\beta}\sqrt{\beta^2(k_x^2+k_y^2)+\frac{\mu\pi}{P}\beta^4-\frac{\mu\beta^4}{P\beta\sqrt{k_x^2+k_y^2}}J_1\left(\beta\sqrt{k_x^2+k_y^2}\right)} \\
&= \pm c\frac{\partial}{\partial(\beta k_x)}\sqrt{[(\beta k_x)^2+(\beta k_y)^2]+\chi\pi-\frac{\chi}{\sqrt{(\beta k_x)^2+(\beta k_y)^2}}J_1\left(\sqrt{(\beta k_x)^2+(\beta k_y)^2}\right)} \\
&= \pm c\frac{\partial}{\partial K_x}\sqrt{(K_x^2+K_y^2)+\chi\pi-\frac{\chi}{\sqrt{K_x^2+K_y^2}}J_1\left(\sqrt{K_x^2+K_y^2}\right)} \\
&= \pm c\frac{\partial}{\partial K_x}\sqrt{(K_x^2+K_y^2)+\chi\left[\pi-\frac{J_1\left(\sqrt{K_x^2+K_y^2}\right)}{\sqrt{K_x^2+K_y^2}}\right]} \\
&= c\frac{\partial \Omega}{\partial K_x}
\end{aligned} \tag{5.15}$$

and the nondimensional $x-$direction group velocity is $C_{g_x} = \frac{c_{g_x}}{c} = \frac{\partial \Omega}{\partial K_x}$, plotted in Figure 5.6. The nondimensional $y-$direction group velocity, for analogous calculus is $C_{g_y} = \frac{\partial \Omega}{\partial K_y}$.

The presence of unusual propagation phenomena are strictly related to the intensity

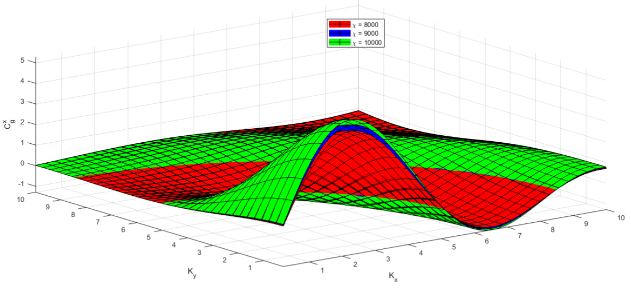

Figure 5.6. Group velocity for the rectangular membrane model (x-direction propagation)

of the stiffness ratio χ, as depicted in Figure 5.5 and Figure 5.6 , where Wave-stopping and Negative Group Velocity emerge only for high stiffness ratios $\chi >\sim 30$. Similar to what highlighted in the case of the one-dimensional rod with rectangular interaction, the radial group velocity presents a pseudo-harmonic trend, that asymptotically leads to the case of the short-range membrane, with constant group velocity. The oscillating behavior of the radial group velocity curve theoretically allows the presence of more than one NGV regions, but, the stiffness ratios to obtain such phenomena are pretty high $\chi > 10^4$, values that are barely reachable with physical quantities. Moreover, the surfaces in Figure 5.6 show that the wave-stopping and NGV regions are described with circles and rings, respectively.

Part III

Experiments and perspectives

Chapter 6

Design of an experimental demonstrator

Thanks to the achieved results in terms of wave propagation in the rod models and simulations, an experimental campaign has been carried on in the PhD project.
The experimental campaign has been developed in cooperation with the research team of the *Dynamics Laboratory* at the Mechanical Engineering Department of Technion, Israel Institute of Technology, directed by Prof. Izhak Bucher [72–75].
The experimental demonstrator consists in a prototype for testing the effects of nonlocal interactions in the dynamics of a finite discrete waveguide with long-range interactions. The nonlocality is provided by the use of permanent neodymium magnets.
The experimental setup is a finite waveguide composed by discrete elements, namely cells; each cell is linked to the frame and to its closest neighbor with metal (steel) strips, in charge for providing the short range stiffness. The cell is composed by a neodymium permanent magnet surrounded by an external plastic (ABS) case, capable of hosting the magnet and also clamping the metal strips. The first mass is solicited by an electromagnetic actuator (voice-coil) and the displacement of some of the cells have been monitored with laser interferometers.

The choice of the magnet-magnet interaction as nonlocal element has been made because the permanent magnets do not need an external energy supply; they can

Figure 6.1. Outlook of the experimental demonstrator

be handled in safety (no special protection hardware is needed) and, thanks to the choice of magnets with cubic shape, several configurations can be evaluated. The magnet to magnet interaction is modeled by a power-law type: $f(|\boldsymbol{r}|) \propto \frac{r}{|\boldsymbol{r}|^5}$, according to the magnetic dipole-dipole interaction described in [76]. Nevertheless, the interaction vanishes very soon, due to the high power order.

To limit the cell dimensions as much as possible (to obtain the best long-range interaction spread), the size of the magnet has been chosen to reach the best compromise between compact dimensions and force intensity (proportional to the volume of the magnet). Several design choices have been made to achieve the best results. The general model, as in the previous sections, shows interesting phenomena with high stiffness ratios, but this requirement is in strong contrast with the practical design feasibility. The magnetostatic long-range forces, in fact, lead to small equivalent stiffness (E^*): to obtain high ratios (χs), very soft springs are needed, in contrast with the values attainable with steel springs. The choice of using steel strips as springs has been made to guarantee the waveguide not to collapse under his own weight. For that reason the presence of springs connecting each cell with the ground (*sky-hook* springs) is necessary, even if consisting in an additional short-range stiffness term, further compromising the stiffness ratio of the waveguide. The design parameters are summarized in Table 6.1:

The number of cells is limited to 13 due to the overall dimensions of the setup, that is around 90 cm long.

Description	Symbol	Quantity	Unit
Number of cells	N	13	
Magnetic interaction intensity	μ	1.1964x10^{-7}	(N/m^4)
Mass of the magnet	m_{mag}	7.6x10^{-3}	(kg)
Mass of the plastic support	m_{case}	4.2x10^{-3}	(kg)
Mass of the actuator (mobile section)	m_{coil}	60x10^{-3}	(kg)
Mass of the actuator/1st cell support	m_{supp}	249x10^{-3}	(kg)
Stiffness of the sky-hook springs	k_{sh}	382.6	(N/m)
Stiffness of the cell springs	k_{cell}	369.9	(N/m)

Table 6.1. Demonstrator design parameters.

A preliminary experimental campaign has been made to verify the presence of shifts in the frequency response of the system, due to the presence of nonlocal interactions. The data acquisition chain, shown in Figure 6.2 indicates the hardware involved in the measurement. In general, the workstation is connected to the data acquisition system, capable of both receiving information from the sensors, and sending data to the actuator. The actuator has a control hardware capable of converting the information received from the workstation into an electrical signal to send to the voice-coil. Moreover, a low voltage output signal is sent from the actuator control hardware to the data acquisition system, to read the actual current signal sent to the actuator.

The laser sensors acquire the displacements of the cells, converted into voltage and sent to the acquisition system. The information is sent to the workstation, on which

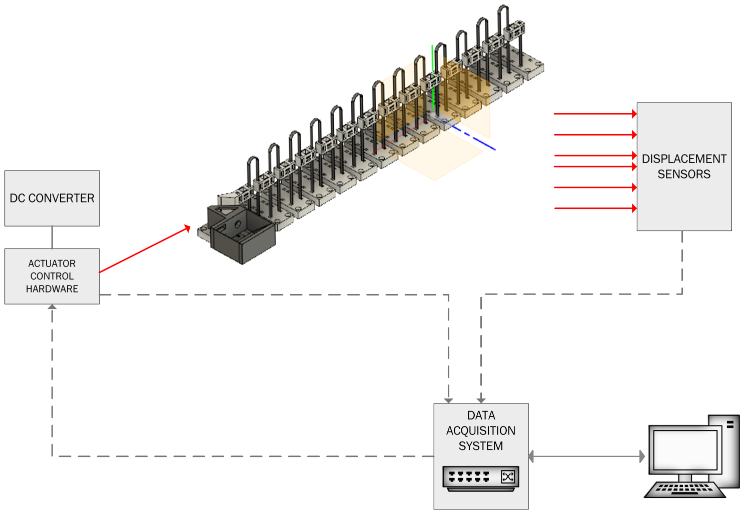

Figure 6.2. Measurement chain

an acquisition software is responsible of the data logging procedure.
Some auxiliary hardware is present, such as a DC converter capable of providing the power supply to the actuator.
The acquisition campaign has been set up to obtain the frequency response of the system, as a preliminary dat acquisition campaign.

Chapter 7

Preliminary results

The experimental configuration of the demonstrator cannot lead to the evaluation of Wave-Stopping, Negative Group Velocity or superluminal effects; nevertheless, the presence of magnetic interaction leads to perturbation in the dynamic response of the waveguide.
The choice of cubic magnets allows the waveguide to be tested under three different configurations. Namely the three setups are classified as follows:

- **Short-range configuration:** Each magnet is oriented to have the face with both north and south pole perpendicular to the abscissa. According to this configuration, negligible magnetic interaction is registered;
- **Repulsive configuration:** Each magnet is oriented to have the face with north/south magnetic poles facing the same pole of the first neighbor. According to this configuration, a prevalent repulsive magnetic interaction is registered;
- **Attractive configuration:** Each magnet is installed with the same orientation, each magnet will expose his north/south pole face to the opposite of the waveguide. According to this configuration, attractive interaction is registered.

The three configurations are presented in Figure 7.1:

The FFT of the system has been obtained by exciting the system with stepped sine waves. An excitation loop has been designed. Each iteration excites the system with a single frequency sine force. The data acquisition starts when the system reaches a stationary regime, and the displacement is collected.
The processing algorithm is based on the Non Linear Least Square method. It detects the actual frequency and reads the amplitude of the displacement for each degree of freedom. The ratio between the amplitude of the excitation and the amplitude of the displacement gives the frequency response. In Figure 7.2 the FFT of some DoFs of the system in the three configurations is presented. The excitation bandwidth spans from 10 to 60 Hz, with $\Delta f = 0.2Hz$.

The plots in Figure 7.2 show the frequency response (magnitude and phase) of three masses, in each window, each line corresponds to a configuration.
A graphical analysis of the plots shows that the frequency responses are comparable for the three configurations. Weak magnetic interaction is registered, if compared to

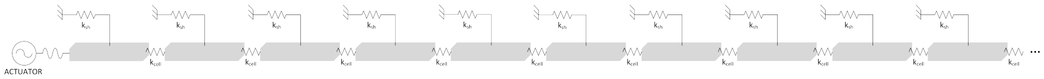

(a) Short-range configuration

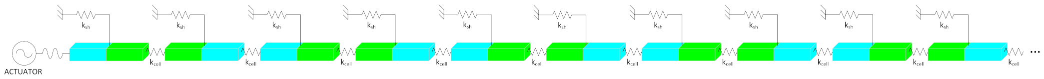

(b) Repulsive configuration

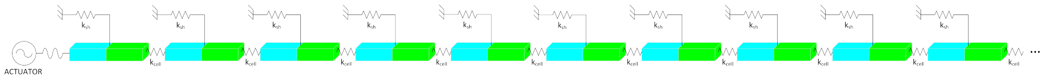

(c) Attractive configuration

Figure 7.1. Experimental configurations

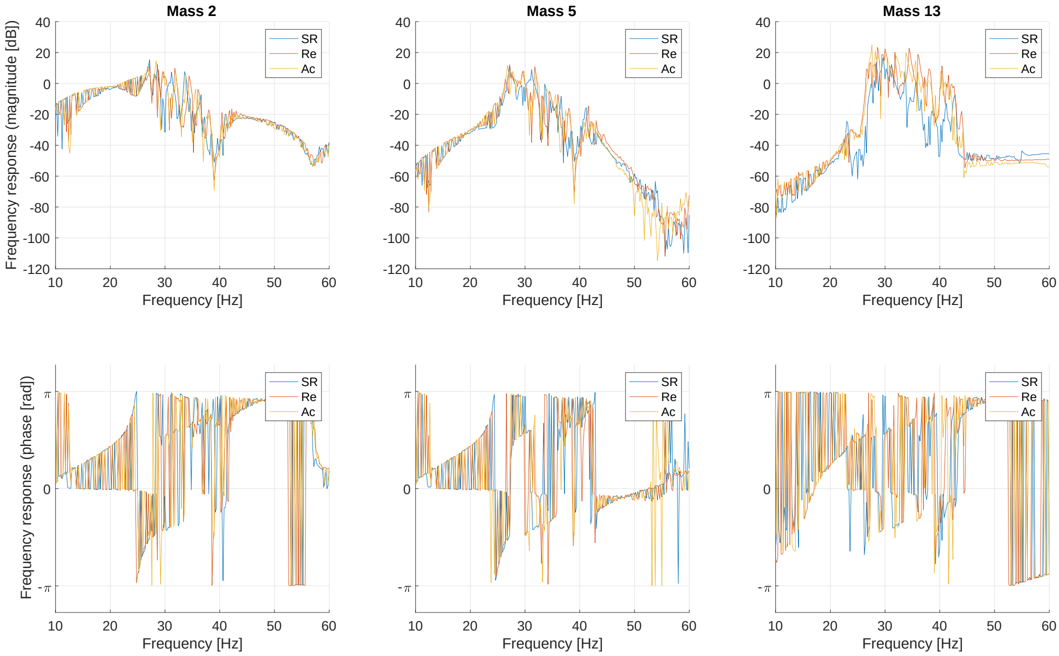

Figure 7.2. FFT of the experimental waveguide

the local stiffness. Nevertheless, some differences emerge.

Mass 2 At low frequencies (10-20 Hz) the frequency response is high. The support of the voice coil shift the first natural frequency around 20 Hz and increases the response at lower frequencies. Between 30 Hz and 40 Hz a shift of the resonances is registered, and, from 40 to 60 Hz, no important shifts appear.

Mass 5 In mass 5 the effects of the coil support is less evident, and the greatest shifts emerge from 30 Hz to 40 Hz. Also from 50 Hz to 60 Hz the frequency response changes.

Mass 13 A richer response emerge around 25 Hz for the active configurations (Repulsive and attractive). In addition, the bigger shift is present between 30 Hz and 40 Hz, as for the other masses.

This preliminary results gives important hints for the next experimental campaigns. The acquisition bandwidth can be extended towards higher frequencies, because the presence of some resonances around 60 Hz needs to be investigated.
Most of the shifts emerge from 30 Hz to 40 Hz, thus, a more detailed analysis of this bandwidth is desirable. Several acquisition will be made. Moreover, the setup should guarantee a higher definition of the response curves. Hence, Δf must reduce.

Chapter 8

Conclusions

This thesis presents the investigation carried on by the author during a three year PhD program in theoretical and applied mechanics.

The analysis has shown how the presence of long-range nonlocal connections can produce unusual effects in wave propagation of elastic metamaterials.

A general interaction model has been presented. The analysis has been carried on in a detailed analysis for one-dimensional waveguides with long-range interactions. The models are ruled by second and fourth order local interaction, i.e. following the D'Alembert and Euler-Bernoulli dynamic models, respectively. In addition the case of an elastic membrane has been evaluated.

The studied cases have been evaluated according to three interaction families: the Gauss-like, the Laplace-like and the rectangular interactions. All the three interaction forces respect the action-reaction principle, and all of them are function of the mutual distance between different particles of the medium. In addition, the Gauss-like and the Laplace-like forces rapidly decay with the distance; physically mimicking the behavior of several interactions present in nature such as electrostatic, magnetostatic or gravitational forces. The rectangular interaction is a constant elastic interaction living in a limited interaction range, namely a radius (in membranes) or a segment (in rods).

The different interactions have been analysed and closed form dispersion relationships have been calculated. Each combination of elastic model with interaction force has been depicted in a propagation map. The surface on the propagation maps is the plot of the time frequency, depicted as function of the space frequency. A long-range parameter has been introduced: the stiffness ratio, χ; a nondimensional group comparing the long-range interaction to the short-range forces.

The maps of the long-range rods (for Gauss-like and Laplace-like forces) show different propagation behaviors, according to the sign and to the magnitude of χ: when the local elasticity overcomes the nonlocal interaction, a mode propagation phenomenon emerge. For strongly negative ratios Wave-Stopping and Negative Group Velocity phenomena emerge. For high (positive) stiffness ratios an instability region appears at low space frequencies (wavenumbers), and, barely in the stable propagation region, Superluminal group velocity is registered.

The rectangular long-range interaction rod has physical meaning only for positive values of the stiffness ratios. A shift towards the high frequencies of the dispersion relationship is registered coherently with the increasing of the magnitude of the stiffness ratios. In addition, Wave-Stopping and Negative Group Velocity regions appear, together with the presence of Superluminal phase velocity regions for very low wavenumbers.

In the case of long-range beams, two kind of interactions have been evaluated, long-range top surface and long-range top and bottom surfaces. Gauss-like (top surface and top and bottom surfaces) and Laplace-like (Top surface) have been considered. In both cases, for negative wavenumbers unstable regions and Superluminal group velocities appear, the thinnest the beam, the widest the instability region. For positive stiffness ratios, a shift is present, as well as in the case of rectangular rods, together with the presence of Superluminal phase velocity at low wavenumbers.

In two dimensions, the case of a rectangular interaction membrane is considered. As in the one-dimensional rod with analogous interaction, the presence of Wave-Stopping, Negative Group Velocity and Superluminal phase velocity regions is confirmed.

Some numerical simulations have been developed to corroborate the presence of such propagation phenomena. Finite media subject to long-range interactions have been simulated. The results obtained for the Gauss-like and Laplace-like rods are encouraging and give a hint to prosecute with additional simulations, aimed to test the model/interaction combinations not investigated in this project.

The results obtained with the simulations of rod models opened the possibility to design an experimental demonstrator, built in cooperation with with Prof. Izhak Bucher and the team of the Dynamics Laboratory at Technion, Israel institute of technology in Haifa. The preliminary setup has been used to test the presence of a frequency response shift in elastic waveguides with long-range magnetic interaction. Three configurations have been considered. Such preliminary results open the way in pursuing with the experimental campaign. To achieve peculiar phenomena, nevertheless, a re-design of the experimental setup is necessary: due to the insufficient strength of magnets in modifying solid media dynamics.

The generality of the presented physical-mathematical model: a local interaction system added with nonlocal terms, can be applied in wide ranges. Not only in physics, such as in the regulation of complex physical systems, but also, for instance, in social dynamics. Recent studies in the population dynamics [77] show how elastic connections can be used to model the behaviour of the crowds; dynamic modeling can also be applied to predict and prevent the risk on catastrophic events [78]. Moreover, also the traffic dynamics can be modeled, according to long-range models [79], demonstrating how the collective behaviour of individuals can be described as a population of particles subject to wave models, as described in the present investigation.

Appendix A

Numerical solutions for the one-dimensional Gauss-like waveguide (Frequency domain)

The analysis in Section 3.1 is carried on solving the dispersion relationship in the wavenumber domain. In the current appendix a numerical algorithm for the solution of the dispersion relationship in the frequency domain is presented.

The transcendent nature of the dispersion relationship leads to the presence of an infinite set of numerable solutions for each frequency value. Uncontrolled root finding algorithms lead to random local minima; distinguishing the different dispersion curves is not possible. In Figure A.1, the different solutions are plotted with green circles to qualitative observe the nature of the solutions. The random algorithm are tested for low values of the stiffness ratio χ.

A canonical Newton[16]-Raphson[17] method is applied. Special initial guesses are chosen: the hypothesis of at least continuous dispersion curves is made, thanks to the preliminary graphical results in Figure A.1.

The root finding algorithm works as a two-dimensions loop, where once the local frequency value is evaluated, one of the $i-th$ curve is considered. The loop in the frequency starts at $\Omega = 0$, where analytical solutions are found by solving equation (A.1):

$$\begin{aligned} \Omega^2 - K^2 + \chi K^2 e^{-\frac{K^2}{4}}\Bigg|_0 &= 0 \\ K_{0_i}^2 \left(1 - \chi e^{-\frac{K_{0_i}^2}{4}}\right) &= 0 \end{aligned} \tag{A.1}$$

The dummy solutions $K_{0_{1,2}} = 0$ correspond to the purely real and purely imaginary trends. Solving the term between the parenthesis:

$$\chi e^{-\frac{K_{0_i}^2}{4}} = 1$$

---

[16] Sir Isaac Newton (January 4th 1643 - March 31st 1727) English mathematician, astronomer, theologian, author and physicist.

[17] Joseph Raphson (c. 1648 - c. 1715) English mathematician.

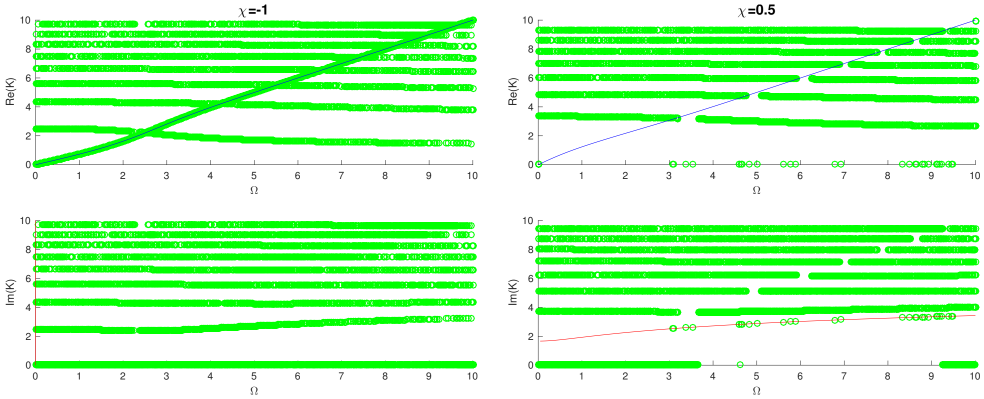

(a) $\chi = -1$ **(b)** $\chi = 0.5$

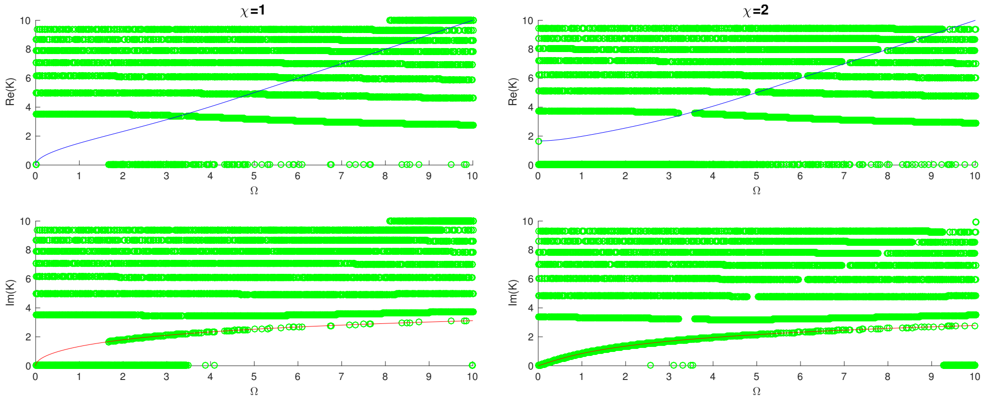

(c) $\chi = 1$ **(d)** $\chi = 2$

Figure A.1. Numerical solutions of the dispersion relationships (green circles in digital version) for different values of χ (-1, 0.5, 1, 2) compared with the real and purely imaginary analytical solution (blue and red lines in digital version respectively)

in $\chi = 0$ the D'Alembert waveguide is verified, and the only solution is $K_{0_{1,2}} = 0$. For $\chi \neq 0$:

$$
\begin{aligned}
e^{-\frac{K_{0_i}^2}{4}} &= \frac{1}{\chi} \\
-\frac{K_{0_i}^2}{4} + 2\pi \jmath i &= -\ln \chi \\
\frac{K_{0_i}^2}{4} &= 2\pi \jmath i + \ln \chi \\
K_{0_i} &= \pm 2\sqrt{2\pi \jmath i + \ln \chi}
\end{aligned}
$$

where the first $2(i+1)$ solutions are found for $\Omega = 0$.
For the following Ω_j steps of the frequency loop, the initial guesses are the solutions obtained for $\Omega = \Omega_{j-1}$. For the 1^{st} step of the loop, the solutions are the K_{0_i} values calculated as in equation (A.1).
The solution for 5 dispersion curves is depicted in Figure A.2.

Observing the plots in Figure A.2, interesting behaviour emerge. In blue it is

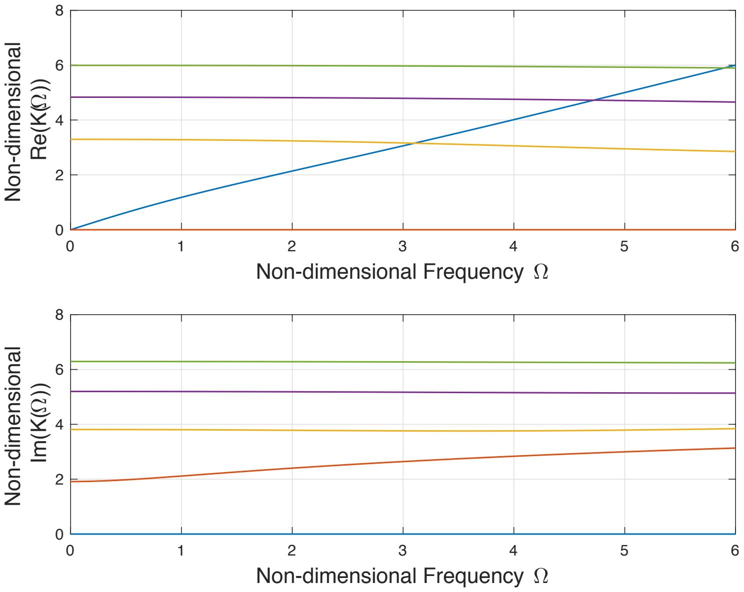

Figure A.2. Long-range Gauss-like waveguide dispersion curves (Non-dimensional frequency domain)

possible to notice the purely real dispersion curve, ruled by the inverse relation $\Omega = K\sqrt{1-\chi e^{-\frac{K^2}{4}}}$. In addition, a purely imaginary curve appears, apparently linked to near field phenomena, and several complex curves appear. Such solutions have no physical meaning, if compared to the purely real solutions. For this reason the focus have been moved to the analytical solutions discussed in Section 3.1.

Appendix B

Analytical solutions for the one-dimensional Laplace-like waveguide (Frequency domain)

The Laplace-like model leads to a rational dispersion relationship, in the wavenumber. The order of the numerator is 6, and it is a biquadratic polynomial. The only two domain poles of the dispersion relationship are in $K = \pm\jmath$, but, solving with Cardano[18]'s method for the solutions of 3rd order equations, the poles appear not to be solutions of the equation, as in equations (B.1), (B.2), and (B.3).

$$\begin{aligned}K_{3,4} = \pm\frac{1}{\sqrt{3}\sqrt[8]{\pi}} \Biggl\{ \biggl[& 24\chi + \sqrt{\pi}\left(\Omega^2+1\right)^2 + \sqrt[4]{\pi}\Omega^2 - 2\biggl(36\sqrt[4]{\pi}\chi\left(\Omega^2-2\right) + \pi^{3/4}\left(\Omega^2+1\right)^3 \\ & + 6\sqrt{6}\sqrt{-\chi\left(64\chi^2 + 2\sqrt{\pi}\chi\left(\Omega^4+20\Omega^2-8\right) + \pi\left(\Omega^2+1\right)^3\right)}\biggr)^{\frac{1}{3}} \\ & + \biggl(36\sqrt[4]{\pi}\chi\left(\Omega^2-2\right) + \pi^{3/4}\left(\Omega^2+1\right)^3 \\ & +6\sqrt{6}\sqrt{-\chi\left(64\chi^2 + 2\sqrt{\pi}\chi\left(\Omega^4+20\Omega^2-8\right) + \pi\left(\Omega^2+1\right)^3\right)}\biggr)^{\frac{2}{3}}\biggr] \\ & \biggl[36\sqrt[4]{\pi}\chi\left(\Omega^2-2\right) + \pi^{3/4}\left(\Omega^2+1\right)^3 \\ & +6\sqrt{6}\sqrt{-\chi\left(64\chi^2 + 2\sqrt{\pi}\chi\left(\Omega^4+20\Omega^2-8\right) + \pi\left(\Omega^2+1\right)^3\right)}\biggr]^{-\frac{1}{3}} \Biggr\} \end{aligned} \tag{B.1}$$

---

[18] Gerolamo Cardano (September 24th 1501 - September 21st 1576) Italian mathematician, physician, biologist, physicist, chemist, astrologer, astronomer, philosopher, writer, and gambler

$$
\begin{aligned}
K_{3,4} = \pm\frac{1}{\sqrt{6}\pi^{3/8}} \Bigg\{ \Bigg[& 24i\left(\sqrt{3}+\jmath\right)\sqrt{\pi}\chi + \jmath\pi\sqrt{3}\left(\Omega^2+2\right)\Omega^2 - \pi\left(\Omega^2+1\right)^2 \\
& +2\pi^{3/4}\Omega^2 - 2\Bigg(36\sqrt[4]{\pi}\chi\left(\Omega^2-2\right) + \pi^{3/4}\left(\Omega^2+1\right)^3 \\
& +6\sqrt{6}\sqrt{-\chi\left(64\chi^2+2\sqrt{\pi}\chi\left(\Omega^4+20\Omega^2-8\right)+\pi\left(\Omega^2+1\right)^3\right)}\Bigg)^{\frac{1}{3}} \\
& +\left(-1-\jmath\sqrt{3}\right)\sqrt{\pi}\Bigg(36\sqrt[4]{\pi}\chi\left(\Omega^2-2\right) + \pi^{3/4}\left(\Omega^2+1\right)^3 \\
& +6\sqrt{6}\sqrt{-\chi\left(64\chi^2+2\sqrt{\pi}\chi\left(\Omega^4+20\Omega^2-8\right)+\pi\left(\Omega^2+1\right)^3\right)}\Bigg)^{\frac{2}{3}}\Bigg] \\
& \Bigg[36\sqrt[4]{\pi}\chi\left(\Omega^2-2\right) + \pi^{3/4}\left(\Omega^2+1\right)^3 \\
& +6\sqrt{6}\sqrt{-\chi\left(64\chi^2+2\sqrt{\pi}\chi\left(\Omega^4+20\Omega^2-8\right)+\pi\left(\Omega^2+1\right)^3\right)}\Bigg]^{-\frac{1}{3}}\Bigg\}
\end{aligned}
\tag{B.2}
$$

$$
\begin{aligned}
K_{5,6} = \pm\frac{1}{\sqrt{6}\pi^{3/8}} \Bigg\{ \Bigg[& -\pi\left(\Omega^2+1\right)^2 + 2\pi^{3/4}\Omega^2 - 2\Bigg(36\sqrt[4]{\pi}\chi\left(\Omega^2-2\right) + \pi^{3/4}\left(\Omega^2+1\right)^3 \\
& +6\sqrt{6}\sqrt{-\chi\left(64\chi^2+2\sqrt{\pi}\chi\left(\Omega^4+20\Omega^2-8\right)+\pi\left(\Omega^2+1\right)^3\right)}\Bigg)^{\frac{1}{3}} \\
& +\jmath\sqrt{\pi}\Big(-24\left(\sqrt{3}-\jmath\right)\chi - \sqrt{3\pi}\left(\Omega^2+2\right)\Omega^2 - \sqrt{3\pi} \\
& +\left(\sqrt{3}+\jmath\right)\Bigg(36\sqrt[4]{\pi}\chi\left(\Omega^2-2\right) + \pi^{3/4}\left(\Omega^2+1\right)^3 \\
& +6\sqrt{6}\sqrt{-\chi\left(64\chi^2+2\sqrt{\pi}\chi\left(\Omega^4+20\Omega^2-8\right)+\pi\left(\Omega^2+1\right)^3\right)}\Bigg)^{\frac{2}{3}}\Bigg] \\
& \Bigg[36\sqrt[4]{\pi}\chi\left(\Omega^2-2\right) + \pi^{3/4}\left(\Omega^2+1\right)^3 \\
& +6\sqrt{6}\sqrt{-\chi\left(64\chi^2+2\sqrt{\pi}\chi\left(\Omega^4+20\Omega^2-8\right)+\pi\left(\Omega^2+1\right)^3\right)}\Bigg]^{-\frac{1}{3}}\Bigg\}
\end{aligned}
\tag{B.3}
$$

The solutions K are plotted in Figure B.1, where one real solutions couple emerge, together with two couples of conjugate complex solutions. As well as for the Gauss-like solutions, the only valuable curve is the real one, which equation corresponds to the inverse of the curve in equation (3.30).

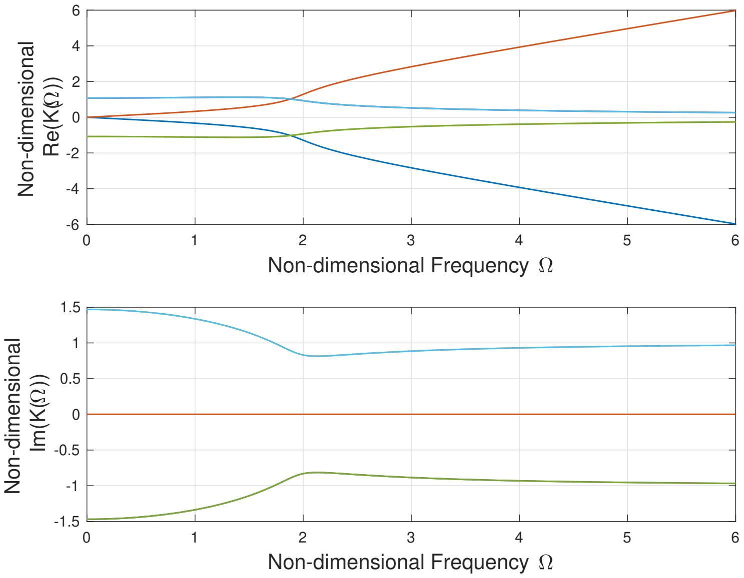

Figure B.1. Long-range Laplace-like waveguide dispersion curves (Non-dimensional frequency domain)

Appendix C

Numerical simulation Matlab basic code

The numerical simulations carried on for the Gauss-like and the Laplace-like finite rods, are based on a modal approach solved with the Galërkin[19] method. In particular, the displacement is assumed as follows:

$$w(x,t) = \sum_i \left(A_i \sin k_i x + B_i \cos k_i x\right)\left(C_i \sin \omega_i t + D_i \cos \omega_i t\right) \tag{C.1}$$

with $i \in \mathbb{N}$ is the integer index indicating the i-th mode, and $k_i = \frac{i\pi}{L}$, where the geometrical properties have been introduced in Section 3.1 and previously. The frequencies are unknown, because of the nonlocal nature of the system.
According to the boundary conditions of the system (finite rod clamped at the extrema, as in Figure 3.13), $B_i = 0$ always. The displacement is applied in the equation of motion for the generic one-dimensional long-range waveguide, equation (3.35). Writing the space contribution and the time contribution in a compact form:

$$\phi_i(x) = A_i \sin k_i x \tag{C.2a}$$

$$q_i(x) = C_i \sin \omega_i t + D_i \cos \omega_i t \tag{C.2b}$$

the equation of motion becomes:

$$-\rho \sum_i \omega_i^2 \phi_i(x) q_i(t) + E \sum_i k_i^2 \phi_i(x) q_i(t) + h(x) * \sum_i \phi_i(x) q_i(t) = 0 \tag{C.3}$$

The equation of motion can be solved minimizing the ortho-normalization error with the Galërkin method. Equation (C.3) can be split in two parts that are separately analyzed:

$$-\rho \sum_i \omega_i^2 \phi_i(x) q_i(t) + E \sum_i k_i^2 \phi_i(x) q_i(t) \tag{C.4a}$$

$$h(x) * \sum_i \phi_i(x) q_i(t) \tag{C.4b}$$

---

[19] Boris Grigoryevich Galërkin (March 4th 1871 - July 12th 1945) Soviet mathematician and engineer.

The analysis of the first part leads to the classical short-range modal rod. Introducing the diagonal matrix $\mathbf{\Lambda}$ such that $\lambda_i = \frac{i^2\pi^2}{L^2}\frac{E}{\rho}$:

$$\int_0^L \phi_j(x)\left(-\rho\sum_i \omega_i^2\phi_i(x)q_i(t) + E\sum_i k_i^2\phi_i(x)q_i(t)\right)dx = 0 \tag{C.5}$$

leads to the known relationship

$$\boldsymbol{I}\ddot{\boldsymbol{q}}(t) + \mathbf{\Lambda}\boldsymbol{q}(t) \tag{C.6}$$

with $\boldsymbol{I}$ the identity matrix and $\boldsymbol{q} = \begin{pmatrix} \vdots \\ q_j(t) \\ \vdots \end{pmatrix}$.

The solution of the second element requires more attention. It is necessary, in fact, that the convolution integral, integrated with the orthogonal mode, leads to a closed form solution. For the Gauss-like and Laplace-like models this solution exists. In general, to solve the system a $\boldsymbol{H}$ matrix is obtained as follows:

$$\boldsymbol{H} \mid [h_{ji}] = \int_0^L \phi_j(x)\int_0^L h(x-\xi)\phi_i(\xi)q_i(t)\,d\xi\,dx \tag{C.7}$$

The equation of motion becomes:

$$\boldsymbol{I}\ddot{\boldsymbol{q}}(t) + (\mathbf{\Lambda} + \boldsymbol{H})\,\boldsymbol{q}(t) = 0 \tag{C.8}$$

that corresponds to the equation of motion of a discrete modal system.

The new system is simulated according to the modal analysis technique, evaluating the eigenvalues and the eigenvectors, and letting the system evolve according to the displacement in equation C.1. Initial conditions in space are chosen for all the wavenumber spectrum.

The displacement maps depicted in Sections 3.1 and 3.2 show both time and space evolution for long-range systems. Two discrete Fourier transforms have been applied to the maps, once in space and once in time domain, obtaining the depicted dispersion surfaces. The peaks indicate a frequency-wavenumber correlation.

The time and space steps, together with the time window and the total length of the rod, have been chosen to avoid any leakage or aliasing phenomena.

Bibliography

[1] Antonio Carcaterra, A Akay, and C Bernardini. “Trapping of vibration energy into a set of resonators: Theory and application to aerospace structures”. In: *Mechanical Systems and Signal Processing* 26 (2012), pp. 1–14.

[2] Xingcun Colin Tong. “Electromagnetic Metamaterials and Metadevices”. In: *Functional Metamaterials and Metadevices*. Cham: Springer International Publishing, 2018, pp. 39–55. ISBN: 978-3-319-66044-8. URL: `https://doi.org/10.1007/978-3-319-66044-8_3`.

[3] Luke H Nicholls et al. “Ultrafast synthesis and switching of light polarization in nonlinear anisotropic metamaterials”. In: *Nature Photonics* 11.10 (2017), p. 628.

[4] Satoshi Ishii and Evgenii Narimanov. “Non-local Optical Topological Transitions and Critical States in Electromagnetic Metamaterials”. In: *Scientific Reports* 5.1 (Dec. 2015). ISSN: 2045-2322. URL: `http://dx.doi.org/10.1038/srep17824`.

[5] Yanxia Cui et al. “Plasmonic and metamaterial structures as electromagnetic absorbers”. In: *Laser & Photonics Reviews* 8.4 (June 2014), pp. 495–520. ISSN: 1863-8880. URL: `http://dx.doi.org/10.1002/lpor.201400026`.

[6] Graeme W Milton, Marc Briane, and John R Willis. “On cloaking for elasticity and physical equations with a transformation invariant form”. In: *New Journal of Physics* 8.10 (2006), p. 248.

[7] Wenshan Cai, Uday K Chettiar, Alexander V Kildishev, and Vladimir M Shalaev. “Optical cloaking with metamaterials”. In: *Nature photonics* 1.4 (2007), p. 224.

[8] Steven A Cummer, Johan Christensen, and Andrea Alù. “Controlling sound with acoustic metamaterials”. In: *Nature Reviews Materials* 1.3 (2016), p. 16001.

[9] Pai Wang et al. “Harnessing buckling to design tunable locally resonant acoustic metamaterials”. In: *Physical review letters* 113.1 (2014), p. 014301.

[10] Nicholas X Fang. “Tailoring the flow of acoustic waves by architectured metamaterials”. In: *The Journal of the Acoustical Society of America* 142.4 (2017), pp. 2683–2683.

[11] Stéphane Brûlé, EH Javelaud, Stefan Enoch, and Sébastien Guenneau. “Experiments on seismic metamaterials: molding surface waves”. In: *Physical review letters* 112.13 (2014), p. 133901.

[12] Mohamed Farhat, Sebastien Guenneau, and Stefan Enoch. "Broadband cloaking of bending waves via homogenization of multiply perforated radially symmetric and isotropic thin elastic plates". In: *Physical Review B* 85.2 (Jan. 2012). ISSN: 1550-235X. URL: `http://dx.doi.org/10.1103/PhysRevB.85.020301`.

[13] SANG-HOON KIM and MUKUNDA P. DAS. "SEISMIC WAVEGUIDE OF METAMATERIALS". In: *Modern Physics Letters B* 26.17 (July 2012), p. 1250105. ISSN: 1793-6640. URL: `http://dx.doi.org/10.1142/S0217984912501059`.

[14] Sang-Hoon Kim. "Seismic wave attenuator made of acoustic metamaterials". In: *The Journal of the Acoustical Society of America* 131.4 (Apr. 2012), pp. 3292–3292. ISSN: 0001-4966. URL: `http://dx.doi.org/10.1121/1.4708309`.

[15] Yair Zárate et al. "Elastic metamaterials for tuning circular polarization of electromagnetic waves". In: *Scientific Reports* 6.1 (June 2016). ISSN: 2045-2322. URL: `http://dx.doi.org/10.1038/srep28273`.

[16] Ilya Shadrivov. "Nonlinear effects in magneto-elastic metamaterials". In: *Antennas and Propagation (APCAP), 2015 IEEE 4th Asia-Pacific Conference on*. IEEE. 2015, pp. 401–402.

[17] Alessandro Scorrano and Antonio Carcaterra. "Semi-classical modeling of nano-mechanical transistors". In: *Mechanical Systems and Signal Processing* 39.1-2 (2013), pp. 489–514.

[18] Francesco Dell'Isola, Giulio Sciarra, and Stefano Vidoli. "Generalized Hooke's law for isotropic second gradient materials". In: *Proceedings of the Royal Society of London A: Mathematical, Physical and Engineering Sciences*. The Royal Society. 2009, rspa–2008.

[19] Ying Wu, Yun Lai, and Zhao-Qing Zhang. "Elastic metamaterials with simultaneously negative effective shear modulus and mass density". In: *Physical review letters* 107.10 (2011), p. 105506.

[20] Jayson Paulose, Bryan Gin-ge Chen, and Vincenzo Vitelli. "Topological modes bound to dislocations in mechanical metamaterials". In: *Nature Physics* 11.2 (Jan. 2015), pp. 153–156. ISSN: 1745-2481. URL: `http://dx.doi.org/10.1038/nphys3185`.

[21] Jesse L Silverberg et al. "Using origami design principles to fold reprogrammable mechanical metamaterials". In: *science* 345.6197 (2014), pp. 647–650.

[22] Sophia Sklan, Ronald Pak, and Baowen Li. "Realizable Elastic Wave Cloaking in Mechanical Metamaterials". In: *Bulletin of the American Physical Society* (2018).

[23] Christopher Sugino, Stephen Leadenham, Massimo Ruzzene, and Alper Erturk. "On the mechanism of bandgap formation in locally resonant finite elastic metamaterials". In: *Journal of Applied Physics* 120.13 (Oct. 2016), p. 134501. ISSN: 1089-7550. URL: `http://dx.doi.org/10.1063/1.4963648`.

[24] Andy Nagerl and John Watkins. *Electromagnetic Meta-Materials*. US Patent App. 14/322,453. Oct. 2014.

[25] T. Bückmann, M. Kadic, R. Schittny, and M. Wegener. "Mechanical metamaterials with anisotropic and negative effective mass-density tensor made from one constituent material". In: *physica status solidi (b)* 252.7 (Apr. 2015), pp. 1671–1674. ISSN: 0370-1972. URL: `http://dx.doi.org/10.1002/pssb.201451698`.

[26] Julia R Greer and Jiwoong Park. *Additive Manufacturing of Nano-and Microarchitected Materials.* 2018.

[27] Thomas Brunet et al. "Soft porous materials with ultra-low sound speeds in acoustic metamaterials". In: *The Journal of the Acoustical Society of America* 141.5 (2017), pp. 3811–3811.

[28] A Carcaterra, F Coppo, F Mezzani, and S Pensalfini. "Metamaterials: wave propagation control". In: *A/A* 1 (2016), p. 2.

[29] A. Carcaterra, F. Coppo, F. Mezzani, and S. Pensalfini. "Long-Range Retarded Elastic Metamaterials: Wave-Stopping, Negative, and Hypersonic or Superluminal Group Velocity". In: *Phys. Rev. Applied* 11 (1 Jan. 2019), p. 014041. URL: `https://link.aps.org/doi/10.1103/PhysRevApplied.11.014041`.

[30] Angela Madeo, Patrizio Neff, Ionel-Dumitrel Ghiba, and Giuseppe Rosi. "Reflection and transmission of elastic waves in non-local band-gap metamaterials: A comprehensive study via the relaxed micromorphic model". In: *Journal of the Mechanics and Physics of Solids* 95 (2016), pp. 441–479. ISSN: 0022-5096. URL: `http://www.sciencedirect.com/science/article/pii/S0022509616302010`.

[31] S. Hossein Mousavi, Alexander B. Khanikaev, and Zheng Wang. "Topologically protected elastic waves in phononic metamaterials". In: *Nature Communications* 6.1 (Nov. 2015). ISSN: 2041-1723. URL: `http://dx.doi.org/10.1038/ncomms9682`.

[32] Vasily E Tarasov. "Lattice with long-range interaction of power-law type for fractional non-local elasticity". In: *International Journal of Solids and Structures* 51.15 (2014), pp. 2900–2907.

[33] Vasily E Tarasov and George M Zaslavsky. "Fractional dynamics of systems with long-range interaction". In: *Communications in Nonlinear Science and Numerical Simulation* 11.8 (2006), pp. 885–898.

[34] Mario Di Paola et al. "The mechanically based non-local elasticity: an overview of main results and future challenges". In: *Phil. Trans. R. Soc. A* 371.1993 (2013), p. 20120433.

[35] Mario Di Paola and Massimiliano Zingales. "Long-range cohesive interactions of non-local continuum faced by fractional calculus". In: *International Journal of Solids and Structures* 45.21 (2008), pp. 5642–5659. ISSN: 0020-7683. URL: `http://www.sciencedirect.com/science/article/pii/S0020768308002461`.

[36] Antonio Carcaterra, Nicola Roveri, and Adnan Akay. "Connectivity in waves and vibrations: one-to-six, one-to-all, all-to-all and random connections". In: *Proceedings of ISMA2018 International Conference on Noise and Vibration Engineering USD2016 International Conference on Uncertainty in Structural Dynamics.* 2018.

[37] A. Carcaterra and A. Sestieri. “ENERGY DENSITY EQUATIONS AND POWER FLOW IN STRUCTURES”. In: *Journal of Sound and Vibration* 188.2 (1995), pp. 269–282. ISSN: 0022-460X. URL: `http://www.sciencedirect.com/science/article/pii/S0022460X85705913`.

[38] Antonio Carcaterra and A Akay. “Dissipation in a finite-size bath”. In: *Physical Review E* 84.1 (2011), p. 011121.

[39] Antonio Carcaterra, F Dell’Isola, R Esposito, and M Pulvirenti. “Macroscopic description of microscopically strongly inhomogenous systems: A mathematical basis for the synthesis of higher gradients metamaterials”. In: *Archive for Rational Mechanics and Analysis* 218.3 (2015), pp. 1239–1262.

[40] Antonio Carcaterra and A Akay. “Fluctuation-dissipation and energy properties of a finite bath”. In: *Physical Review E* 93.3 (2016), p. 032142.

[41] A Carcaterra, G Pepe, and N Roveri. “Energy exchange between nonlinear oscillators: an entropy foundation”. In: *analysis* 19 (2016), p. 23.

[42] Antonio Carcaterra and Adnan Akay. “Pseudo-damping in undamped plates and shells”. In: *The Journal of the Acoustical Society of America* 120.5 (2006), pp. 3132–3132.

[43] Adnan Akay, Zhaoshun Xu, Antonio Carcaterra, and I Murat Koç. “Experiments on vibration absorption using energy sinks”. In: *The Journal of the Acoustical Society of America* 118.5 (2005), pp. 3043–3049.

[44] Adnan Akay and Antonio Carcaterra. “Theory and application of pseudo-damping in structures”. In: *The Journal of the Acoustical Society of America* 123.5 (2008), pp. 3058–3058.

[45] F. Coppo, A. S. Rezaei, and A. Mezzani F. Pensalfini S. Carcaterra. “Waves path in an elastic membrane with selective nonlocality”. In: *Proceedings of ISMA2018 International Conference on Noise and Vibration Engineering USD2016 International Conference on Uncertainty in Structural Dynamics*. 2018.

[46] S. Pensalfini et al. “Optimal control theory based design of elasto-magnetic metamaterial”. In: *Procedia Engineering* 199.Supplement C (2017). X International Conference on Structural Dynamics, EURODYN 2017, pp. 1761–1766. ISSN: 1877-7058. URL: `http://www.sciencedirect.com/science/article/pii/S1877705817339371`.

[47] Nicola Roveri, Sara Pensalfini, and Antonio Carcaterra. “Small-world based interactions in mechanical systems”. In: *Proceedings of ISMA2018 International Conference on Noise and Vibration Engineering USD2016 International Conference on Uncertainty in Structural Dynamics*. 2018.

[48] F Mezzani et al. “Twin-waves propagation phenomena in magnetically-coupled structures”. In: *Procedia Engineering* 199 (2017), pp. 711–716.

[49] F. Mezzani, F. Coppo, and A. Carcaterra. “Long-range coupling of waveguides”. In: *Proceedings of ISMA2018 International Conference on Noise and Vibration Engineering USD2016 International Conference on Uncertainty in Structural Dynamics*. 2018.

[50] Vincent Laude and Maria E Korotyaeva. “Stochastic band structure for waves propagating in periodic media or along waveguides”. In: *arXiv preprint arXiv:1801.09914* (2018).

[51] Andres D Neira, Gregory A Wurtz, and Anatoly V Zayats. “Superluminal and stopped light due to mode coupling in confined hyperbolic metamaterial waveguides”. In: *Scientific reports* 5 (2015), p. 17678.

[52] DE Chang, Amir H Safavi-Naeini, Mohammad Hafezi, and Oskar Painter. “Slowing and stopping light using an optomechanical crystal array”. In: *New Journal of Physics* 13.2 (2011), p. 023003.

[53] Mehmet Fatih Yanik and Shanhui Fan. “Stopping light all optically”. In: *Physical review letters* 92.8 (2004), p. 083901.

[54] Kosmas L Tsakmakidis et al. “Completely stopped and dispersionless light in plasmonic waveguides”. In: *Physical review letters* 112.16 (2014), p. 167401.

[55] WM Robertson et al. “Sound beyond the speed of light: Measurement of negative group velocity in an acoustic loop filter”. In: *Applied physics letters* 90.1 (2007), p. 014102.

[56] Dexin Ye et al. “Observation of wave packet distortion during a negative-group-velocity transmission”. In: *Scientific reports* 5 (2015), p. 8100.

[57] David Maximilian Storch, Mauritz Van den Worm, and Michael Kastner. “Interplay of soundcone and supersonic propagation in lattice models with power law interactions”. In: *New Journal of Physics* 17.6 (2015), p. 063021.

[58] Jingyuan Qu et al. “Experiments on Metamaterials with Negative Effective Static Compressibility”. In: *Physical Review X* 7.4 (2017), p. 041060.

[59] Nicolas Brunner et al. “Direct measurement of superluminal group velocity and signal velocity in an optical fiber”. In: *Physical review letters* 93.20 (2004), p. 203902.

[60] Kirk T McDonald. “Negative group velocity”. In: *American Journal of Physics* 69.5 (2001), pp. 607–614.

[61] OE Martinez, JP Gordon, and RL Fork. “Negative group-velocity dispersion using refraction”. In: *JOSA A* 1.10 (1984), pp. 1003–1006.

[62] George M Gehring et al. “Observation of backward pulse propagation through a medium with a negative group velocity”. In: *Science* 312.5775 (2006), pp. 895–897.

[63] A Dogariu, A Kuzmich, and LJ Wang. “Transparent anomalous dispersion and superluminal light-pulse propagation at a negative group velocity”. In: *Physical Review A* 63.5 (2001), p. 053806.

[64] W.S. Slaughter. *The Linearized Theory of Elasticity.* Birkhäuser Boston, 2002. ISBN: 9780817641177.

[65] Jean le Rond d’Alembert. “Recherches sur la courbe que forme une corde tendue mise en vibration”. In: (1747).

[66] Antonio Carcaterra, A Akay, and IM Koc. “Near-irreversibility in a conservative linear structure with singularity points in its modal density”. In: *The Journal of the Acoustical Society of America* 119.4 (2006), pp. 2141–2149.

[67] Leon Brillouin. *Wave propagation in periodic structures: electric filters and crystal lattices.* Courier Corporation, 2003.

[68] Erasmo Recami. “Superluminal waves and objects: An overview of the relevant experiments”. In: *Journal of Physics: Conference Series* 196 (Nov. 2009), p. 012020. ISSN: 1742-6596. URL: `http://dx.doi.org/10.1088/1742-6596/196/1/012020`.

[69] D Alleyne and Peter Cawley. “A two-dimensional Fourier transform method for the measurement of propagating multimode signals”. In: *The Journal of the Acoustical Society of America* 89.3 (1991), pp. 1159–1168.

[70] Léon Brillouin. *Wave propagation and group velocity.* Vol. 8. Academic Press, 2013.

[71] Nico M Temme. *Special functions: An introduction to the classical functions of mathematical physics.* John Wiley & Sons, 2011.

[72] I Bucher and DJ Ewins. “Modal analysis and testing of rotating structures”. In: *Philosophical Transactions of the Royal Society of London A: Mathematical, Physical and Engineering Sciences* 359.1778 (2001), pp. 61–96.

[73] Solomon Davis and Izhak Bucher. “Automatic vibration mode selection and excitation; combining modal filtering with autoresonance”. In: *Mechanical Systems and Signal Processing* 101 (2018), pp. 140–155.

[74] Izhak Bucher and Amit DOLEV. *Method and system for parametric amplification.* US Patent App. 10/061,181. Aug. 2018.

[75] Ran Gabai et al. “A rotational traveling wave based levitation device–Modelling, design, and control”. In: *Sensors and Actuators A: Physical* 255 (2017), pp. 34–45.

[76] E.P. Furlani and Engineering Information Inc. *Permanent Magnet and Electromechanical Devices: Materials, Analysis, and Applications.* Academic Press series in electromagnetism. Elsevier Science, 2001. ISBN: 9780122699511. URL: `https://books.google.it/books?id=irsdLnC5SrsC`.

[77] Dirk Helbing, Ansgar Hennecke, Vladimir Shvetsov, and Martin Treiber. “Micro-and macro-simulation of freeway traffic”. In: *Mathematical and computer modelling* 35.5-6 (2002), pp. 517–547.

[78] H Gayathri, PM Aparna, and Ashish Verma. “A review of studies on understanding crowd dynamics in the context of crowd safety in mass religious gatherings”. In: *International Journal of Disaster Risk Reduction* (2017).

[79] Dirk Helbing and Peter Molnar. “Social force model for pedestrian dynamics”. In: *Physical review E* 51.5 (1995), p. 4282.